

**THE UNIVERSITY *of* LIVERPOOL**

**Advanced Modelling and Feature Extraction for Fault Diagnosis  
of Power Apparatus**

Thesis submitted in accordance with the  
requirements of the University of Liverpool  
for the degree of Doctor of Philosophy

in

Electrical Engineering and Electronics

by

Chenghao Wei, M.Sc.(Eng.)

June 2015

**Advanced Modelling and Feature Extraction for Fault Diagnosis of Power  
Apparatus**

by  
Chenghao Wei

Copyright 2015

## **Acknowledgements**

First and foremost, I would like to give my heartfelt thanks to my supervisors, Dr. T. T. Mu and Prof. W. H. Tang, not only for their invaluable support, stimulating discussions and intellectual guidance, but also for providing such a great opportunity to enhance my capability both on an academic and personal level. They have made a great number of contributions to this research, for which i am truly appreciative.

I am deeply grateful to Prof. Q. H. Wu, for his kind guidance with his knowledge of power systems. The research skill, writing skill and presenting skill he taught me will benefit me throughout my life, as well as his inspiring insight into life philosophy and poetry.

I also want to offer my regards to all the members of the Intelligence Engineering and Automation Group for our valuable discussions, especially to Mr. L. Yan. Special thanks also goes to my friends, Miss J. Zhu and Dr Z. K. Zhang, for their great support and friendship. I am indebted to the University of Liverpool for the studentship. My thanks are offered to the Department of Electrical Engineering and Electronics at the University of Liverpool, for providing the research facilities that made it possible for me to carry out this research.

Finally, my thanks goes to my beloved wife for her loving considerations and great confidence in me through these hard years.

# Abstract

This thesis presents novel methods for advanced modeling and fault diagnosis of power apparatuses, which mainly contain power transformers and induction motors. These two popular applied power apparatuses are inherently reliable. But, they may deteriorate and fail without effective preventive maintenance. This gives rise to the need of research work for condition monitoring and assessment.

For the condition monitoring and assessment of a power transformer, dissolved gas analysis (DGA) has been applied to determine the condition of a power transformer during the past decades. A core problem needs to be considered is the classification of nonlinear DGA gas data. As a well-approved technique to diagnose incipient faults, all the applied fault interpretation methods are based on the DGA data of laboratory simulation and industrial faulty inspection. These inspection data are usually obtained by periodically sampling liquids from power transformers and analysing the dissolved gases in laboratories. Threshold values of DGA interpretation methods are obtained by using the DGA gas records of laboratory simulation and industrial faulty inspection. But, it is not always possible to conduct precise measurements of gas records, the measurement errors sometimes too big to obtain correct DGA results. Hence, threshold values and error redundancy of current DGA methods need to be re-examined using DGA gas records within a reasonable error range. In the study, in order to test the reliability of DGA methods, the  $\pm 5\%$  variation is applied to faulty gas value of laboratory simulated case and the  $\pm 10\%$  variation is used to those fault cases identified by inspection of the equipment. Based on the analysis of results, three zones of Duval triangle, which represent highly possible misclassification faults of discharge, overheating and partial discharge, are concluded for improving its reliability.

Conventional DGA ratio methods are not unbiased and sometimes provide different judgements. In order to establish a reliable, intelligent fault classification method, three main aspects, including DGA data pre-processing, effective gas feature extraction, and optimised computational classifiers have been considered for the classification of non-linear DGA data. To cope with the highly versatile or noise-corrupted DGA data, two methods, bootstrap and logarithm transformation under two base and ten base conditions, are employed as data pre-processing tools. For gas feature extraction, unified and non-unity new features are first obtained based on in-depth analysis of current DGA standards. Meanwhile, the statistical characteristics of the selected gas features are used for prioritisation.

A ten based logarithmic transformation is first applied to three select ratios of combustible gases against the total gas volume and the total gas volume itself. The bootstrap method is used to overcome the shortage of class samples. Nine features, including five features of conventional ratios, are used as input vectors to SVM, LS-SVM and SVDD, whose tuning parameters are optimised by PSO. Comparisons of classification results between conventional gas ratios and the proposed nine feature ratios are illustrated finally. It shows that PSO-LSSVM has the highest classification accuracy using nine feature ratios.

These unified features of different classifications might cause redundant information that leads to a low overall accuracy. Therefore, attempts have been made to achieve feature extraction for different classification condition by the analysis of Duval triangle, IEC standards and feature prioritisation. A two based logarithmic transformation is applied as data preprocessing. Prioritization orders of all gas features are obtained for different classification levels by using the Kolmogorov-Smirnov (K-S) test. The first three highly ranked features are selected as input vectors for a multi-layer PSO-SVM classifier. For comparison, a three layer multilayer perception (MLP) neural networks, PSO-SVM and KNN are applied with different number of genetic programming (GP) features. Among all classification accuracies, the PSO-SVM with the proposed features can gain the highest accuracy.

In the appendix part, the detection of broken bars of an induction machine based on multiple coupled circuit model is proposed. The optimised motor parameters

are achieved by minimising the gap between experimental results and simulation model responses using GA. Based on the optimised model, faults of one broken bar and two broken bars conditions are detected by extracting the harmonic components appearing at the right and left sides of the fundamental frequency.

# **Declaration**

The author hereby declares that this thesis is a record of work carried out in the Department of Electrical Engineering and Electronics at the University of Liverpool during the period from January 2011 to June 2014. The thesis is original in content except where otherwise indicated.

# Contents

<b>List of Figures</b>	<b>xi</b>
<b>List of Tables</b>	<b>xiii</b>
<b>List of Abbreviations and Symbols</b>	<b>xv</b>
<b>1 Introduction</b>	<b>1</b>
1.1 Condition Monitoring of Power Transformers . . . . .	1
1.2 Motivation and Objectives . . . . .	2
1.2.1 Uncertainty in Dissolved Gas Analysis . . . . .	2
1.2.2 Objectives . . . . .	3
1.3 Contribution of work . . . . .	4
1.4 Thesis Outline . . . . .	5
<b>2 Transformer Condition Assessment Based on Dissolved Gas Analysis</b>	<b>7</b>
2.1 Introduction . . . . .	7
2.2 Operating Procedures of DGA . . . . .	9
2.2.1 Evolution of Gas . . . . .	11
2.2.2 Determination of Combustible Gassing Rate . . . . .	14
2.2.3 Computation of Gas Space and Dissolved Gas-in-Oil Equiv- alents . . . . .	16
2.2.4 General Operation Procedure using Dissolved Gas Concen- tration . . . . .	18
2.3 Gas Interpretation Methods . . . . .	19
2.3.1 Key Gas Method . . . . .	19
2.3.2 Gas Ratio Methods . . . . .	21
2.3.3 Duval Triangle Methods . . . . .	25
2.3.4 Further Issues on Dissolved Gas Analysis . . . . .	33
2.4 Summary . . . . .	35
<b>3 Study and Analysis of DGA with Sampling Errors</b>	<b>37</b>
3.1 Introduction . . . . .	37
3.2 DGA Measurement Methods . . . . .	39



3.3	Gas Variation . . . . .	40
3.4	Duval Triangle Test . . . . .	41
3.5	IEC Ratio Test . . . . .	64
3.6	Summary . . . . .	67
<b>4</b>	<b>Approaches to Incipient Fault Detection for Oil-Immersed Power Transformer using Support Vector Classifiers</b>	<b>69</b>
4.1	Introduction . . . . .	70
4.2	Pre-process DGA Data . . . . .	71
4.2.1	Logarithmic Transform of DGA Concentrations . . . . .	71
4.2.2	Basic Theory of Bootstrap . . . . .	72
4.3	Support Vector Based Classification Methods . . . . .	73
4.3.1	Support Vector Machine . . . . .	73
4.3.2	Least-Square Support Vector Machine . . . . .	75
4.3.3	Support Vector Domain Description . . . . .	76
4.4	Particle Swarm Optimisation . . . . .	77
4.5	Results and Discussion . . . . .	80
4.5.1	Sample Number Equalisation for Different Fault Classes Using Bootstrap . . . . .	81
4.5.2	Classification Results . . . . .	83
4.5.3	Classification Decision Boundary . . . . .	85
4.6	Conclusions . . . . .	90
<b>5</b>	<b>A Dissolved Gas Analysis Method Based on New Feature Prioritisation and Different Classifiers</b>	<b>91</b>
5.1	Introduction . . . . .	92
5.2	New Feature Extraction and Data Preprocessing . . . . .	93
5.2.1	New Features Between Normal and Fault Cases . . . . .	94
5.2.2	New Features Between Thermal and Discharge Cases . . . . .	95
5.2.3	New Feature Between Low and High Energy Discharge Cases . . . . .	96
5.2.4	DGA Data Preprocessing . . . . .	96
5.3	Computational method for feature selection . . . . .	98
5.3.1	Kolmogorov-Smirnov Test . . . . .	98
5.3.2	<i>K</i> -Nearest Neighbors Algorithm . . . . .	99
5.4	Experimental Results . . . . .	101
5.4.1	Feature Prioritisation using K-S Test . . . . .	102
5.4.2	Configuration of Intelligent classifiers . . . . .	104
5.4.3	Classification Results using the K-S Features . . . . .	106
5.4.4	Classification Results using GP Features . . . . .	107
5.5	Conclusion . . . . .	110
<b>6</b>	<b>Conclusion and Future work</b>	<b>111</b>

<b>References</b>	<b>114</b>
<b>Appendix A</b>	<b>123</b>
A.1 Multiple Coupled Circuit Modeling . . . . .	125
A.2 Winding Function Method . . . . .	128
A.3 Genetic Algorithms . . . . .	131
A.4 Simulation Results . . . . .	132
A.5 Summary . . . . .	138
References . . . . .	140

# List of Figures

2.1	Operating procedures of DGA [1] . . . . .	10
2.2	Free radicals due to heating of mineral oil [1] . . . . .	11
2.3	Experimental bond entropies for several important radial [2] . . . . .	12
2.4	Oil decomposition temperature over 150 °C [3] . . . . .	13
2.5	Duval triangle 1 [4] . . . . .	27
2.6	Duval triangle 2 [5] . . . . .	28
2.7	Duval triangle 3 of silicone oil [5] . . . . .	31
2.8	Duval triangle 3 of synthetic ester [5] . . . . .	31
2.9	Duval triangle 3 of natural esters [5] . . . . .	32
2.10	Duval triangle 3 of vegetable oils [5] . . . . .	33
3.1	Laboratory DGA data in Duval triangle . . . . .	43
3.2	Laboratory simulated faults in paper with %5 variation . . . . .	44
3.3	Simulated paper in oil fault with 5% variation . . . . .	45
3.4	Simulated oil fault with 5% variation . . . . .	46
3.5	Inspected fault cases below 700 degree with 10% variation . . . . .	46
3.6	Inspected fault cases below 700 degree with threshold variation . . . . .	48
3.7	Inspected fault cases above 700 degree with variation of 10 percent . . . . .	50
3.8	Inspected fault cases above 700 degree with threshold variation . . . . .	51
3.9	Thermal fault with threshold variation . . . . .	51
3.10	Electrical low energy discharge simulated in the laboratory with 5 percent variation . . . . .	52
3.11	Fault identified as discharges of low energy by inspection of the equipment with 10 percent variation . . . . .	55
3.12	Fault identified as discharges of low energy by inspection of the equipment with threshold variation . . . . .	57
3.13	Fault identified as discharges of high energy by inspection of the equipment with 10 percent variation . . . . .	60
3.14	Fault identified as discharges of high energy by inspection of the equipment with threshold variation . . . . .	61
3.15	Discharges of energy equipment with threshold variation . . . . .	61
3.16	Partial discharge simulated in the laboratory with 5 percent variation . . . . .	62

3.17	Partial discharge fault by inspection of the equipment with 10 percent variation . . . . .	62
3.18	Duval triangle with variation threshold . . . . .	63
4.1	Maximum-margin hyperplane for an SVM with samples from two classes . . . . .	74
4.2	Classification result using Duval triangle . . . . .	81
4.3	SVM classification using conventional features . . . . .	86
4.4	SVM classification using additional features . . . . .	87
4.5	SVM classification using additional features . . . . .	87
4.6	LS-SVM classification using additional features . . . . .	88
4.7	LS-SVM classification using additional features . . . . .	88
4.8	SVDD classification using additional features . . . . .	89
4.9	SVDD classification using additional features . . . . .	89
5.1	Triangle graphical form . . . . .	96
5.2	(a) Ratio values by using logarithm transformation. (b) Ratio values before logarithm transformation . . . . .	97
5.3	(a) CDF of %C <sub>2</sub> H <sub>2</sub> in the normal case. (b) The K-S test of %C <sub>2</sub> H <sub>2</sub> between normal and overheating. . . . .	99
5.4	Diagnostic model using multi-layer SVM classifier . . . . .	105
A.1	Multiple coupled circuit rotor model . . . . .	126
A.2	Winding distribution of a rotor loop . . . . .	130
A.3	GA flow chart . . . . .	134
A.4	Comparison of measured current [3], simulation current using original parameters and simulation current using GA parameters . . . . .	136
A.5	Comparison of measured speed [3], simulation speed using original parameters and simulation speed using GA parameters . . . . .	137
A.6	Comparison of health power spectrum, one broken bar power spectrum and two broken bars power spectrum . . . . .	137

# List of Tables

2.1	Bond dissociation energy [2] . . . . .	12
2.2	Actions based on TCG gas rate [1] . . . . .	15
2.3	Actions based on TDCG gas rate [1] . . . . .	16
2.4	Ostwald coefficient of each gas [1] . . . . .	17
2.5	Dissolved gas concentration limits( $\mu l/L$ ) [1] . . . . .	18
2.6	Typical values of key gases [1] . . . . .	19
2.7	IEC ratio methods [6] . . . . .	23
2.8	Concentration limits of Doernenburg ratio method [1] . . . . .	24
2.9	Fault diagnosis concentration limits of Doernenburg ratio method [1]	25
2.10	Concentration limits of Duval ratio method [7] . . . . .	26
2.11	Identification of fault zones in Duval Triangle 2 [5] . . . . .	29
2.12	Numerical zone boundaries of Figure 2.6 [5] . . . . .	29
2.13	Zone boundaries (in $C_2H_4\%$ ) specific for non-mineral oils in the Duval Triangle 3 for non-mineral oils [5] . . . . .	32
3.1	Repeatability of IEC/CIGRE laboratories surveys [8] . . . . .	40
3.2	Accuracy of IEC/CIGRE laboratories [8] . . . . .	40
3.3	DGA data cases under 5% variation . . . . .	41
3.4	Simulated results of overheating faults [9] . . . . .	42
3.5	Hot spots in oil simulated in the laboratory [9] . . . . .	45
3.6	Fault identified as thermal faults < 700 (T1 and T2) by inspection of the equipment [9] . . . . .	47
3.7	Fault identified as thermal faults > 700 (T3) by inspection of the equipment [9] . . . . .	49
3.8	Electrical low energy discharge simulated in the laboratory [9] . . .	52
3.9	Fault identified as discharges of low energy ( D1 ) by inspection of the equipment [9] . . . . .	54
3.10	Fault identified as discharges of high energy ( D2 ) by inspection of the equipment [9] . . . . .	58
3.11	Fault identified as discharges of high energy ( D2 ) by inspection of the equipment [9] . . . . .	59
3.12	Classification result of each fault . . . . .	64
3.13	Classification result of each type of fault . . . . .	65

4.1	90% Typical normal values (ppm) for power transformers without a communicating OLTC [9] . . . . .	78
4.2	90% Typical normal values (ppm) for power transformers with a communicating OLTC [9] . . . . .	79
4.3	Influence of various parameters on 90% typical (normal) values in power transformers [9] . . . . .	79
4.4	Length of 95% confidence intervals of gas ratio data . . . . .	82
4.5	PSO-SVM without additional features $\xi = 0.5171$ and $C = 13.5626$	83
4.6	PSO-LSSVM without additional feature $\xi = 2.5728$ and $C = 4.2486$	83
4.7	PSO-SVDD without additional feature $\xi = 0.6139$ and $C = 0.2839$	83
4.8	PSO-SVM with additional features $\xi = 0.0452$ and $C = 71.7022$ .	84
4.9	PSO-LSSVM with additional features $\xi = 2.3820$ and $C = 7.7891$	84
4.10	PSO-SVDD with additional features $\xi = 0.4562$ and $C = 0.1918$ .	85
5.1	Rogers ratio for key gases . . . . .	94
5.2	Maximum D values for features without bootstrapping . . . . .	102
5.3	Feature ranking using K-S test results without bootstrapping . . . . .	103
5.4	Maximum D values for features with bootstrapping . . . . .	103
5.5	Features ranking using K-S test results with bootstrapping . . . . .	104
5.6	Classification accuracy (%) using multi-layer PSO-SVM with different features . . . . .	107
5.7	Test classification accuracy(%) of GP-ANN with different neuron numbers . . . . .	107
5.8	Test classification accuracy (%) of PSO-SVM using GP features . .	108
5.9	Test classification accuracy (%) of GP-KNN with different neighbor number . . . . .	108
5.10	Best test classification accuracy(%) of different classifiers . . . . .	109
A.1	Induction motor parameters [3] . . . . .	133
A.2	Parameter results using GA . . . . .	135
A.3	Frequency Points . . . . .	136
A.4	Speed and Torque . . . . .	138

# List of Abbreviations and Notations

## Abbreviations

<b>DGA</b>	Dissolved Gas Analysis
<b>TCG</b>	Total Combustible Gas
<b>TDCG</b>	Total Dissolved Combustible Gas
<b>SVM</b>	Support Vector Machine
<b>LSSVM</b>	Least Square Support Vector Machine
<b>PSO</b>	Particle Swarm Optimization
<b>SVDD</b>	Support Vector Data Description
<b>GA</b>	Genetic Algorithm
<b>PDA</b>	Partial Discharge Analysis
<b>OLTCs</b>	On-line Load Tap Changers
<b>ECT</b>	Electrostatic Charging Tendency
<b>BDV</b>	Break Down Voltage
<b>TCD</b>	Thermal Conductivity Detector
<b>FID</b>	Flame Ionization Detector
<b>ECDF</b>	Empirical Cumulative Distribution Function
<b>CDF</b>	Cumulative Distribution Function
<b>VFD</b>	Variable Frequency Drive
<b>EP</b>	Evolutionary Programming
<b>RWS</b>	Roulette Wheel Selection
<b>MCSA</b>	Motor Current Signature Analysis

# **Chapter 1**

## **Introduction**

This chapter concentrates on a clear introduction for this thesis. A brief review of condition monitoring for power transformer is presented at first. The motivation and objectives are then introduced, followed by main contributions, and a specific view of the thesis contents.

### **1.1 Condition Monitoring of Power Transformers**

Power transformer is an important apparatuses in current power industry. Power transformers, on-line load tap changers (OLTCs) and other switchgears are the main elements of transmission and distribution infrastructure. They can move power from generating utility to industrial consumers or residential consumers. If these critical assets were to fail, power outages, personal and environmental hazards may be caused. In order to ensure maximum uptime, critical assets should be closely and continuously monitored especially power transformers, which are the most expensive assets in the power transmission and distribution networks. They can enable us to transmit electrical energy over a great distance and distribute it safely to customers. In result, failures of the power transformers are sometimes catastrophic and always along with irreversible internal damage. Its healthy functioning is vital to whole systems of operations. Therefore, it is very necessary to monitor the behavior of a power transformer. Conditional monitoring explores the possibilities



of acquiring maximum operating time and optimum life of a power transformer, reducing the risk of failures and providing the reasonable maintenance strategy [10] [11]. Typical transformer maintenance programs include condition and assessment testing, dissolved gas analysis and oil quality testing. On-line and off-line detectors are being developed to monitor the transformers [12]. Three main aspects of transformer condition monitoring are thermal modelling, partial discharge analysis (PDA) and dissolved gas analysis (DGA). Thermal aging of transformer is mainly determined by its daily cyclic loadings. Many loading guides provide the suggestion for choosing the correct transformer ratings under a given loading condition. Several publications are applied for this aim, international electrotechnical commission (IEC) 60354 standard [13] can be applied to oil immersed transformers, while IEC 60905 standard considers dry type transformers [14]. Actually, major power transformer is filled with a fluid for several purposes, acting as dielectric media, ensuring insulation condition and transferring heat during operation. Normally, a slow degradation of the mineral oil always exists during normal daily operation. It will be enhanced due to the energy of faults. Partial discharge (PD) is a typical reason. PD occurs when the local electric field exceeds the threshold value, resulting in a partial breakdown of the surrounding medium [15].

## **1.2 Motivation and Objectives**

### **1.2.1 Uncertainty in Dissolved Gas Analysis**

Dissolved gas analysis (DGA) [1] [4] [9], which evaluates operation condition of a transformer using gas concentrations of the insulation oil periodically, is one of the most important methods for the fault detection. The core of DGA is interpretation method of the fault gas. The Doernenburg ratio method uses four gas ratios while the Roger ratio method employs three combustible gas ratios [1]. The Triangle graphical method [9] was proposed for fault classification using three combustible gas percentages. As known, not all the combinations of gas ratios presented in a fault can be mapped to a fault type as described in a diagnostic criterion. Different transformer diagnostic techniques may give varied analysis results, and it is difficult

for engineers to make a final decision when facing with so much diverse information. Furthermore, the use of gas ratio should be applied according to the fault type. Each well-known method has some drawbacks during industrial applications, e.g. “lack code”, rigorous borderline and hidden relationships. As a well-approved technique to diagnose incipient faults, all the mentioned fault interpretation methods are based on the DGA data of laboratory simulation and industrial faulty inspection. But, these inspection data are usually obtained by periodically sampling liquids from power transformers and analysing the dissolved gases in laboratories. Sampling errors always existed by using any DGA monitoring instruments. For the laboratory DGA results, many factors can affect the final detection of gas values, such as poor conditions of oil sample transportation and oil sample storage. Vital research works have been done in the university of Manchester, where researchers compared the laboratory DGA results and online monitor DGA results [16], and their results indicated that deviations between their results are generally within 30%. It is actually large enough to affect the final DGA detection results. Therefore, it is worth to re-examine current standardised methods by using DGA data with a reasonable error range.

There is no universally accepted DGA interpretation scheme due to the heuristic nature of such methods. Recently, the uncertainty of these methods can be mitigated by using fuzzy logic set [17]. In addition, a systematic stochastic petri net based methodology was applied for fault detection of power transformer and its corresponding repair method [18]. Support vector based classifiers, such as support vector machine and least-square support machine, have been applied to gas ratio forecasting [19] and classification [20]. A combined artificial neural network (ANN) and expert system tool is developed for transformer fault diagnosis using dissolved gas analysis [21]. New artificial intelligence technique can be applied to preprocess the data and improve the overall classification accuracy.

### 1.2.2 Objectives

The objectives of this research are oil-immersed power transformers and squirrel-cage induction rotors. For the oil-immersed power transformers, DGA

datasets will be extracted from the available historical records, which are collected from DGA data of laboratory simulation and industrial faulty inspection. Current standardised methods are re-examined by using these datasets with resealable errors range. Novel data preprocessing techniques will be applied to obtain new gas feature and equalise the numbers of each dataset. Artificial intelligence algorithms are used to improve the classification accuracy by effectively handling the non-linear DGA data.

A detailed model of a squirrel cage induction motor is established with careful consideration of current of each rotor slot. The optimisation of the model is achieved by applying GA algorithms and broken rotor bar fault is detected by using this optimised model. Finally, the negative effects on the induction motor is fully discussed under the broken bar situation.

### 1.3 Contribution of work

List of the publication during this research:

Conference publications:

T. Y. Ji, W. H. Tang, **C. H. Wei** and Q. H. Wu, “Frequency Response Analysis of Transformer Winding Deformation Based on Multiconductor Transmission Line Model”, 4th UHVnet Colloquium, Jan. 18-19, 2011, Winchester, UK.

**C.H. Wei**, L. Yan, W.H. Tang and Q.H. Wu, “Detection of Broken Bars in Induction Motor Based on Multiple Coupled Circuit Model with Optimized Parameters”, The 5th IEEE PES Asia-Pacific Power and Energy Engineering Conference, Dec. 8-11, 2013, HK.

L. Yan, **C.H. Wei**, W.H. Tang and Q.H. Wu, “Development of a novel asset management system for power transformers based on ontology”, The 5th IEEE PES Asia-Pacific Power and Energy Engineering Conference, Dec. 8-11, 2013, HK.

Journal publications:

**C. H. Wei**, W. H. Tang and Q. H. Wu, “A Hybrid Least-square Support Vector Machine Approach to Incipient Fault Detection for Oil-immersed Power Transformers”, *Electric Power Components and Systems*, vol. 42, no. 5, pp. 453-

463, 2014.

C. H. Wei, W. H. Tang and Q. H. Wu, "A Dissolved Gas Analysis Method Based on Novel Feature Prioritisation and Support Vector Machine", IET Electric Power Applications, vol. 8, no. 8, pp. 320-328, 2014.

## 1.4 Thesis Outline

The works of this thesis contain two parts, where the main topic is intelligent transformer fault detection using dissolved gas analysis (DGA). The other topic is about the detection of broken bars in induction motor based on multiple coupled circuit model with optimized parameters by using genetic algorithm (GA). This thesis is structured as follows:

**Chapter 2 :** This chapter is concentrated on conventional DGA techniques as well as their latest developments. Important international standards of DGA have been reviewed in details. All the international DGA fault interpretation methods, which are based on the DGA data of laboratory simulation and industrial fault inspection, are discussed carefully.

**Chapter 3 :** The chapter is focused on re-examination of current standardised methods. Error range values are selected based on a detailed discussion of the measurement accuracies of CIGRE Laboratories. Current standardised methods are re-examined by using DGA data with a reasonable 5%-10% error range. Error redundancy of Duval triangle and IEC ratio method is discussed, and some specific zones of Duval Triangle are highlighted for extra cautious during its industrial application.

**Chapter 4 :** This chapter is mainly focused on dealing with the nonlinear DGA data using the support vector classifiers. Two methods are applied for DGA data preprocessing. The resample tool bootstrap is used for overcoming the shortage of faulty data numbers. The logarithmic transformation of DGA concentrations rescales the gas ratio to generate additional features. Particle swarm optimisation is applied to search the optimised combination of preset

parameters of classifiers within a short convergence time. The chapter is published as a paper in a journal of electric power components and systems.

**Chapter 5 :** Although new features are proposed in the preceding chapter, some of them may be redundant. This chapter mainly concentrates on feature extraction and preprocessing. Firstly, novel gas features are manually selected based on in-depth analysis of well-known DGA international standards. Combined with conventional gas features, prioritisation of all features is obtained by using the K-S test. The features in the first three rankings are applied as input vectors for PSO. The results are obtained from other artificial intelligence classifiers with data of genetic programming are provided for comparisons.

**Chapter 6 :** This chapter concludes the thesis by giving a summary of the results of each chapter. Suggestions for possible future work are also listed at the end.

**Appendix :** This part proposed a method for the detection of broken bars of an induction machine based on multiple coupled circuit model. The optimised motor parameters are achieved by minimising the gap between experimental results and simulation model responses using GA. Based on the optimised model, faults of one broken bar and two broken bars conditions are detected by extracting the harmonic components of stator current.

## **Chapter 2**

# **Transformer Condition Assessment Based on Dissolved Gas Analysis**

This chapter concentrates on literatures of transformer condition assessment with respect to dissolved gas analysis and its latest development. A brief introduction to current DGA standards is given. Complicated chemical processes of the evolution of gas are discussed under the conditions of high temperatures and discharge. Bond dissociation energies of different gas molecules are also explored for an in-depth understanding of gas evolution. Determination of the operating procedure using total combustible gas (TCG) and total dissolved combustible gas (TDCG) are presented. The core parts of DGA, which are various gas interpretation methods, such as Duval triangle methods [4] [9], Key gas method [1], IEC ratio method [6], Rogers ratio [1] [22], and Dornenburg ratio method [1] [23], are discussed in detail. Finally, main advantages and obstacles of DGA methods are summarised.

### **2.1 Introduction**

The dissolved gas analysis (DGA) has been widely utilised to detect incipient faults in oil-filled power transformers [1] [9] [22] [23]. Traditional condition assessment of transformer using DGA data is achieved off-line by manually

extracting oil sample, delivering it to a laboratory, and obtaining the diagnosis results [9]. By carrying out gas detection techniques to the oil sample, the types and concentration of dissolved gases can be measured. Then, faults are detected by the relationship among different gas concentrations or the individual gas concentration itself. Many international standards are implemented to determine the fault, where an evaluation of the impact of a fault on the serviceability of a power transformer can be obtained. Once any exceeded suspicious gas is detected, further inspections need to be implemented to identify the possible locations of faults, for example, no-load test of winding DC resistance, test of insulation condition, location test of partial discharge or humidity content measurements, etc.

The lifespan is largely dependent up the design and condition of insulation. Recently, the lifespan has been extended due to improvements and innovation in insulating materials. The application of new insulation components is one of the key factors to prolong its service life. Apparently, the power transformers are always subject to electrical and thermal stresses [24] [25] [26]. These two stresses could break down insulation materials and release gaseous decomposition products, which may lead to further damages [27]. In an oil-immersed power transformer, the oil serves the dual purposes of providing insulation and acting as a cooling medium to conduct away the losses which occur in the transformer in the form of heat. The gases, which might be generated by faults or incipient faults, could dissolve in the insulation oil, where there exists a dynamic equilibrium as a result of many environmental factors [28] [29]. Recently, DGA and its interpretation rules have become the main research area. Various diagnostic schemes have been developed. These methods try to reveal the relationship between gases and fault types.

For key gas method, oil-filled transformers generate a small quantity of gas to some extent in normal operation conditions, especially carbon monoxide (CO) and carbon dioxide (CO<sub>2</sub>), three primary causes, overheating, partial discharge and arcing, lead to a relatively large amount of the corresponding gases. Such internal faults in oil produce gaseous byproducts mainly include hydrogen (H<sub>2</sub>), methane (CH<sub>4</sub>), acetylene (C<sub>2</sub>H<sub>2</sub>), ethylene (C<sub>2</sub>H<sub>4</sub>) and ethane (C<sub>2</sub>H<sub>6</sub>). Faults existed in a different place can produce different gases. For instance, if a fault

exists in cellulose insulation material,  $\text{CH}_4$ ,  $\text{H}_2$ ,  $\text{CO}$  and  $\text{CO}_2$  can be produced simultaneously or asynchronously. These gases are generally combustible. Anyone or a combination of thermal, electrical or corona faults may cause a speedily increase of gas generating rates. Based on long term experience of maintenance, main difficulties of fault detection are that these faults may exist simultaneously or asynchronously. Also, interaction of different faults always happen. Because the gas generation is an interactive process in power transformer, clear thresholds of gas values are hard to determine during fault detection. Many gas features are attempted to be used for fault detection of a power transformer. For example, certain value combinations of separate gases, called Key gases [1], are used to represent general fault types, such as overheated oil, overheated cellulose, corona in oil and arcing in oil. On the other hand, the ratios of certain key gas concentrations are applied to detect the specific details of fault types, for instance, thermal fault  $> 700^\circ\text{C}$  and thermal fault  $< 700^\circ\text{C}$ .

In this chapter, an usual operative procedure of dissolved gas analysis is introduced firstly. Then, evolution of gas and combustible gassing rate is discussed for the detection of faulty gas. Moreover, calculation of gas space and gas equivalents is taken into account. Various interpretation methods are discussed for improving the DGA reliability. Finally, a detailed discussion of current DGA methods is provided.

## 2.2 Operating Procedures of DGA

Three procedures typically need to be taken into consideration in a power transformer maintenance, which are the detection, evaluation and action [3]. General procedures of DGA are shown in Figure 2.1, which mainly present the detection and evaluation. The first one represents that any gases exceed ‘normal’ quantities necessitate to be detected at the earliest possible time in order to minimise damage or avoid a failure. The second procedure is to measure the level of abnormality effect on the serviceability of a transformer based on a set of guidelines or rules. The action procedure is to take the recommended action, which may be



either an increased surveillance for supplementary analysis, a determination of load sensitivity, a decrease in the load on the transformer, or the removing the unit from service if bad condition occurred. Prior to that, basics of evolution of gas in oil as well as combustible gassing rate need to be figured out. Also, dissolved gas-in-oil equivalents may need to be considered during gas sampling.

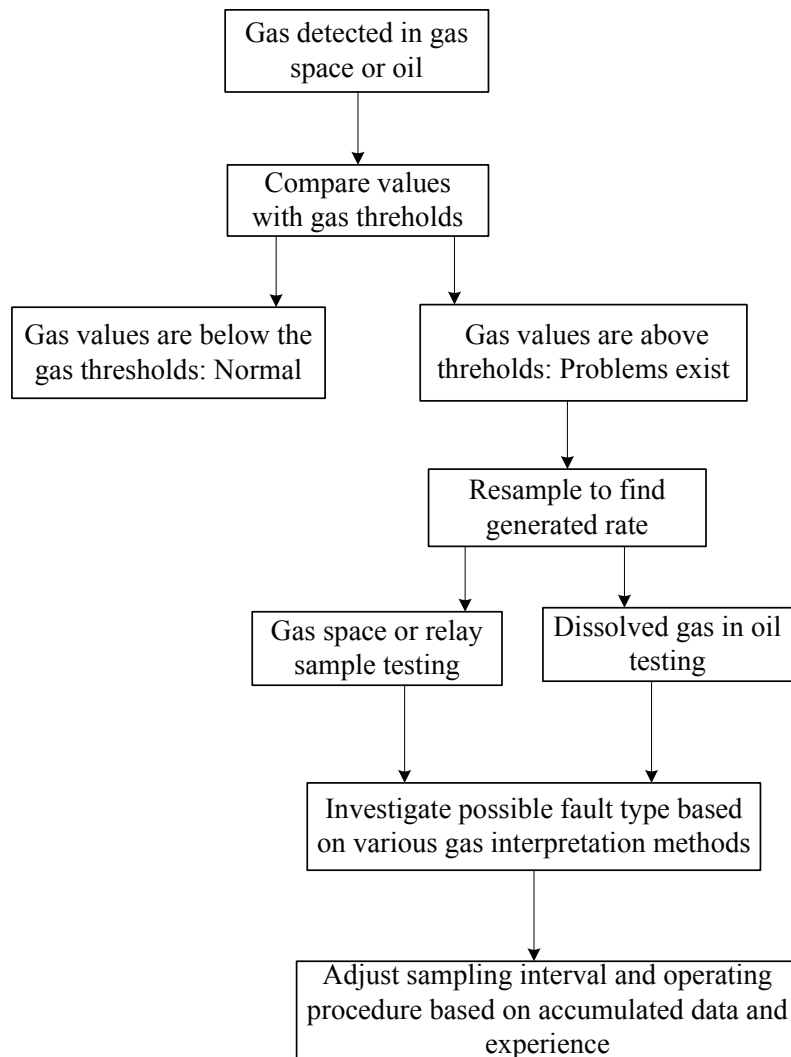


Figure 2.1: Operating procedures of DGA [1]

### 2.2.1 Evolution of Gas

It is great concern about the generation progress of gases due to the aforementioned operation pressures of a power transformer. With a long-term electrical stresses and thermal stresses [30] [31], its insulation materials are broken down with gaseous decomposition products, typical gases are  $H_2$ ,  $CO$ ,  $CO_2$ ,  $CH_4$ ,  $C_2H_6$ ,  $C_2H_4$  and  $C_2H_2$ . Gas bubbles could arise in oil if one of them certain level is exceeded.

In fact, as a result of the energy generated by a fault, breakdown of the hydrocarbon molecules is generally caused, which free radicals are then produced as shown in Figure 2.2. These free radicals subsequently combine with each other to produce low molecular weight hydrocarbon gases. The complicated chemical

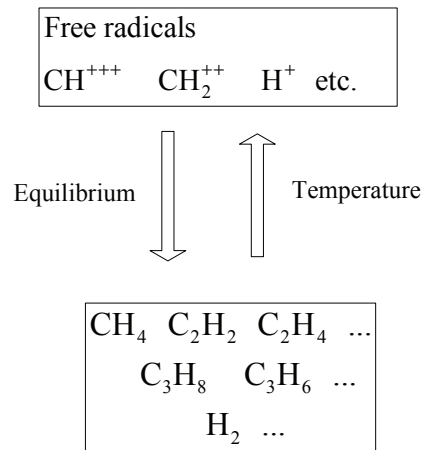


Figure 2.2: Free radicals due to heating of mineral oil [1]

process not only depends on the operation temperatures, but also influenced by faults such as partial discharge, low energy discharge and high energy discharge. Newly formed unstable radical or ionic fragments will recombine swiftly into gas molecules like hydrogen ( $H-H$ ), methane ( $CH_3-H$ ), ethane ( $CH_3-CH_3$ ), ethylene ( $CH_2=CH_2$ ), acetylene ( $CH=CH$ ),  $CO$  ( $C \equiv O$ ) and  $CO_2$  ( $O=C=O$ ). Different energy levels are required to break different kind of molecular bonds. Therefore, different types and amounts of fault gases will be formed according to the severity and category of the transformer fault. Experimental bond entropies for several important radical was given by Stephen in [2], and several important values of energy

Table 2.1: Bond dissociation energy [2]

Bond	C-C (CH <sub>3</sub> - CH <sub>3</sub> )	C-H	C = C (H <sub>2</sub> C = CH <sub>2</sub> )	C ≡ C (HC ≡ CH)	H-H
Energy (kJ/mol)	376	337.2	682.2	962	436.0

Notes: 1 kcal/mol= 4.184 kJ/mol

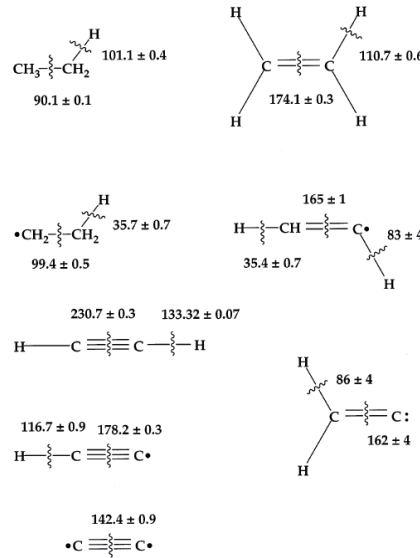


Figure 2.3: Experimental bond entropies for several important radical [2]

needs to crack the typical molecular bond inside the transformer oil is shown in Table. Unit of the values in Figure 2.3 is kcal/mol and unit of the values in Table 2.1 is kJ/mol. As it can be seen from the table, the bond dissociation energy is in the order:  $\text{CH}_4 < \text{H}_2 < \text{C}_2\text{H}_6 < \text{C}_2\text{H}_4 < \text{C}_2\text{H}_2$ . Obviously, the largest bond energy of  $\text{C}_2\text{H}_2$  indicates that only a small concentration of  $\text{C}_2\text{H}_2$  means a serious fault of a power transformer. A general relationship among gases appearing, discharge and temperature are shown in Figure 2.4 [1]. The analysis of bond energy is also demonstrated by the appearance order of gases in the figure. It is noted that no temperature scale is indicated along the temperature axis of Figure 2.4. When the temperature increase to  $150^\circ\text{C}$ , both  $\text{CH}_4$  and  $\text{H}_2$  are generated, with  $\text{CH}_4$  existing

predominant. When the temperature increases,  $C_2H_6$  starts to be predominant gas with a reduced  $CH_4$ , so that the  $C_2H_6/CH_4$  ratio becomes an apparent pattern. As the temperature goes higher, the rate of  $C_2H_6$  evolution is reduced and  $C_2H_4$  production commences and soon outweighs the proportion of  $C_2H_6$ . If the temperature reaches to a high value,  $C_2H_4$  will be produced. As the temperature increases still further, it can become the most predominant gas. When the temperature reaches  $500^\circ C$ ,  $C_2H_2$  will be produced and become a dominant gas. In general, hydrogen and methane begin to form in small amounts at around  $150^\circ C$ , whereas ethane ( $C_2H_6$ ) begins

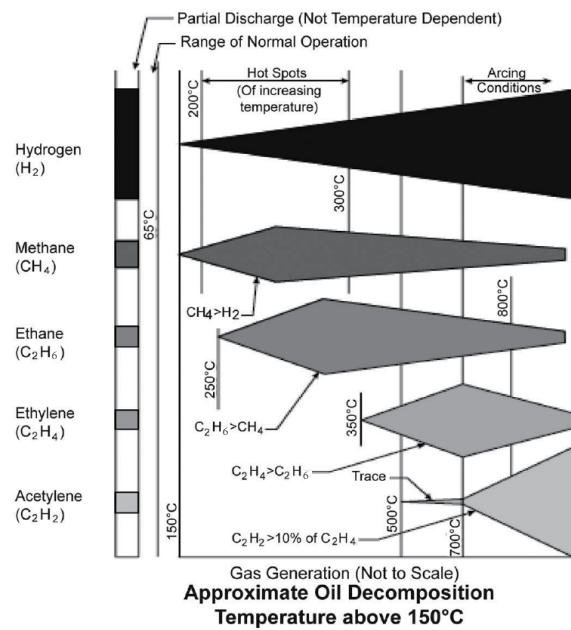


Figure 2.4: Oil decomposition temperature over  $150^\circ C$  [3]

to be produced at about  $250^\circ C$  and ethylene ( $C_2H_4$ ) is produced at about  $350^\circ C$ . Acetylene ( $C_2H_2$ ) production starts between  $500^\circ C$  and  $700^\circ C$ . In the past, trace amounts of acetylene ( $C_2H_2$ ) was considered to be an indication of a temperature of at least  $700^\circ C$ ; however, recent work has led to the conclusion that a thermal fault (hot spot) of  $500^\circ C$  can produce a few parts per million of the gas [3]. It is interesting to note that larger amounts of acetylene can only be produced above  $700^\circ C$  by internal arcing. The production of methane surpasses hydrogen when the temperature is between  $200^\circ C$  and  $300^\circ C$ . Starting at about  $270^\circ C$  and on up,

the production of ethane exceeds methane. At about 450°C, hydrogen production exceeds all others until about 750°C to 800°C; then more acetylene is produced. A small amount of H<sub>2</sub>, CH<sub>4</sub>, and CO continue to be produced by normal aging. Thermal decomposition of oil-impregnated cellulose usually produces CO, CO<sub>2</sub>, H<sub>2</sub>, CH<sub>4</sub>, and O<sub>2</sub>. Decomposition of cellulose insulation normally begins at only about 100°C or less.

### 2.2.2 Determination of Combustible Gassing Rate

The volume of a detected gas might be repeatedly generated over a long time period by an insignificant fault, or it may be produced in a very short period of time by severe mentioned faults simultaneously. Obviously, the gas generation rate and the severity of a fault cannot be represented by one measurement. Once there is a existence of suspicious gas, it is vital to test again and obtain the gassing rate of the gas, which can be applied to determine whether the generated gas is active or not. Normally, an evolution rate greater than 2.8 L (0.1 ft<sup>3</sup>) of combustible gas per day may indicate the unit has an active internal fault [1]. The equation for computing gassing rate is as below [22]:

$$r_i = \frac{(S_{i1} - S_{i2}) \times V \times 10^{-6}}{t}, \quad (2.2.1)$$

where  $r_i$  is the rate (liters/day),  $S_{i1}$  is the first sample (microliters/liter),  $S_{i2}$  is the second sample (microliters/liter),  $V$  is the tank oil volume (liters),  $t$  is the actual operating time of a sampling interval (day). To calculate the rate of evolution, take the sum of the concentrations of all the combustible except CO<sub>2</sub>, O<sub>2</sub> and N<sub>2</sub>. Limits for average gas generation rates are provided for total combustible gas (TCG) in Table 2.2 and for analysis of total dissolved combustible gas (TDCG) in Table 2.3.

#### Determining the transformer sampling interval utilising TCG in the gas space

Table illustrates the recommended initial sampling intervals and operating procedures for various levels of TCG (in percentage). The sampling interval time are classified into four level conditions. Once the source of gassing is determined by analysis, inspection, consultation, or combinations and the risk

has been assessed, then engineering judgment should be used to determine the final sampling interval by using the following operating procedures.

Table 2.2: Actions based on TCG gas rate [1]

	TCG levels (%)	TCG rate(%)	Sampling interval
Condition 4	$\geq 5$	$>0.03$	Daily
		0.01-0.03	Daily
		$<0.01$	Weekly
Condition 3	$\geq 2$ and $< 5$	$>0.03$	Weekly
		0.01-0.03	Weekly
		$<0.01$	Monthly
Condition 2	$\geq 0.5$ and $< 2$	$>0.03$	Monthly
		0.01-0.03	Monthly
		$<0.01$	Quarterly
Condition 1	$< 0.5$	$>0.03$	Monthly
		0.01-0.03	Quarterly
		$<0.01$	Annual

The recommended operating procedures for condition 4 are : 1. Consider removal from service; 2. Exercise extreme cautions and does analysis for individual gases; 3. Plan outage. Normal operating procedures for condition 3 are: 1. Exercise utmost caution; 2. Do analysis for each individual gas; 3. Plan outage and obtains advice from the manufacturer. The recommended operating procedures for condition 2 can be: 1. Exercise cautions; 2. Analysis for individual gases; 3. Determine load dependence. Suggested operational procedure for condition 1 is exercise caution.

### **Determining the sampling interval from the TDCG levels and generating rates in the oil**

When sudden increase of gas exists in the dissolved gas content of the oil in successfully operating transformers an internal fault may be suspected. Table 2.3 indicates the recommended initial sampling intervals for various levels of

TDCG. The sampling interval time of a power transformer is classified into four level conditions. An increasing gas generation rate indicates the problem becomes severity, therefore, a shorter sampling interval is recommended.

Table 2.3: Actions based on TDCG gas rate [1]

	TDCG levels ( $\mu\text{l}/\text{L}$ )	TDCG rate( $\mu\text{l}/\text{L}/\text{day}$ )	Sampling interval
Condition 4	> 4630	>30	Daily
		10-30	Daily
		<10	Weekly
Condition 3	1921-4630	>30	Weekly
		10-30	Weekly
		<10	Monthly
Condition 2	721-1920	>30	Monthly
		10-30	Monthly
		<10	Quarterly
Condition 1	$\leq 720$	>30	Monthly
		10-30	Quarterly
		<10	Annual

Suppose a transformer has a TDCG level of 1700  $\mu\text{l}/\text{L}$  (ppm) and generates gas at a constant rate is smaller than 10  $\mu\text{l}/\text{L}$  (ppm) per day, then the case belongs to condition 2 and the power transformer needs to be sampled quarterly according to the Table 2.3. The suggested operations for the transformer are: exercise caution, analysis for individual gases, and determine load dependence. If the rate increases to a value which is bigger than 30  $\mu\text{l}/\text{L}$  (ppm) per day, the operator must now sample monthly.

### 2.2.3 Computation of Gas Space and Dissolved Gas-in-Oil Equivalents

Gas space and oil equivalents are used to compare the results of analysis of the gas space (TCG) with the results from analysis of the gases dissolved in the oil (TDCG).

Table 2.4: Ostwald coefficient of each gas [1]

Gas	Ostwald coefficient (B)
H <sub>2</sub>	0.0429
O <sub>2</sub>	0.138
CO <sub>2</sub>	0.900
C <sub>2</sub> H <sub>2</sub>	0.938
C <sub>2</sub> H <sub>4</sub>	1.35
N <sub>2</sub>	0.0745
CO	0.102
C <sub>2</sub> H <sub>6</sub>	1.99

Comparisons of gas ratios obtained from the gas space can then be compared to similar ratios of gases extracted from the oil. It should be noted that the calculated equivalent values of TCGe and experimentally measured values of TCG probably do not show close agreement, since the equation for obtaining the equivalents assumes the existence of equilibrium between the gas blanket and the oil. This condition may not exist, particularly in the case of an actively progressing fault. But, the equation is valuable for the determination of a limitation for the expected total combustible gas concentration in the gas blanket. The dissolved gas equivalent of the TCGe is obtained using the following equation:

$$TCGe = \sum_{C1}^{Cn} \frac{\frac{F_c}{B_c}}{\sum \frac{F_g}{B_g}} \times 100, \quad (2.2.2)$$

where:

TCGe : An estimate of the percent of combustible gas in the gas space

C : Combustible gas

G : Each gas dissolved in oil (combustible and noncombustible)

F<sub>c</sub>: The concentration expressed in ppm of combustible gas dissolved in oil

B<sub>c</sub> : The Ostwald solubility coefficient of combustible gas

F<sub>g</sub> : The concentration of a particular gas dissolved in oil

B<sub>g</sub> : The Ostwald solubility coefficient of particular gas



The corresponded Ostwald coefficient for each gas is given in Table 2.4. An operating procedure utilizing the gas data of the power transformer is to be developed immediately following the initial detection of combustible gases.

#### 2.2.4 General Operation Procedure using Dissolved Gas Concentration

Table 2.5: Dissolved gas concentration limits( $\mu\text{l}/\text{L}$ ) [1]

Condition	CH <sub>4</sub>	H <sub>2</sub>	C <sub>2</sub> H <sub>4</sub>	C <sub>2</sub> H <sub>6</sub>	C <sub>2</sub> H <sub>2</sub>	CO	CO <sub>2</sub>	TDCG
1	120	100	50	65	35	350	2500	720
2	120-400	101-700	51-100	66-100	36-50	351-570	2500-4000	721-1920
3	401-1000	701-1800	101-200	101-150	51-80	571-1400	4001-10000	1921-4630
4	> 1000	> 1800	> 200	>150	>80	>1400	>10000	>4630

The initial detection of combustible gas in Figure 2.1 indicates the final assessment of the status of the transformer. The applied gas thresholds are given in Table 2.5. The risks of power transformer are classified into four level conditions. The criterion uses both gas concentration itself and the total concentration of all combustible gases. The total dissolved combustible gas (TDCG) indicates the sum of CH<sub>4</sub> , H<sub>2</sub>, C<sub>2</sub>H<sub>4</sub>, C<sub>2</sub>H<sub>6</sub>, C<sub>2</sub>H<sub>2</sub> and CO. The four conditions are listed as follows:

Condition 1: TDCG below the level indicates the transformer is operating normally. But, if an individual combustible gas exceeding specified levels in Table 2.5, an additional prompt investigation needs to be executed.

Condition 2: TDCG belong to the range indicates greater than normal combustible gas level. Any individual combustible gas exceeding specified levels should prompt additional investigation, such as change the resampling rate.

Condition 3: TDCG belong to the range represents a high level of decomposition. Any individual combustible gas exceeding specified levels should prompt additional investigation. Immediate action should be taken to the power transformer

Condition 4: TDCG over the value indicates excessive decomposition. Continued operation could result in failure of the transformer.

## 2.3 Gas Interpretation Methods

When the procedure reaches the step of possible investigation of fault type base on various gas values, the focus of the procedure naturally is the gas interpretation methods. Three important methods, Key gas method, Gas ratio methods and Duval triangle methods, are investigated. Gas ratio methods contain Rogers ratio method, IEC ratio method and Donernenburg ratio method. Meanwhile, differen versions of Duval triangle are introduced for different types of insulation materials in transformers. All these methods are discussed in the followings.

### 2.3.1 Key Gas Method

Table 2.6: Typical values of key gases [1]

Key gas	Value (ppm)	Suspected fault
$C_2H_2$	>20	Power discharge
$H_2$	>100	Partial discharge
$\sum C_xH_y$	>1000 >500	Thermal fault
$CO_x, x = 1,2$	>10000	Cellulose degradation

The method applies the key gases to detect four fault types [1], including overheating of oil, overheating of cellulose, corona (partial discharge) and arcing. Typical values are given in Table 2.6. The method mainly contains concentrations of  $C_2H_4$ ,  $CO$ ,  $H_2$ ,  $C_2H_2$ ,  $C_2H_6$ . The four rules of qualitative investigation are provided as follows:

1. Overheating of cellulose: Hydrocarbon gases, such as  $CH_4$  and  $C_2H_4$ , are generated when an overheating fault involves an oil-immersed cellulose structure.

Normally, large quantities of  $\text{CO}_2$  and  $\text{CO}$  are produced from an overheated cellulose. In this situation, the principal gas is  $\text{CO}$ .

2. Overheating of oil: Together with small quantities of  $\text{H}_2$ , significant amount of  $\text{C}_2\text{H}_4$ ,  $\text{C}_2\text{H}_6$  and  $\text{CH}_4$  are produced from oil decomposition products. Traces of  $\text{C}_2\text{H}_2$  may be formed if other faults are severe or involve electrical contacts. The principal gas is  $\text{C}_2\text{H}_4$ .

3. Corona:  $\text{H}_2$  and  $\text{CH}_4$  together with small amount of  $\text{C}_2\text{H}_6$  and  $\text{C}_2\text{H}_4$  are generated by low-energy electrical discharges. Comparable amounts of  $\text{CO}$  and  $\text{CO}_2$  may be formed due to discharges in cellulose. In this case,  $\text{H}_2$  is the principal gas.

4. Arcing: Large quantities of  $\text{H}_2$  and  $\text{C}_2\text{H}_2$  are formed, with minor quantities of  $\text{CH}_4$  and  $\text{C}_2\text{H}_4$ .  $\text{CO}_2$  and  $\text{CO}$  may be formed if a fault involves cellulose. Insulation oil may be carbonised.  $\text{C}_2\text{H}_2$  is the foremost gas.

A short summary can be concisely suggested describing relationships between key gases and fault types as follows:

1. Small amount of  $\text{O}_2$  and  $\text{N}_2$  represent that the power transformer generally is normal operation.
2. Large quantities of  $\text{CO}$  and  $\text{CO}_2$  indicate an overheating fault exists in the cellulose insulation.
3. Normally,  $\text{CH}_4$  and  $\text{C}_2\text{H}_6$  point that a low temperature overheating happens in the oil.
4. Generally,  $\text{C}_2\text{H}_4$  indicates a high temperature overheating in the oil.

5. Even small amount of  $C_2H_2$  represent an arcing fault in high temperature.

Because the key gas method provides few numerical correlations between fault types and gas types directly, the method normally is applied as a qualitative investigation.

### 2.3.2 Gas Ratio Methods

The usage of gas ratios to detect a single possible fault type is a trade-off art during fault classification. The ratio range results are obtained by assigning the cause of failure when the unit was examined or normal maintenance. The five ratios are: Ratio 1 (R1) =  $CH_4/H_2$ ; Ratio 2 (R2) =  $C_2H_2/C_2H_4$ ; Ratio 3 (R3) =  $C_2H_2/CH_4$ ; Ratio 4 (R4) =  $C_2H_6/C_2H_2$ ; Ratio 5 (R5) =  $C_2H_4/C_2H_6$ ; Ratio 6 (R6) =  $C_2H_6/CH_4$ . The first ratio method, called Roger ratios [22], utilises three ratios R1, R6, R5 and R2. The Rogers method does not depend on specific gas concentrations to exist in the transformer for the diagnosis. It suggests that the method can be used when the normal limits of the individual gases have been exceeded.

The IEC ratio method originated from the Roger's Ratio method, except that the ratio  $C_2H_6/CH_4$  was dropped since it only indicated a limited temperature range of decomposition as shown in Table 2.7. The faults are divided into nine different types.

The second ratio method, known as Doernenburg Ratio method [23], applies the gas concentration ratio of R1, R2, R3 and R4. The value of the gases at first must exceed the concentration limitation to ascertain whether there is really a problem with the unit.

#### IEC Ratios Method

As a convenient basis for fault diagnosis, the gas ratio methods are coding schemes that assign certain combinations of codes to specific fault types. The codes are generated by calculating ratios of gas concentrations and comparing the ratios with predefined values, which have been derived from experience and modified continually. A fault condition is detected when a gas combination fits the code pattern of a particular fault. The most commonly used gas ratio method

is the IEC ratio method [6] [22] as listed in Table 2.7, which is able to distinguish more types of thermal faults than that of the Dornenberg ratio method [23].

Additional attention should be paid to the following conditions while applying the gas ratio method according to Table 2.7:

1. Significant values quoted for ratio calculations needs to be only regarded as typical.
2. Transformers fitted with an in-tank OLTC may represent faults of code 202/102, depending on transmission of arc decomposition products in the diverter switch tank into the transformer tank oil.
3. The ratios for a combination of multiple faults may not fit the predefined codes in Table 2.7.
4. Combinations of ratios not included in Table 2.7 may occur in practice. A great amount of consideration is being given to the interpretation of such combinations.

Table 2.7: IEC ratio methods [6]

		$\frac{C_2H_2}{C_2H_4}$	$\frac{CH_4}{H_2}$	$\frac{C_2H_4}{C_2H_6}$	
	Ratios of gases				
	< 0.1	0	1	0	
	0.1-1	1	0	0	
	1-3	1	2	1	
	> 3	2	2	2	
Fault types					Typical reasons
0	No fault	0	0	0	Normal aging
1	Partial discharges of low energy density	0	1	0	Discharges in gas-filled cavities resulting from incomplete impregnation, or supersaturation or cavitation or high humidity
2	Partial discharges of high energy density	1	1	0	As above, but leading to tracking or perforation of solid insulation
3	Discharge of low energy	1-2	0	1-2	Continuous sparking in oil between bad connections of different potential, or to floating potential.
4	Discharge of high energy	1	0	2	Discharges with power follow-through. connections of different potential, Arcing - breakdown of oil between windings or coils or between coils to earth.
5	Thermal fault of low temperature T:<150°C	0	0	1	General insulated conductor overheating
6	Thermal fault of low temperature T:150°C-300°C	0	2	0	Increasing hot spot temperatures
7	Thermal fault of low temperature T:300°C-700°C	0	2	1	Small hot spots in core, shorting links in core, overheating of copper due to eddy currents, bad contacts/joints concentrations of flux.
8	Thermal fault of high temperature T:>700°C	0	2	2	As above, regular hot spot, tank circulating currents

### Doernenburg Ratio Method

This method utilises the gas concentration from ratio of  $\text{CH}_4/\text{H}_2$ ,  $\text{C}_2\text{H}_2/\text{CH}_4$ ,  $\text{C}_2\text{H}_4/\text{C}_2\text{H}_6$  and  $\text{C}_2\text{H}_2/\text{C}_2\text{H}_4$ . The value of the gases at first must exceed the limitation values in Table 2.8 [1] to ascertain whether there is really a problem with the unit and then whether there is sufficient generation of each gas for the ratio analysis to be applicable. According to IEEE Standard C57.104 [1], the step-by-step procedure to diagnose faults using Doernenburg ratio method is:

Table 2.8: Concentration limits of Doernenburg ratio method [1]

Key Gas	Concentrations (ppm)
$\text{H}_2$	100
$\text{CH}_4$	120
$\text{CO}$	350
$\text{C}_2\text{H}_2$	35
$\text{C}_2\text{H}_4$	50
$\text{C}_2\text{H}_6$	65

Step 1. Gas concentrations are obtained by extracting the gases and separating them by chromatograph.

Step 2. If at least one of the gas concentrations (in ppm) for  $\text{H}_2$ ,  $\text{CH}_4$ ,  $\text{C}_2\text{H}_2$ , and  $\text{C}_2\text{H}_4$  exceeds twice the values for limits in table above and one of the other three gases exceed the values for limitation, the unit is considered faulty. Step 3 needs to be executed.

Step 3. Determining validity of ratio procedure: If at least one of the gases in each ratio  $\text{CH}_4/\text{H}_2$ ,  $\text{C}_2\text{H}_2/\text{CH}_4$ ,  $\text{C}_2\text{H}_2/\text{CH}_4$  and  $\text{C}_2\text{H}_6/\text{C}_2\text{H}_2$  exceeds legitimation, the ratio procedure is valid. Otherwise, the ratios are not significant, and the unit should be resample and investigated by alternative procedures.

Step 4. Assuming that the ratio analysis is valid, each successive ratio is compared to the values obtained from Table 2.9 in the order of ratio  $\text{CH}_4/\text{H}_2$ ,  $\text{C}_2\text{H}_2/\text{CH}_4$ ,  $\text{C}_2\text{H}_2/\text{CH}_4$  and  $\text{C}_2\text{H}_6/\text{C}_2\text{H}_2$ , where NS is short for not significant.

Step 5. If all succeeding ratios for a specific fault type fall within the values given in Table 2.9, the suggested diagnosis is valid.

Table 2.9: Fault diagnosis concentration limits of Doernenburg ratio method [1]

Fault Diagnosis	$\text{CH}_4/\text{H}_2$		$\text{C}_2\text{H}_2/\text{C}_2\text{H}_4$		$\text{C}_2\text{H}_2/\text{CH}_4$		$\text{C}_2\text{H}_6/\text{C}_2\text{H}_2$	
	Oil	Gas space	Oil	Gas space	Oil	Gas space	Oil	Gas space
Thermal Fault	>0.1	>0.1	<0.75	<1.0	<0.3	<0.1	>0.4	>0.2
Partial Discharge	<0.1	<0.01	NS		<0.3	<0.1	>0.4	>0.2
Arcing	0.1-1.0	0.01-1.0	>0.75	>1.0	>0.3	>0.1	<0.4	<0.2

### 2.3.3 Duval Triangle Methods

A ternary graphic, which plots the normalized proportions of three substances in a triangle, was introduced by Duval for DGA data visualisation. Firstly, to determine whether a problem exists, gas thresholds in the following Table 2.10 [32] are applied for predefine assessment. At least one of the individual gases must at the concentration or the gas generation rate at least at G2 and G1. Then, fault will be determined by using Duval triangle graphic.



Table 2.10: Concentration limits of Duval ratio method [7]

Key Gas	Concentrations	G1 Limits (ppm per month)	G2 limits (ppm per month)
H <sub>2</sub>	100	10	50
CH <sub>4</sub>	75	8	38
CO	700	70	350
C <sub>2</sub> H <sub>2</sub>	3	3	3
C <sub>2</sub> H <sub>4</sub>	75	8	38
C <sub>2</sub> H <sub>6</sub>	75	8	38
CO <sub>2</sub>	7000	70	350

Duval proposed several versions of triangle methods. The classical Duval Triangle 1 is for equipment filled with mineral oil. The Duval Triangle 2 is proposed for load tap changers of the oil type. Triangle 3 is for non-mineral oil transformer. The main difference is that normal operation of load tap changers may involve arcing in oil.

### Duval Triangle 1

The classical Duval triangle method [4] can be applied when there is some suspicion of faults, based on an increase in combustible gas or some other suspicious symptom. The Triangle graphical method of representation is used to visualize the different cases. The coordinates and limits of the discharge and thermal fault zones of the Triangle are indicated in Figure 4.2. It shows the classification rules and the coded list of faults are: PD = partial discharges; D1 = discharges of low energy; D2 = discharges of high energy; T1 = thermal faults of temperature  $< 300^{\circ}\text{C}$ ; T2 = thermal faults of temperature  $300^{\circ}\text{C} < T < 700^{\circ}\text{C}$ ; T3 = thermal faults of temperature  $> 700^{\circ}\text{C}$ . The Triangle coordinates corresponding to DGA results in ppm can be calculated as follows:  $\text{C}_2\text{H}_2 = 100x / (x+y+z)$ ;  $\text{C}_2\text{H}_4 = 100y / (x+y+z)$ ;  $\text{CH}_4 = 100z / (x+y+z)$ , with  $x = (\text{C}_2\text{H}_2)$ ;  $y = (\text{C}_2\text{H}_4)$ ;  $z = (\text{CH}_4)$ , in ppm. All the thresholds are illustrated in the Figure 4.2. In [4], one hundred and seventy-nine cases of faults in transformers in service as well as 19 cases of faults simulated in the laboratory have been examined by the

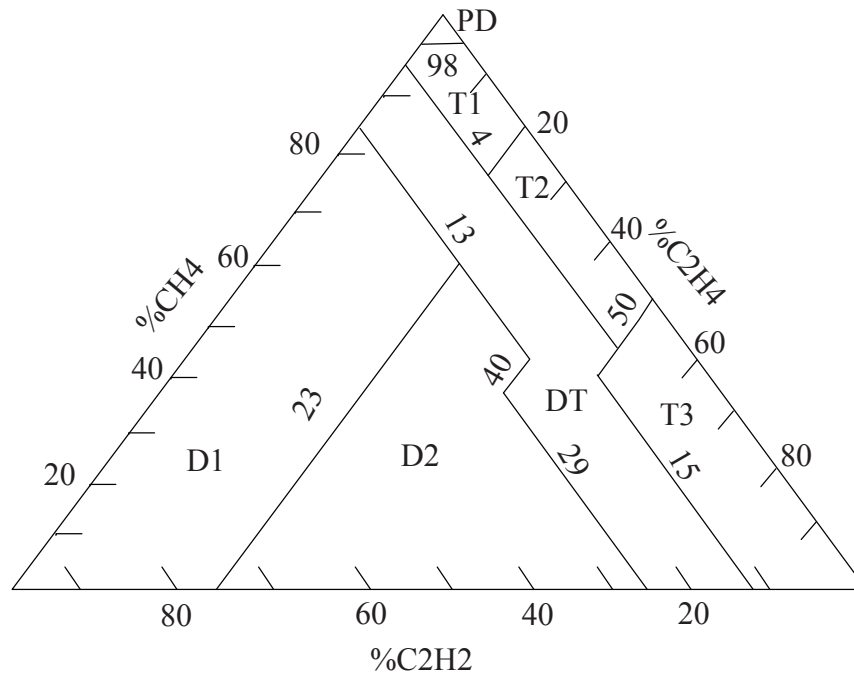


Figure 2.5: Duval triangle 1 [4]

method. From these cases, six main types of faults zone can be established (PD, D1, D2, T1, T2, T3). Among these, faults T3 in service tend to be related to hot spots in oil and faults [4]. PD faults are potentially harmful to the equipment, and some of them remain undetected. The application of Duval Triangle 1 to load tap changers has been examined, with indications on high reliable detection of hot spots and abnormal arcing.

### Duval Triangle 2 for Load Tap Changers with oil

Duval triangle 1 applies to transformers filled with mineral oils, but not directly to load tap changers (LTCs) of the oil type, where normal operation involves arcing in oil. Also, equipment can be filled with non-mineral oils (e.g., natural or synthetic esters and silicones). Diagnosis for low-temperature faults may be affected by the “stray gassing” of some types of oils. Duval proposed a new version of the Duval Triangle for such cases [5].

The normal operation of load tap changers (LTCs) of the oil type involves

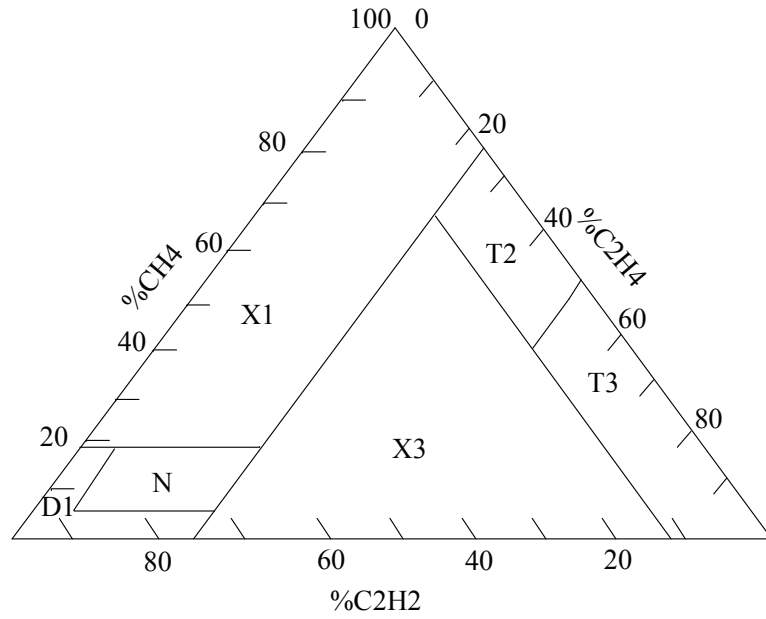


Figure 2.6: Duval triangle 2 [5]

arcings in the oil. The Duval triangle 2 for LTCs of the oil type, taking this into account in a more user-friendly manner than in a previous triangle method, is presented in Figure 2.6. Zone boundaries in the Duval triangle 2 for LTCs of the oil type are based on the published cases of inspected cases of faults. DGA results are obtained based on the inspected cases in Duval's paper records. Related fault cases, reported in [33], also fit well in it. The report of CIGRE TF D1-01-15 [34] also provides additional cases of faulty or normally operating LTCs, which also fitting nicely in Figure 2.6.

Table 2.11: Identification of fault zones in Duval Triangle 2 [5]

Zone	Identification
N	Normal operation
T3	Severe thermal fault T3 ( $T > 700^{\circ}\text{C}$ ), heavy coking
X3	Severe thermal fault T2 ( $300 < T < 700^{\circ}\text{C}$ ), coking
T2	Fault T3 or T2 in progress with light coking
D1	Abnormal arcing D1 (outside of zone N).
X1	Abnormal arcing D1 or thermal fault in progress

The identification of fault zone in Figures 2.6 is indicated in Table 2.11. Numerical zone boundaries in Figures 2.6 are indicated in Table 2.12. The numerical zone boundaries indicated in Table 2.11 for the N (normal operation) zone cover all types of LTCs of the oil type and may be used by default. However, the N zone may be smaller for some individual types or brands of LTCs of the oil type, and its actual boundaries can be determined by using DGA results from such individual units which have been newly installed or where normal operation is ascertained.

Table 2.12: Numerical zone boundaries of Figure 2.6 [5]

Zone	Value (in %)
N	$\text{CH}_4=19, \text{C}_2\text{H}_4=23, \text{CH}_4=2, \text{C}_2\text{H}_4=6$
T3	$\text{C}_2\text{H}_4 = 50, \text{C}_2\text{H}_2 = 15$
X3	$\text{C}_2\text{H}_4 = 23, \text{C}_2\text{H}_2 = 15$
T2	$\text{C}_2\text{H}_4 = 23, \text{C}_2\text{H}_2 = 15, \text{C}_2\text{H}_4 = 50$
D1	$\text{CH}_4 = 19, \text{C}_2\text{H}_4 = 6, \text{CH}_4 = 2, \text{C}_2\text{H}_4 = 23$
X1	$\text{CH}_4 = 19, \text{C}_2\text{H}_4 = 23$

Fault diagnoses should not be attempted in LTCs if concentrations of  $\text{C}_2\text{H}_2$  and  $\text{C}_2\text{H}_4$  are  $< 10$  ppm, because of possible contamination and uncertainty of laboratory results. When oil in an LTC is removed and replaced by new oil, some of the removed (previous) oil remains on metallic parts and can

be evaluated by extracting it with a solvent, then evaporating the solvent and measuring the amount of extracted oil (typically 0.2% of the LTC oil volume but this may depend on the type of LTC used). This contamination by the previous oil may need to be subtracted from DGA results in the new oil, depending on the respective gas concentrations in the previous and the new oil. For example, if the concentration of a gas was 10,000 ppm in the previous oil, contamination by this gas in the new oil will be 20 ppm and may need to be subtracted from the concentration measured in the new oil if the latter is relatively low (e.g.,  $< 10$  times the contamination, or 200 ppm).

### **Duval Triangle 3 for Non-Mineral Oils**

Since early 1980s, cooper power systems has been actively involved in exploring and developing ester-based dielectric fluid, and the first commercialised ester was a synthetic ester in 1984 [35]. Synthetic ester dielectric coolants have better cold temperature flow and improved lubricity. End-users observed that the annual failure rate was reduced dramatically with synthetic esters. However, synthetic ester dielectric coolants are expensive to produce. Because of many chemical similarities between the synthetic esters and certain natural esters. More cost-effective, ester chemistries are applied in power transformer [36]. Experimental investigations on insulating liquids, which mainly contain mineral, ester and silicon oils, have been done in [37], where the characteristics such as dielectric strength, heat transfer efficiency, aging, electrostatic charging tendency (ECT), gassing tendency, and the stray gassing issue were analysed. The works show that break down voltage (BDV) close to that of mineral oil while after aging, natural esters generally keep a good BDV and are even sometimes better than mineral oils. Some natural esters have oxidation stability as good as noninhibited mineral oil with correct increase of acidity and tan delta. As the increasing application of non-mineral oil, new DGA interpretation methods are needed for them. In other words, the existing methods used for mineral oils should be adjusted for non-mineral oils [5].

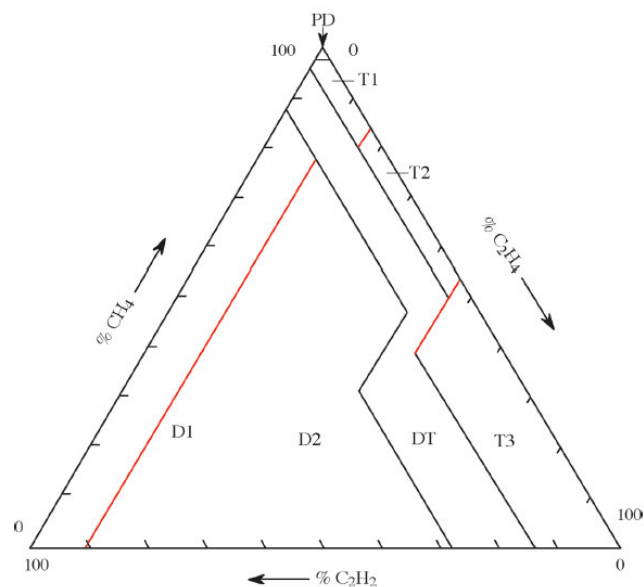


Figure 2.7: Duval triangle 3 of silicone oil [5]

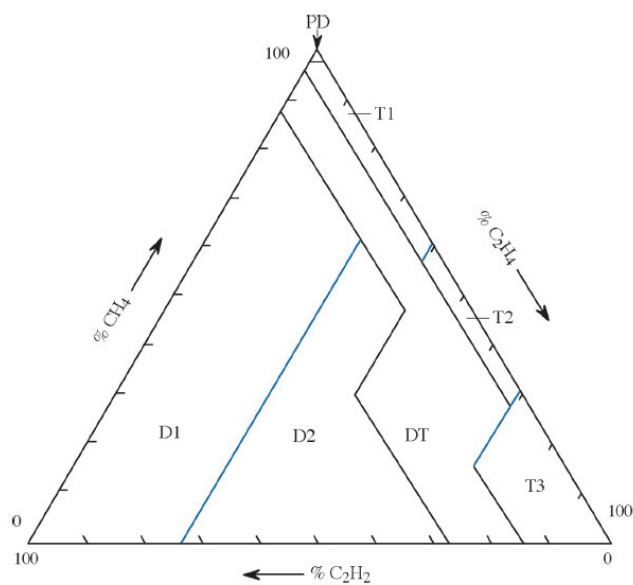


Figure 2.8: Duval triangle 3 of synthetic ester [5]

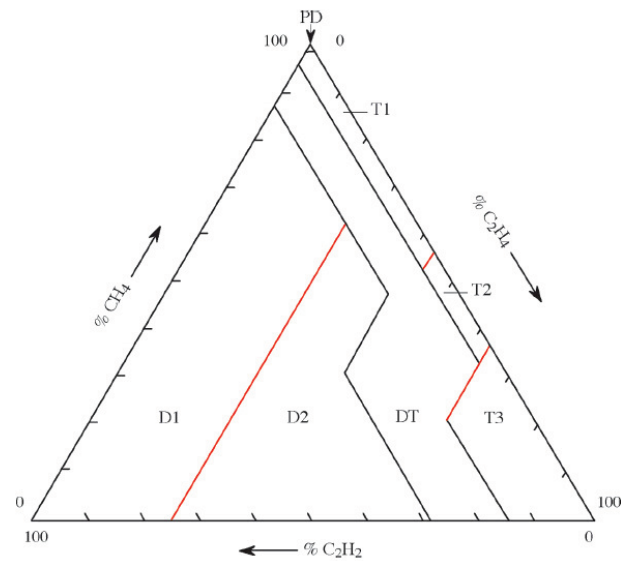


Figure 2.9: Duval triangle 3 of natural esters [5]

Table 2.13: Zone boundaries (in  $C_2H_4\%$ ) specific for non-mineral oils in the Duval Triangle 3 for non-mineral oils [5]

Boundary zones	Mineral oil	Silicone	Midel	FR3	BioTemp
D1/D2	23	9	26	25	20
T1/T2	20	16	39	43	52
T2/T3	9	(46)	(68)	63	(82)

However, very few inspected cases of faults in equipment filled with non-mineral oils are available, because these fluids have been used only for a small number of years and in a limited quantity of equipment. To evaluate gas formation patterns in these fluids, therefore, one can only rely on tests simulating faults in the laboratory, and performed in parallel on both mineral oils and the new fluids such as, silicone oil, synthetic ester (Midel), and natural esters/ vegetable oils (FR3 and BioTemp). The different thresholds of gas in Figure 2.7, Figure 2.8, Figure 2.9 and Figure 2.10 are obtained by using faulty data from the corresponding insulation materials [38] [39]. A Duval Triangle

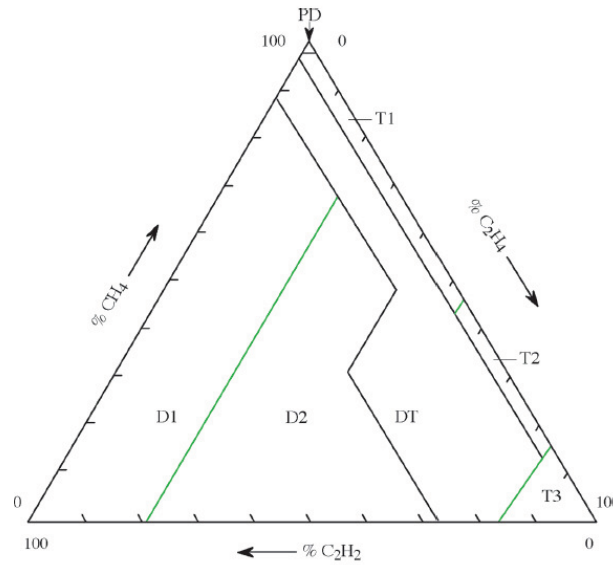


Figure 2.10: Duval triangle 3 of vegetable oils [5]

3 for each of the non-mineral oils is illustrated in the above figures. Zone boundaries of the Duval Triangle 3 for non-mineral oils are the same as those of the Duval Triangle 1 for mineral oils, but the boundaries (in  $C_2H_4\%$ ) between zones D1/ D2, T1/ T2, and T2/ T3 are different and shown in the Table 2.13.

#### 2.3.4 Further Issues on Dissolved Gas Analysis

Experimental results in [40] review the factors that affect the quality and reliability of gas-in-oil analysis. Air bubbles of the oil volume could play an important role in affecting the hydrogen concentration. Storage temperature is also a key factor, which can lead to strong variations of gas-in-oil concentrations due to ongoing chemical reactions, e.g. stray gassing or chemical equilibrium with aging products. It strongly recommends the storage place should be in a dark place below  $20^\circ C$  without air bubbles.

It is important to establish the following evaluation procedures using combined DGA criteria, which are rooted on the guidelines from IEC [9], IEEE [1] and the new modification recommended by CIGRE Task Force 15.01.01 [34].



1. Detection and comparison:

- a. Detect concentrations and gassing rates of any gases dissolved in the oil, and compare them with 'normal' quantities using appropriate guidelines. Then it is certain whether an abnormality occurs in a transformer or not.
- b. A recent investigation on DGA undertaken by CIGRE TF 15.01.01 has set up a table with typical values for the key gases  $H_2$ ,  $C_2H_2$ , the sum of the  $C_1$  and  $C_2$ -hydrocarbons and the sum of  $CO_2$  and  $CO$  for generator and transmission transformers as shown in Table 2.6 [41]. The key gases and the gas concentration values showed in Table 2.6 can be understood as a guideline for DGA interpretation. This is particularly valuable where no additional information is available from historical data of a transformer. However, generally the gassing rate of fault-generated gases is more important than absolute levels, e.g. high levels of key gases can exist with no faults present.
- c. Attention should also be paid to  $CO$  and  $CO_2$  when it is suspected that cellulose materials are involved. The high temperature degradation of cellulose, no matter how it is caused (e.g. hot spots or arcing), tends to increase the relative amount of  $CO$ . However, the rates of  $CO_2$  and  $CO$  production depend greatly upon the oxygen availability, moisture contents and the temperature of degradation. The ratio of  $CO_2/CO$  primarily indicates the participation of cellulose insulation materials in electrical or thermal related faults. Normally, in case of overheating of cellulose, the ratio is greater than 10 and in case of degradation of cellulose caused by an electrical fault, the ratio is less than 3 [41].
- d. Additionally, a new ratio  $C_2H_2/H_2$  is introduced by CIGRE TF 15.01.01 to determine whether fault gases diffuse into a tank from a leaking OLTC or not (if a diverter switch tank and a main tank have a common conservator, it is a similar situation). In this case, normally the ratio is 2 and the concentration of  $C_2H_2$  is 30 ppm [41].
- e. When an internal fault is suspected, the gas ratio methods and the key gas method should be combined to identify the type of faults.

2. Assessment: Based upon the combined assessment results using various

DGA guidelines, further inspections should be carried out to identify the type and location of faults, such as tests of no-load characteristics of winding DC resistance, insulation, partial discharge and humidity content measurements, followed by the evaluation of the impact of the fault on the serviceability of the observed transformer.

3. Action: Recommended actions should be taken, such as increasing surveillance, shortening sampling intervals, reducing the load on the transformer and finally removing the unit from service.

## 2.4 Summary

Literatures of DGA techniques have been reviewed. It is probably one of the most effective methods for monitoring the condition of oil-filled electrical equipment such as transformers. Nearly every possible fault generates one or more gases arising from the consequential increased degradation of adjacent oil or cellulosic insulation. DGA can be recognised as a tool to detect many faults. Furthermore, since in the early stages of these faults as the gases dissolve in the oil, they can be detected at some subsequent point if an oil sample is taken in time. Because fault gases can be detected at very low levels, the DGA technique is very sensitive and eminently suitable for detecting faults at an early stage.

Based on different interpretation methods of DGA, the correlations among gas types, gas concentrations and fault types are summarised. Then, conventional DGA evaluation procedures are presented and a combined DGA criterion is introduced involving the Key gas method, the Rogers ratio method, the gassing rate. However, at the current stage, it must be recognised that analysis of these gases and interpretation of their significance is not a science but an art subject to variability.

Furthermore, the performance of DGA is also dependent on equipment variables. The first one is the type, location, and temperature of the fault. The second one is solubility and degree of saturation of various gases in power transformer oil. The type of oil preservation system also needs to be considered. The type and rate of oil should also apply to the calculation. Variables in the environment associated

with the sampling and measuring procedures should also take account. Due to the variability of acceptable gas limits and the significance of various gases and generation rates, consensus gas thresholds are hard to obtain. The principal obstacle to the development of fault interpretation as an exact science is the lack of clear correlation of the fault-identifying gases with faults found in actual transformers and also new pattern recognition techniques need to be applied to solve this problem.

## **Chapter 3**

# **Study and Analysis of DGA with Sampling Errors**

DGA has been reviewed in the preceding chapter. Fault interpretation methods are all based on the DGA gas data records without considering sampling errors. This chapter focuses on the study and analysis of DGA with reasonable sampling errors. The sampling errors are simulated by variation rates of selected gas. Newly variants of DGA gas records are generated using the variation rates. Duval Triangle method and IEC ratio method are re-examined by the classification of DGA gas records and their variants. The classification results are discussed in detail. Three specific zones of Duval Triangle are proposed for improving its reliability. Typical misclassification fault cases of each zone are summarised.

### **3.1 Introduction**

DGA has been performed mostly by periodically sampling oils from power transformers and analysing the dissolved gas components in laboratories. With a large number of the transformer population soon approaching the end of their designed life [42], frequent inspections including DGA monitoring need to be carried out in order to ensure the timely diagnosis of incipient faults and implement necessary maintenance plans. At some point, laboratory DGA analysis becomes less attractive,

concerning the economic importance and safe operations of power transformers. As the multi-gas online monitors have become commercially available, some of them have already been installed on old transformers to continuously monitor their condition. The tiny deviation between the actual value and value measured by these on-line monitors enhances the DGA reliability.

On-line monitors can achieve the continuous detection of abnormal gassing in service in comparison to regular laboratory analysis, which can be recognised as a relatively robust mean for an effective in prolonging the life span of a power transformer. However, a large number of transformers are still monitored by using laboratory analysis. For laboratory analysis, gas leakage and air ingress might occur during sample transportation and measurement delay, which can be identified as the main reasons for the deviations between the online and the laboratory analysis. Even a short delay between the sampling of transformer oils and the laboratory analysis can cause errors. Sometimes, they are large enough to affect the final DGA detection. However, all the current interpretation methods are established based on the data records without considering these deviations. Recently, research results [16] illustrate that the online gas measurements agree with the laboratory analysis are generally within a 30% deviation. Basically, gas data records of current standards are almost obtained using the results of laboratory analysis [9]. It is worth to re-examine current interpretation methods with a reasonable error range.

The research works are accomplished for dual purposes. The first one is to highlight the specific zones of Duval Triangle in order to attract extra cautions of power engineer if the data samples are detected in these zones during application. The second one is to obtain the error redundancy of Duval Triangle and complete a profound discussion of its thresholds. In this chapter, DGA measurement methods are introduced at first. Then gas variation values are discussed in detail by concerning the inaccuracy in laboratory dissolved-gas measurements [8]. All the IEC10 simulated gas values are considered a  $\pm 5\%$  variation, and a  $\pm 10\%$  variation is applied to all gas data obtained from visual inspection of faulty transformers.

## 3.2 DGA Measurement Methods

### Online DGA Method

The liquid was circulated in the sealed system and passed through a gas monitor. The monitor continuously detected the type and amount of fault gases generated every hour. After the experiment, the monitor may be kept running for further hours in order to let the fault gases go until it reaches equilibrium between the headspace and liquid phases.

The monitor extracted dissolved gases through a gas-liquid membrane extractor, using a headspace equilibrium method, so that the amount of dissolved gases in the liquid phase could be identified from the amount of gases in the gas phase when an equilibrium state was reached. After that, concentrations of fault gases in the gas phase were determined by a built-in gas chromatography (GC). The gases passed through a series of GC columns, where the different gases were separated with helium carrier gas. Concentrations of separated gases were detected by a specialized high-sensitivity thermal conductivity detector (TCD) that met or exceeded the sensitivity requirements. Finally, the gas concentration in the headspace phase was calculated back to the concentration of dissolved gas in the liquid. The influence of temperature and pressure needs to be considered in the calculation. During the measurements, system calibration was normally performed periodically.

### Laboratory DGA Method

The liquid samples and free-state fault gases were sampled in syringes and sent to the analytical laboratory for analysis. The analysis procedure strictly followed the IEC 60567. At first, the dissolved gases in the liquid samples were extracted by Toepler pump with multiple cycles. Then the type and amount of gases were determined by gas chromatography. The measurements are generally performed at least several times for minimizing the errors.

Compared online DGA method with laboratory DGA method, online method can be recognised as a relatively high accurate reference. Research results illustrate that agreement between the online gas measurements and the laboratory analysis is generally within a 30% deviation [16]. In this research, gas variation value will

be obtained according to the repeatability and accuracy of important laboratories. In the following section, precision values of current laboratories are discussed for determining the gas variation percentage.

### 3.3 Gas Variation

Table 3.1: Repeatability of IEC/CIGRE laboratories surveys [8]

	At medium gas concentrations	At low gas concentrations
Best Lab	$\pm 1\%$	$\pm 7\%$
Average	$\pm 7\%$	$\pm 27\%$
Worst Lab	$\pm 15\%$	$\pm 65\%$

Table 3.2: Accuracy of IEC/CIGRE laboratories [8]

	At medium gas concentrations	At low gas concentrations
Best Lab	$\pm 3\%$	$\pm 22\%$
Average	$\pm 15\%$	$\pm 30\%$
Worst Lab	$\pm 65\%$	$\pm 64\%$

Twenty-five experienced laboratories from 15 different countries, representative of current DGA practice in the worldwide, participated in the surveys of IEC and CIGRE, where the average repeatability and average accuracy are shown in Table 3.1 and Table 3.2 [8]. Medium concentration levels indicate the values are from 10 ppm to 100 ppm, while the low concentration levels are from 1 ppm to 10 ppm. Both excellent results and poor results were obtained with all the extraction techniques. The DGA gas data and their faults are provided in the following Table 3.4-Table 3.11 [4] [9]. Basically, the accurate laboratories operate in general with highly skilled personnel and follow strict procedures for calibration and quality. Most of the data are obtained from reports of CIGRE with high accuracy measurements.

According to Table 3.1 and Table 3.2, with less transportation and storage procedure, all the simulated gas records of CIGRE laboratory can be viewed as a high accuracy records. The repeatability is generally the measure of the amount scatter in the result obtained from multiple analyses of a sample, which is quite important for defining the accuracy. Also, many the gas records belong to range of medium concentration levels. Hence, a 5% gas variation is used in the study. It is higher than the medium value of the best lab but it is lower than the value of the average lab in Table 3.1. A small variation percentage can be used to estimate the Duval triangle boundary without many ambiguous classifications.

Some records are hard to obtained, for instance, high energy discharge will cause serious damage to the power transformer equipment. In such condition, a large variation to the original gas value can be caused in the collected gas records. Thereby, 10% variation is taken as a conservative estimate sampling error rate for these gas records by concerning the industrial process. It is higher than the medium value of the average lab but it is lower than the value of the worst lab in Table 3.1.

### 3.4 Duval Triangle Test

Table 3.3: DGA data cases under 5% variation

Case	CH <sub>4</sub>	C <sub>2</sub> H <sub>2</sub>	C <sub>2</sub> H <sub>4</sub>
1	+5%	-5%	+5%
2	+5%	+5%	-5%
3	-5%	-5%	+5%
4	-5%	+5%	-5%
5	+5%	-5%	-5%
6	-5%	+5%	+5%
7	-5%	-5%	-5%
8	+5%	+5%	+5%



The Duval Triangle applies three percentage values of gas :  $C_2H_2\% = 100x / (x+y+z)$ ;  $C_2H_4\% = 100y / (x+y+z)$ ;  $CH_4\% = 100z / (x+y+z)$ , with  $x = (C_2H_2)$ ;  $y = (C_2H_4)$ ;  $z = (CH_4)$ . In such case, each gas value has two variants. Each percentage will stay the same value for case 7 and case 8 in the Table 3.3. Therefore, six different percentage variations and the original combinations are applied in the test using Duval triangle method. Table 3.3 shows all possible combinations of three gas values with 5 % variations. The final classification result can be obtained by calculating correct number among the 7 cases. If the number is greater than 4, its final result can be recognised as a correct classified record, otherwise, it will be viewed as a misclassified case.

Figure 3.1 shows 12 gas samples of two lab simulated faults in Table 3.4, which contains 5 overheating faults in paper and 7 thermal faults in paper of oil. The red dots indicate the first fault cases while the green dots represent the second fault cases. All these dots are generally fitted in the faulty areas. The simulated temperature range are from 140°C to 800°C. Due to a reasonable assumption that the lab simulation results have high accuracy of measurement, 5% variations are added to these simulated data for re-examination.

Table 3.4: Simulated results of overheating faults [9]

Case	Paper	Paper/Oil	Temp.	H <sub>2</sub>	CH <sub>4</sub>	C <sub>2</sub> H <sub>2</sub>	C <sub>2</sub> H <sub>4</sub>	C <sub>2</sub> H <sub>6</sub>	CO	CO <sub>2</sub>	Units
1	X		800	22400	22400	1570	13440	2690	112000	56000	μl/g
2	X		500	670	224	2.00	67	45	112000	15680	μl/g
3	X		300	224	4.5	0.00	0	2	2	560	μl/g
4	X		150	900	9180	22.0	900	0	1344	8950	μl/g
5	X		100	0	224	0	45	0	0	670	μl/g
6		X	300	470	4637	0	448	1300	25312	51000	μl/l
7		X	300	65	20	0	5.0	10			%
8		X	300	53	39	0	4.5	3			%
9		X	225	219	44	0	3.0	3	3000	13000	ppm
10		X	200	37	447	0	5.5	10			%
11		X	150	34	30	0	2.5	34			%
12		X	140	14	62	0	3.0	16	68	7500	ppm

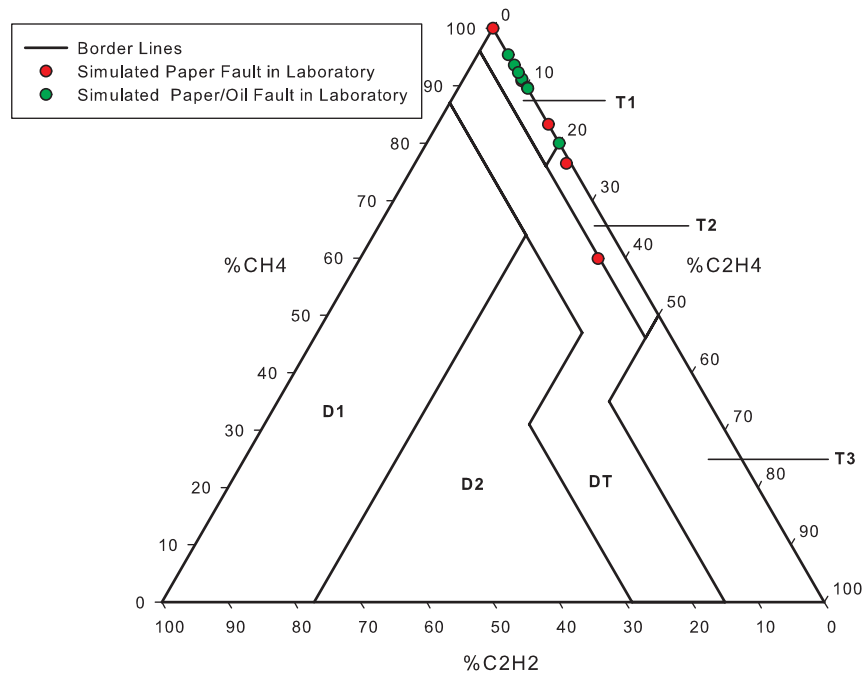


Figure 3.1: Laboratory DGA data in Duval triangle

Figure 3.2 and Figure 3.3 show all the results of each gas sample with 5% variation in the Duval Triangle graphic using different colors. Original data are represented by the cross while six different variation values are around their original data. Five overheating faults are considered at first. As it can be seen from Figure 3.2, green dots, which represent a 800°C fault in paper, tend to be classified in the DT zone. The original fault should be classified into T3 zone, but it turns out at the edge of T2 zone. Variants of other 4 fault case are in the same areas without any difficulty for the final classification. In the figure, all the corrected classified cases are in the right zone under the consideration of 5% variation except a misclassification sample. Variants of these simulated cases tightly stick together, and distributed along at the direction of  $C_2H_2$  borderlines.

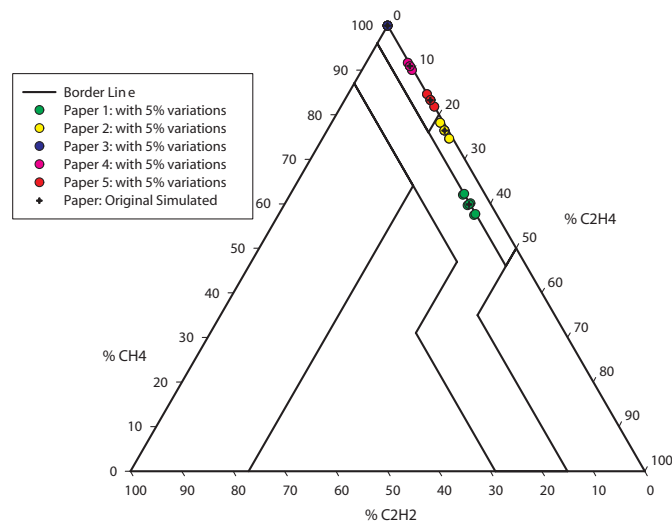


Figure 3.2: Laboratory simulated faults in paper with 5% variation

Figure 3.3 illustrates 7 cases of overheating paper in oil faults. The yellow square result, which indicates a 300°C fault in paper of oil, shows an equal opportunity to be classified into T1 and T2 zone. All the rest sample's variants, which were correctly classified zone, stay in the same area T1 with a close appearance. For the second case, whose original value is located at the threshold line between T1 zone and T2 zone, illustrates an equal opportunity of the variants' appearance in T1 and T2, which can cause problem in final classification result. Therefore, it is strongly suggest that once a fault case is located in the threshold line, the sample needs to be carefully considered for providing a reliable final classification result.

Table 3.5: Hot spots in oil simulated in the laboratory [9]

Case	Temp.	H <sub>2</sub>	CH <sub>4</sub>	C <sub>2</sub> H <sub>2</sub>	C <sub>2</sub> H <sub>4</sub>	C <sub>2</sub> H <sub>6</sub>	CO	CO <sub>2</sub>	Units
1	800	65	34	0	112	16			μl/g
2	500	0.7	1.5	0	1.8	0.3			μl/g
3	300	0	0.2	0	0.13	0.1			μl/g
4	235	48	40	0	0.50	11			%
5	225	130	140	0	120	24	2	400	ppm
6	175	86	8	0	2.50	2.5			%
7	168	6	3	0	0.70	0.8			ml
8	160	50	3	0	0.00	1	14	581	ppm
9	140	55	22	0	2.60	0.5	358	961	ppm
10	120	78	66	0	2.60	62	283	1772	ppm

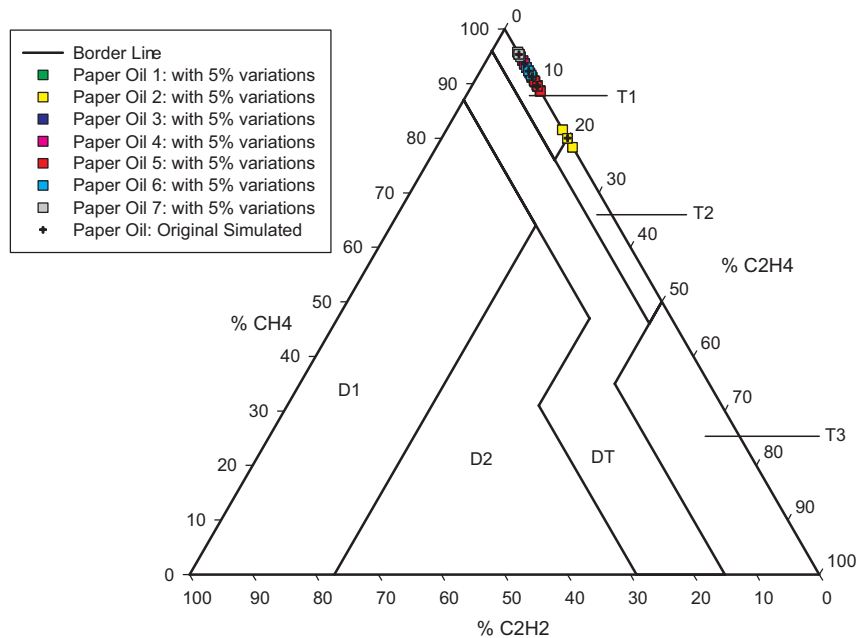


Figure 3.3: Simulated paper in oil fault with 5% variation

Figure 3.4 shows 10 fault cases of hot spot in oil in Table 3.5. Only the 7th case's variants, which indicate a fault that 168°C hot spot in oil, tend to be classified into T2 zone. All other faults keep the same classification results. As it can be seen from above three figures. All the variation dots appear tightly around the original simulated gas values. Also, these variations will not affect the final judgements by using the Duval Triangle except some specific values, such as case at the edge

of two adjacent zones or misclassification ones. Therefore, it is very important to re-examine the gas records when the gas results are located on the threshold lines.

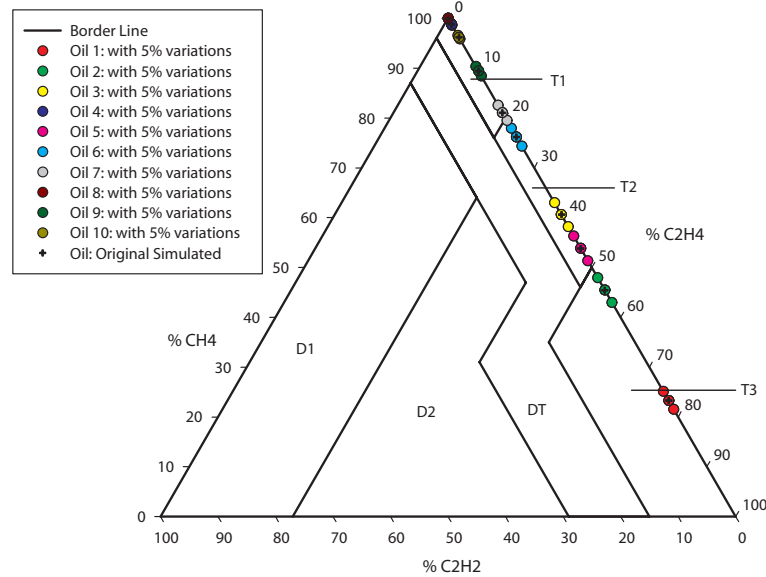


Figure 3.4: Simulated oil fault with 5% variation

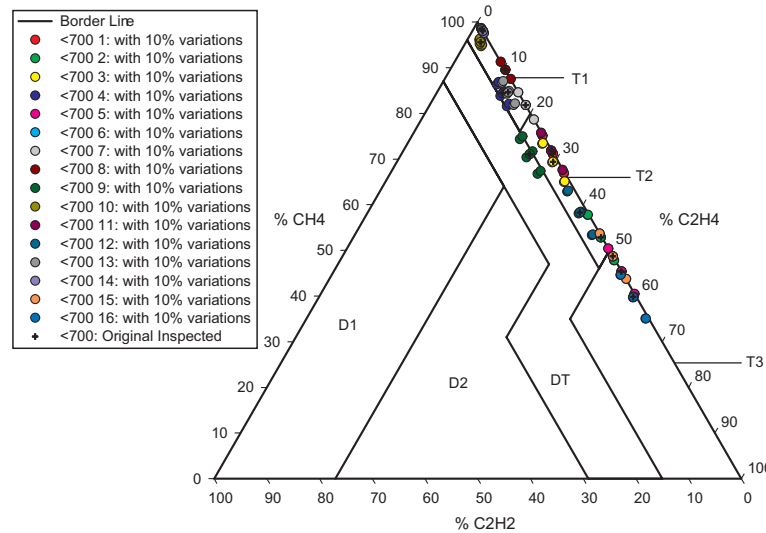


Figure 3.5: Inspected fault cases below 700 degree with 10% variation

Figure 3.5 illustrated 16 fault cases of power transformer in Table 3.6, which are obtained by visual inspections. In such cases, all the gas values are added by 10%

Table 3.6: Fault identified as thermal faults &lt; 700 (T1 and T2) by inspection of the equipment [9]

Case	Inspection	H <sub>2</sub>	CH <sub>4</sub>	C <sub>2</sub> H <sub>2</sub>	C <sub>2</sub> H <sub>4</sub>	C <sub>2</sub> H <sub>6</sub>	CO	CO <sub>2</sub>
1	High circulating currents between conductors with winding damage	1270	3450	8	1390	520		
2	Circulating currents in LV windings and core	3420	7870	33	6990	1500		
3	Thermal runaway inside thick insulation with puncture	360	610	9	260	259		
4	Thermal runaway in thick paper insulation	1	27	1	4	49		
5	Blackened area within windings, interturn fault, open circuit parallel path	3675	6392	5	7691	2500	2	400
6	Vertical bar buses burnt out, carbonization of paper strips	48	610	0	10	29		
7	Carbonized windings during heat run tests	12	18	0	4	4		
8	Circulating currents in magnetic tank shunt during heat run tests	66	60	0	7	2	14	581
9	Overheating of core to ground and insulation shields	1450	940	61	322	211	2420	356
10	Hot spot with carbon formation	0	18900	330	540	410	3900	710
11	Hot spot in paper	960	4000	6	1560	1290	15800	50300
12	Hot spot in paper	24700	61000	1560	42100	26300	14400	30400
13	Overheating of conductor < 200	14	44	1	7	124	128	2746
14	Low temperature overheating of clamping beams of yokes by stray flux	2031	149	0	3	20	556	3008
15	Idem, with carbonization of beams	480	1075	0	1132	298	464	1000
16	Thermodielectric failure	40000	400	6	600	70	800	218

variations, and then these cases are classified by Duval Triangle method. It is clear to be seen that all the variation dots are dispersed located around the original values. Some of them have different classification results, such as, the 5th case, the 7th case, the 9th case and the 15th case. For the 9th case, the original gas obtained from a power transformer with a fault of overheating insulation shields, which can generate circulating currents in paper insulation resulting from high dielectric losses. It is reasonable that some variants of the 9th cases locate at DT zone. But, among all the variants of the 9th case, three variants and the original value itself are very near to T2 zone. The 15th case is obtained from a fault of carbonization beams, which is strongly suggested as a thermal fault over 700°C by IEC 60599. It is also proved by the facts that two out of three variation values appear in the T3 zone. The 2nd case indicates a fault of circulating currents in low voltage windings and core and two values out of three appear in the T2 zone. Based on the above analysis, a corresponding zone is given in the following figure for improve the reliability of Duval method. Addition cautions should be considered when the gas samples is in the zone. The zone is defined by the red dash lines, where the  $\%C_2H_4=60$  and  $\%CH_4=4$ .

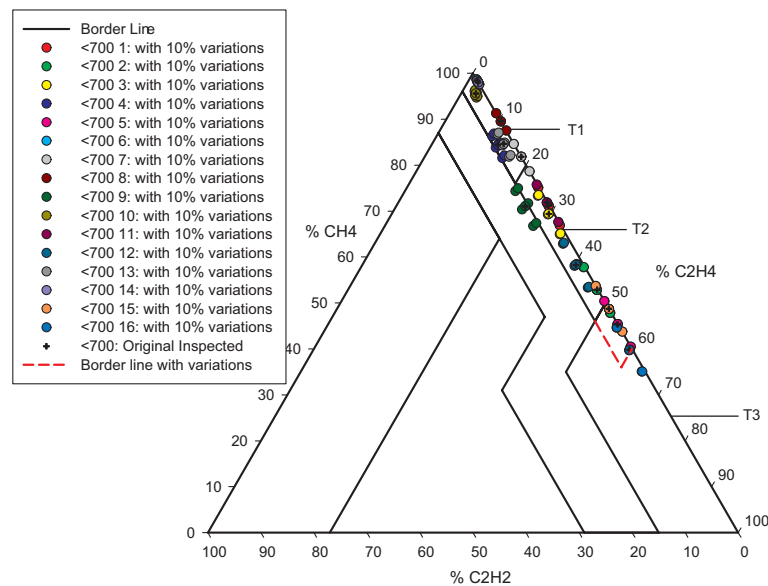


Figure 3.6: Inspected fault cases below 700 degree with threshold variation

Table 3.7: Fault identified as thermal faults &gt; 700 (T3) by inspection of the equipment [9]

Case	Inspection	H <sub>2</sub>	CH <sub>4</sub>	C <sub>2</sub> H <sub>2</sub>	C <sub>2</sub> H <sub>4</sub>	C <sub>2</sub> H <sub>6</sub>	CO	CO <sub>2</sub>
1	Hot spot at connection	8800	64064	0	95650	72128	290	90300
2	Circulating currents between yoke clamps and connecting bolts	6709	10500	750	17700	1400	290	1500
3	Pyrolitic carbon growth between selector contacts	1100	1600	26	2010	221	0	1430
4	Steel lamination eroded	290	966	57	1810	299	72	756
5	Circulating currents in clamping bolt	2500	10500	6	13500	4790	530	2310
6	Contacts of selector switch burnt	1860	4980	1600	10700	0	158	1300
7	Lengthy overheating of tap changer contacts	860	1670	40	2050	30	10	690
8	Defects on contacts of tap changer selector	150	22	11	60	9	0	0
9	High contact resistance of winding terminal	400	940	24	820	210	390	1700
10	Ground wiring burnt and ruptured by circulating current	6	2990	67	26076	29990	6	26
11	Burnt copper contacts in change over selector	100	2990	67	26076	29990	6	26
12	Bad contact in windings	290	1260	8	820	231	228	826
13	Bad contact in defective weld in windings	1550	2740	184	5450	816	1140	9360
14	Hot spots in laminations	3910	4290	1230	6040	626	1800	11500
15	Hot spot in laminations (molten steel)	12705	23498	5188	34257	6047	4004	853
16	Hot spot on bushing	1	8	6	100	8	300	5130
17	High temperature in laminations	300	700	36	1700	280	760	925
18	Burnt lamination during heat run test	107	143	2	222	34	193	1330



The following Figure 3.7 shows 18 fault cases of thermal faults over 700°C in the Table 3.7. The 14th case and the 15th case have variants out of T3 zone. Four variations of 2nd case, which are represented by green dots, are located in T2 and only two variations are classified into T3 in DT zone. According to IEC 60599, the 2nd case, which obtained from a power transformer with a fault of circulating currents between yoke clamps and connecting bolts, strongly suggested to be classified into thermal fault between 300°C and 700°C. It also proved by the facts that most of its variants are located in T2 zone. As it can be seen from the figure, when the fault cases appear in the area near to the edge of DT, such as the 14th case and the 15th case, their variants are highly sparse distributed. Compared with these cases, the fault cases, which contains a small  $C_2H_2$  value, tend to be tightness distributed.

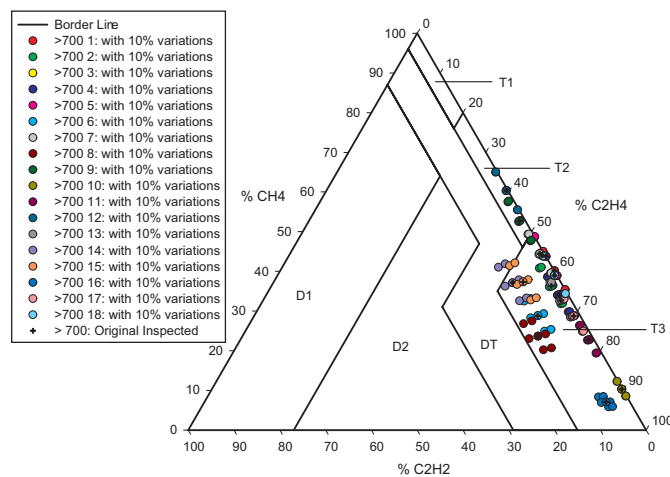


Figure 3.7: Inspected fault cases above 700 degree with variation of 10 percent

A corresponding zone is presented in the following figure for improving the reliability of detection of high thermal faults. A zone is highlighted when these variation values are considered. The zones indicates by the red dash lines are:  $\%C_2H_4=40$  and  $\%CH_4=4$ . The 6th case, which represent a fault of contacts of selector switch burnt, appears at the edge of the give zone. All the variants of the 2nd case are included by the zone.

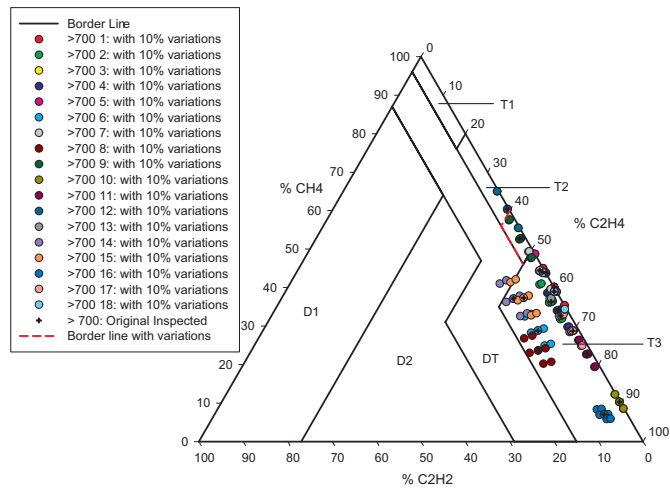


Figure 3.8: Inspected fault cases above 700 degree with threshold variation

Based on the analysis of above two inspected fault cases, a zone, which is defined by the red dash lines, indicates that the gas records have high possibilities of misclassification. In other words, gas records, whose  $\%C_2H_4$  values are from 40% to 60% and their values of  $\%C_2H_2$  are smaller than 4%, can represent a fault either above 700 °C or below 700 °C. Therefore, fault detection of gas records in this area need to be considered carefully.

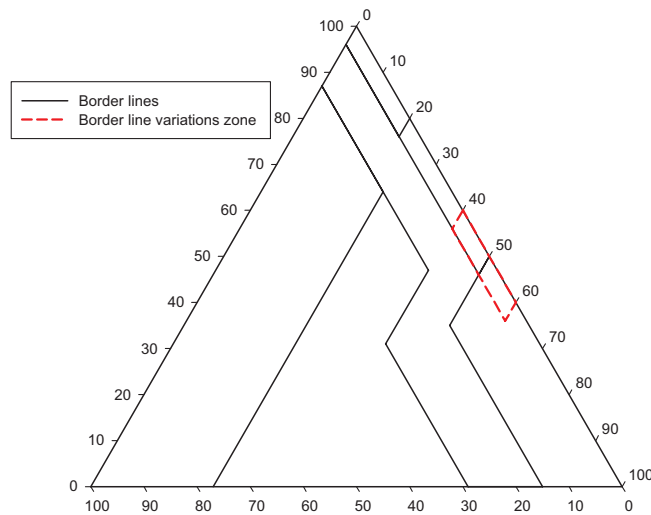


Figure 3.9: Thermal fault with threshold variation

Table 3.8: Electrical low energy discharge simulated in the laboratory [9]

Case	Description	H <sub>2</sub>	CH <sub>4</sub>	C <sub>2</sub> H <sub>2</sub>	C <sub>2</sub> H <sub>4</sub>	C <sub>2</sub> H <sub>6</sub>	CO	CO <sub>2</sub>
1	30 pC in moist paper	2240	157	45	45	90	45	67
2	Pds in badly impregnated paper	73	8	12	2	4	0	0
3	Needle-to-plane Pds > 100 pC	5000	4000	8000	2000	2000	0	0
4	Needle-to-plane Pds > 1000 pC	24.3	15.7	29.8	11.2	6.4	0	0
5	5,000 pC in paper/oil wedge	2240	360	828	169	25	45	2240
6	10,000 pC in oil	4480	560	896	403	380	67	403
7	500,000 pC in paper/oil wedge	200	230	480	170	2	6	160
8	Arcing in oil	60	5	29	6	1	0	0
9	Point-to-plane discharge in oil	890	110	700	84	3	0	430
10	Needle-to-sphere discharge in oil	41	112	4536	254	0	0	98
11	Rod-to-rod discharge	16000	4000	16000	8500	500	0	0
12	Needle-to-plane lightning impulse	210	22	7	6	6	19	74

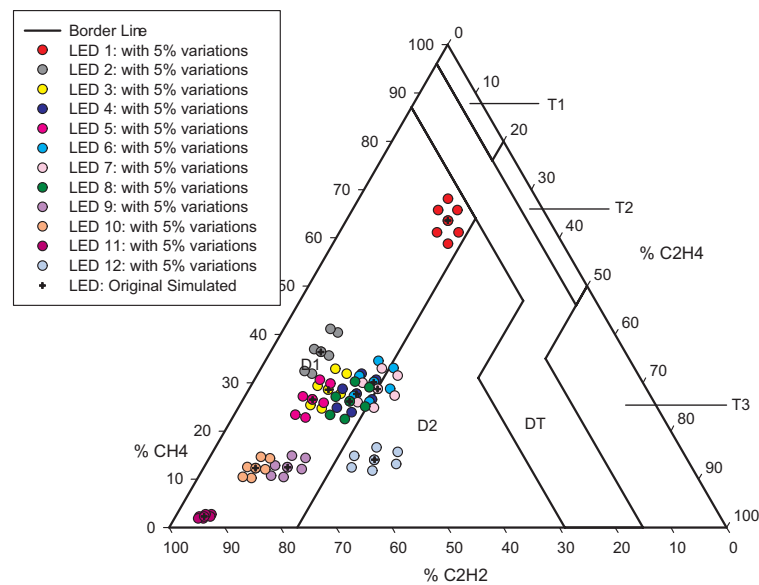


Figure 3.10: Electrical low energy discharge simulated in the laboratory with 5 percent variation

Figure 3.10 illustrates 12 cases in Table 3.8, which represent the simulation results of the laboratory. As it can be seen from the figure, the 4th case, the 5th case, the 6th case and the 7th case, which indicate discharge faults of needle-to-plane > 1000 pC, 5000 pC in oil wedge, 10000 pC in oil and 500000 pC in oil wedge, have values of variation in high energy discharge zone. Those apparent charge

values are from the lab for faults of continuous sparking and discharge of low energy. The real charge and the apparent charge are related through a proportionality factor that normally is well below 1, which implies that the real charge energy can be severely underestimated, and depends in part on the geometry of the defect, furthermore, attenuation phenomena can reduce apparent charge readings by factors that are related to apparatus geometry, materials and the location of the discharge site [43] [44]. These three cases can be recognised as very high discharge level. This is probably one of the reasons why their variation values are classified into high energy discharge area. The 7th case has a really high apparent charge value of 500000 pC. The 4th case, the 6th case and the 7th case have a really large values of apparent charge. Below a threshold near 100 pC the discharges were almost harmless to the insulation in wedge type discharges and it was found that millions of pulses up to 100 pC did no damage at all, while just a few large pulses in the range 500-1000 pC easily punctured the pressboard cover, leading to breakdown within approximately 30 seconds [45]. The 1st case and the 3rd case, which indicate 30Pc in moist paper and needle-to-plane Pds > 100Pc, are belong to the condition. They are located at center of D1 zone.

Table 3.9: Fault identified as discharges of low energy ( D1 ) by inspection of the equipment [9]

Case	Inspection	H <sub>2</sub>	CH <sub>4</sub>	C <sub>2</sub> H <sub>2</sub>	C <sub>2</sub> H <sub>4</sub>	C <sub>2</sub> H <sub>6</sub>	CO	CO <sub>2</sub>
1	Loosening of potential ring on bushing, with marks of sparking and tracking	78	20	28	13	11		784
2	Sparking between HV braided connection and isolated copper tube	305	100	541	161	33	440	3700
3	Selector breaking current in selector tank	35	6	482	26	3	200	2240
4	Continuous sparking between metal cups and earthed bolts in winding	543	120	1880	411	41	76	2800
5	Tracking to HV bushing	1230	163	692	233	27	130	115
6	Tracking in bushing	645	86	317	110	13	74	114
7	Tracking to the ground in glue of central beam	60	10	4	4	4	780	7600
8	Sparking on tank walls to the bushing	95	10	39	11	0	122	467
9	500 OLTC normal operations	6870	1028	5500	900	79	29	388
10	3600 OLTC normal operations	100925	53993	37565	6500	530	42	413
11	Poor shielding contact	650	81	270	51	170	380	2000
12	Traces of discharges in paper of cone junction of HV cable	210	22	7	6	6	19	74
13	Sparking from bushing to tank	385	60	159	53	8	465	1250
14	Sparking from bushing to tank	4230	690	1180	196	5	438	791
15	Tracking in paper	7600	1230	1560	836	318	4970	4080
16	Low energy arcing on bushing	595	80	244	89	9	524	2100
17	Low energy in core	120	25	40	8	1	500	1600
18	Contamination from OLTC	8	0	101	43	0	192	4067
19	Tracking in insulation	6545	2313	6432	2159	121	3628	255
20	Tracking from windings to beam	1790	580	619	336	321	956	4250
21	Sparking / Tracking in insulation	1330	10	182	66	20	231	1820
22	Sparking from core to ground	4	1	52	7	2	93	519
23	Contamination from OLTC	1900	285	7730	957	31	681	732
24	Defective OLTC operation	57	24	30	27	2	540	2518
25	Low energy arcing in bushing	57	24	30	27	2	540	2518
26	Low energy discharge in oil, signs of tracking along inner porcelain	1000	500	500	400	1	200	1000

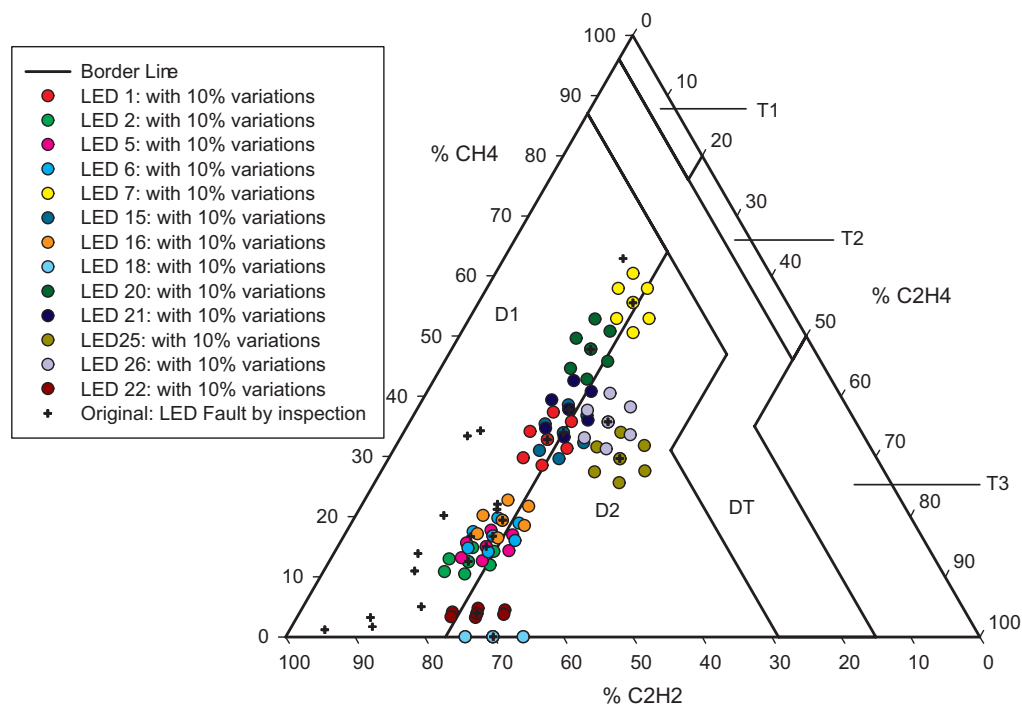


Figure 3.11: Fault identified as discharges of low energy by inspection of the equipment with 10 percent variation

The Figure 3.11 shows the 26 cases of low energy discharge faults by inspection with 10 percent variation in Table 3.9. For those cases are classified into zones, which are not belong to D1 zone, 6 different color around dots are used. The original cases are displayed with crossing. Most of the tracking faults, the 2nd case, the 5th case, the 6th case, the 7th case, the 15th case, the 16th case, the 20th case and the 21th case, are very near to the edge of D2. The bushing related fault is one of the leading causes of catastrophic failures in power transformers. Those tracking are generated by active corona. Once corona becomes active it leaves behind a conductive tracking path on surfaces and also creates a very conductive cloud of air around itself. A flashover can occur once a tracking pathway is completed from phase to phase or phase to ground. Therefore, those faults energy are quite high. Three bushing related faults, the 5th case, the 6th case and the 16th case, which indicate tracking to HV bushing, tracking in bushing, low energy arcing on bushing, all the related variations are classified into D2 zone. Four fault cases, the 18th case, the 22th case, the 25th case and the 26th case, are classified into D2 areas. The 22th case, 25th case and

the 26th case represent fault of sparking from core to ground, low energy arcing in bushing and low energy discharge in oil, signs of tracking along inner porcelain. For the last two cases, they are classified into the D2 areas with variation values equally distributed around them.

According to the above analysis, a possible threshold is also provided in the following figure, where the start point of the dash line is  $\%C_2H_4=27.77$ ,  $\%CH_4=59$ ,  $\%C_2H_2=13.23$ , and the end point is  $\%C_2H_4=27.77$ ,  $\%CH_4=0$ ,  $\%C_2H_2=67$ . Only three cases, the 18th case, the 25th case, and the 26th case, are not in the zone. These three cases are indicate the fault of contamination from OLTC, low energy arcing in bushing and energy discharge in oil with signs of tracking along inner porcelain. Among all the faulty cases of sparking, only the 22nd case, which indicates the sparking from core to ground, locates in the D2 zone. The 8th case, the 13th case, the 14th case and the 19th case are all located in D1 zone. The 21st case and the 22nd case, which indicate sparking in insulation and sparking from core to ground, are in the D2 zone. Most of sparking faulty cases are rightly classified in the D1 zone. The 25th case and the 26th case are arcing related faults, which are low energy arcing and low energy discharge in oil with tracking in the porcelain.

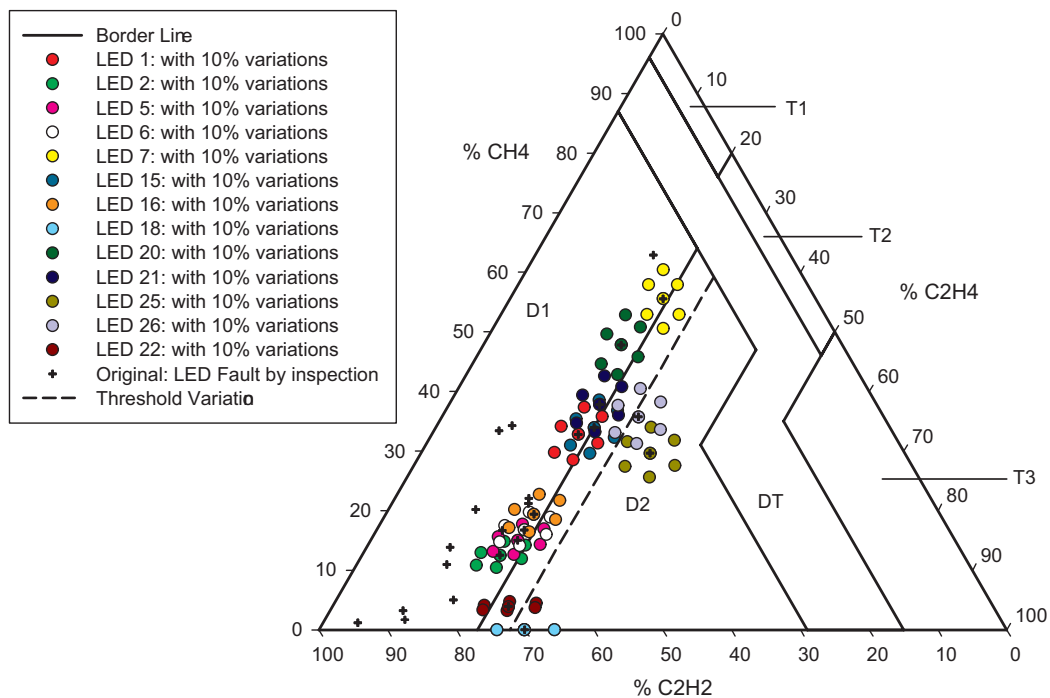


Figure 3.12: Fault identified as discharges of low energy by inspection of the equipment with threshold variation

Figure 3.13 shows 48 inspected cases of high energy discharge fault in Table 3.10 and Table 3.11. All the cross points indicate the original value of faulty gas data. All the gas records with variations of crossing borderlines are represented by six color points. As it can be seen from the figure, 13 cases with their variants are located in areas, where do not belong to D2 zone. The fault typically involves a short circuit from one, or more, of the bus bar connections to a ground or between phases of the power source through the surrounding medium, such as air or an insulating fluid. Normally, the surrounding medium becomes ionized and an electric discharge travels along the path of least resistance. Transformers may be affected by arcs that propagate through the fluid. The formation of air bubbles that get larger with time as more arcs occur in oil-filled transformer. Finally, catastrophic failure takes place, typically from over-pressurization causing a rupture of the transformer casing, and the fluid being discharged [46]. The transformer fluid may ignite as either a pool or spray fire. This issue has been explored to a much larger extent than other types of high energy discharge events, and the resulting fire is conceptually easier to quantify



Table 3.10: Fault identified as discharges of high energy ( D2 ) by inspection of the equipment [9]

Case	Inspection	H <sub>2</sub>	CH <sub>4</sub>	C <sub>2</sub> H <sub>2</sub>	C <sub>2</sub> H <sub>4</sub>	C <sub>2</sub> H <sub>6</sub>	CO	CO <sub>2</sub>
1	Flahover from LV to ground	440	89	757	304	19	229	1190
2	Arc in selector switch	210	43	187	102	12	167	1070
3	Short circuit in distribution windings	2850	1115	3675	1987	138	2330	4330
4	Short circuit from LV to ground	7020	1850	4410	2960	0	2140	1000
5	Short circuit from LV to connector	545	130	239	153	16	660	2260
6	Arcing from windings to porcelain	7150	1440	1760	1210	97	608	2260
7	Tertiary windings damaged by arcing	620	325	244	181	38	1480	2530
8	Arcing in wet cellulose	120	31	94	66	0	48	271
9	Short circuit in windings	755	229	460	404	32	845	5580
10	Arcing from windings to ground	5100	1430	1010	1140	0	117	197
11	Short circuit in windings	13500	6110	4040	4510	212	8690	1460
12	Bushing swollen, tank opened	1570	1110	1830	1780	175	135	602
13	Arcing to magnetic circuit (ground)	3090	5020	2540	3800	323	270	400
14	Short circuit between conductors	1820	405	634	365	35	1010	8610
15	Arcing inside windings	535	160	680	305	16	172	338
16	Flash-over between dislocated connection and HV bushing turre	13	3	6	3	1	4	51
17	Flash-over with burnt insulation	137	67	104	53	7	196	1678
18	Arcing on selector switch ring	1084	188	769	166	8	38	199
19	Arcing between connections to tap changer, burnt areas on windings	34	21	56	49	4	95	315
20	Arcing in static shield connections	7940	2000	5390	3120	355	1130	285
21	Very short HV high energy discharge, followed by tracking	150	130	30	55	9	120	200
22	Arcing from bushing to tank	8200	3790	5830	4620	250	31	85
23	Arcing in windings	260	215	277	334	35	130	416
24	Arcing in windings	75	15	26	14	7	105	322
25	Arcing in windings	530	345	250	266	85	3900	20000
26	Arcing in oil	60	5	21	21	2	188	2510
27	Arcing in windings	90	28	32	31	8	1380	11700
28	Arcing in windings	220	77	240	170	22	1800	13800
29	Arcing in windings	5900	1500	2300	1200	68	750	335

Table 3.11: Fault identified as discharges of high energy ( D2 ) by inspection of the equipment [9]

Case	Inspection	H <sub>2</sub>	CH <sub>4</sub>	C <sub>2</sub> H <sub>2</sub>	C <sub>2</sub> H <sub>4</sub>	C <sub>2</sub> H <sub>6</sub>	CO	CO <sub>2</sub>
30	Arcing in windings	420	250	800	530	41	300	751
31	Arcing from bushing to tank	2800	2800	3600	3500	234	92	718
32	Arcing in bushing	99	170	190	200	20	140	1160
33	Arcing in oil duct	310	230	760	610	54	150	631
34	Arcing in oil duct	800	160	600	260	23	490	690
35	Arcing from bushing to tank	1500	395	323	395	28	365	576
36	Arcing from windings to core	20000	13000	57000	29000	1850	2600	2430
37	Arcing in windings (molten metal)	305	85	130	197	25	813	8380
38	Arcing in windings	1900	530	434	383	35	1890	7570
39	Arcing in windings	110	62	250	140	90	680	6470
40	Arcing in oil (turret)	3700	1690	3270	2810	128	22	86
41	Arcing in oil (turret)	2270	660	763	712	54	522	1490
42	Arcing from bushing to tank	245	120	167	131	18	829	4250
43	Arcing from HV to tank	1170	255	325	312	18	5	1800
44	Arcing from bushing to tank	4419	3564	2025	2861	668	909	9082
45	Arcing in bushing	810	580	490	570	111	1100	6800
46	Arcing in bushing insulation	5000	1200	1100	1000	83	140	265
47	Arcing in OLTC and windings	10000	6730	10400	7330	345	1980	3830
48	Arcing in oil from copper bus to tank	1570	735	1740	1330	87	711	4240

because the knowledge base on oil pool and spray fires is relatively robust [47]. Among the fault cases, the variation values of the 21st case are classified into D1 and DT zone. It represents a fault of very short high energy discharge, followed by tracking. The fault only generates a tracking without burns. Two variants are located in DT zone while one is classified into D1. It has a similar pattern with above the 7th case. Only one variant of the 18th case is in the D1 zone. The 18th case represents arcing on selector switch ring of a load tap changer.

A variation thresholds are provided in the following figure, where the start point of the dash line is  $\%C_2H_4=19.73$ ,  $\%CH_4=68.66$ ,  $\%C_2H_2=13.23$ , and the end point is  $\%C_2H_4=19.73$ ,  $\%CH_4=0$ ,  $\%C_2H_2=80.17$ . Based on the above analysis, a suspected area is given in the following Figure 3.15. Typical inspected faults in this areas, are bushing related low energy discharge faults, tracking related low energy discharge faults as well as bushing arcing. Variation threshold will not be provided for the DT zone due to the facts high energy discharge always generates large heat. Some of faults will cause flash-over and burn insulation. Those dots, which are classified into D2 zone with clear variations, always have very serious damage to the power transformer such as, molten metal, flash-over of whole insulation material.

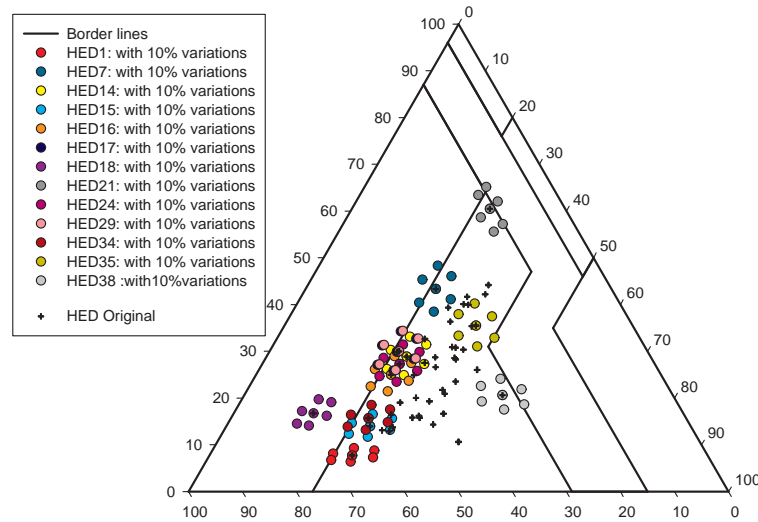


Figure 3.13: Fault identified as discharges of high energy by inspection of the equipment with 10 percent variation

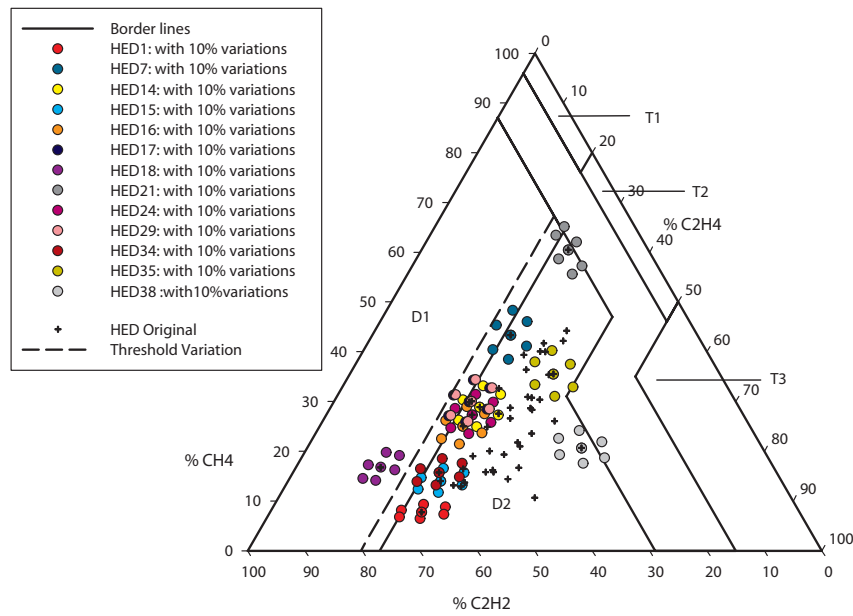


Figure 3.14: Fault identified as discharges of high energy by inspection of the equipment with threshold variation

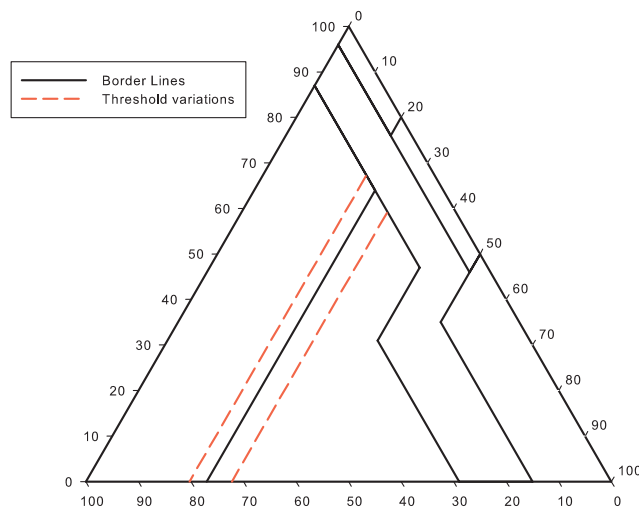


Figure 3.15: Discharges of energy equipment with threshold variation

Figure 3.16 shows 5 cases of PDs simulated in the laboratory. Almost all the variations are basically around the original values. Only the 5th case, which represents a fault of 30 pC in moist paper, is classified into the areas of the partial

discharge zone. A variations lines is shown in the Figure 3.17. It includes all the values and the variations in the PD zone. The new zone is defined as  $\%CH_4 \geq 96$ , while the original value of  $CH_4$  is 96%.

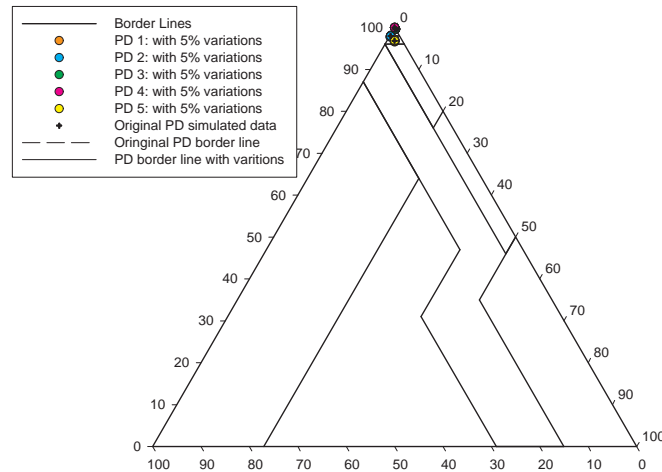


Figure 3.16: Partial discharge simulated in the laboratory with 5 percent variation

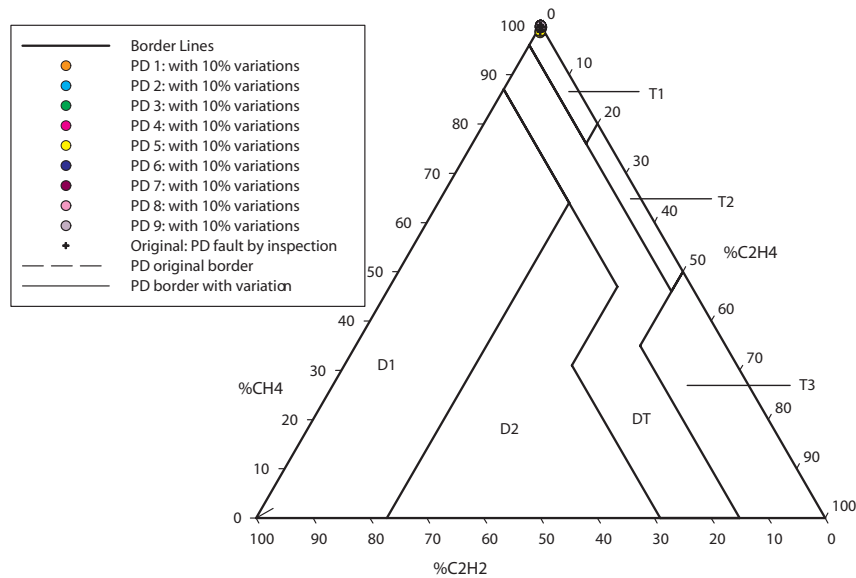


Figure 3.17: Partial discharge fault by inspection of the equipment with 10 percent variation

Based on the Figure 3.9, Figure 3.15, and Figure 3.17, several important zones are

summarised by the following Figure 3.18. In these zones, a high possibility of misclassification can be existed especially with a low precision of DGA gas data. All these areas are obtained from the IEC10 cases. Z1 indicates a zone of energy discharge, whose  $\%C_2H_4$  value is from 19% to 30%. Most the inspected values that represent low energy discharge in the area are faults of busing related arcing and faults of all tracking. Most of these two fault cases have variation values in the zone, where the  $\%C_2H_4$  is between 23% and 30%. For the inspected cases of high energy discharge fault, such as arcing in LV windings and flash-over fault, have variations in the zone between 19% and 23%. The Z2 indicates a suspected zone between T2 and T3. Among all overheating cases, whose thermal values are greater than 700 °C, faults of bolt have tenancy to be classified into T2 zone, and the value of  $\%C_2H_4$  can reach to 40%. The fault cases, which are lower than 700 °C, achieve the value 60%, such as carbonization of beams, therm-dielectric failure and carbonization of paper strips. As some cases of the partial discharge fault are located in the areas out of the original zone. One case with its variations are located in the PD zone between 96% and 98%. The variation value can be classified into this area. Under the same energy of partial discharge, different gases can be generated, for example, 30 pC in moist paper will have a lower  $CH_4$  percentage compared with dry ones.

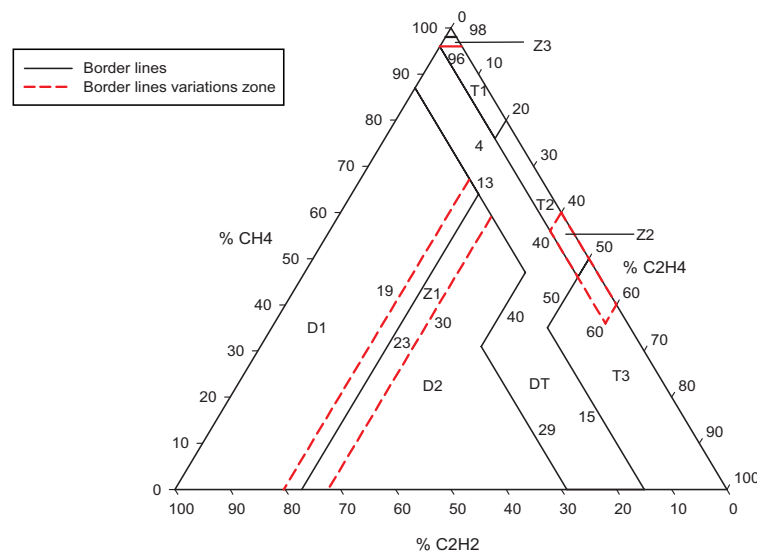


Figure 3.18: Duval triangle with variation threshold

Table 3.12: Classification result of each fault

Fault	Number of cases	Correct cases	Correct percentage
Thermal < 700 °C	16	13	81.25%
Thermal > 700 °C	18	16	81.88%
Partial discharge	14	13	92.85%
Low energy discharge	38	32	84.21%
High energy discharge	48	47	97.91%

By calculating the number of misclassified cases in each classification, Table 3.12 is obtained and it can be seen that if the original data is correctly classified, its 5% or 10% variants normally can be correctly classified. Some of the gas records caused by typical faults need to be considered very carefully due to the fact that they are in the area close to the threshold of a zone.

### 3.5 IEC Ratio Test

The method original from the IEC ratio method, except that the ration  $C_2H_6/CH_4$  was dropped since it only indicated a limited temperature range of decomposition as shown in the Table 2.7. All the tests are carried out by considering their variation values same as they are in Duval triangle test.

First of all,  $\pm 5\%$  variation is calculated and these values are added to the simulated lab values and  $\pm 10\%$  variation is computed with the inspected values. The IEC Ratio method applies the following three ratios:  $\frac{C_2H_2}{C_2H_4}$ ,  $\frac{CH_4}{H_2}$  and  $\frac{C_2H_4}{C_2H_6}$ , we have calculated all the combinations of these three ratios for each gas record, for example, these three ratio values can be calculated when  $C_2H_2$  increases 10% and the other gases decrease 10% for a given gas data record. All the possible combinations of three gas ratios  $P$  is equal to  $[(C_2^1 C_2^1 - 1)(C_2^1 C_2^1 - 1) - 2][C_2^1 C_2^1 - 1]$ , where  $C_2^1 = \frac{2!}{1!(2-1)!}$  and  $P = 21$ . There are 21 combinations of the three gas ratios when the variations of each gas are applied.

The procedure is first to calculate the 21 variants of a given gas record and then

the all these variants and itself will be classified by using IEC ratio test. The final result is obtained by counting the number of each result. For example, if there are 11 codes of '1 0 2' for a testing case, which is greater than the numbers of other codes, then the final fault will be discharge of low energy according to Table 2.7. However, unknown cases can appear in the combinations of a given gas records. For instance, the gas record will be recognise as an unknown case when there are 11 codes of '1 2 1', which does not exist in the Table 2.7.

Table 3.13: Classification result of each type of fault

Fault	Number of cases	Correct cases	Unknown cases	Percentage
Thermal $< 700\text{ }^{\circ}\text{C}$	16	7	5	43.75%
Thermal $> 700\text{ }^{\circ}\text{C}$	18	11	3	61.11%
Partial discharge	14	3	4	21.43%
Low energy discharge	38	16	7	42.11%
High energy discharge	48	41	3	85.42%

The final classification results are shown in the Table 3.13. It can be seen that many gad records are classified as a unknown condition due to the lack of codes of Table 3.13. Compared with results of from Duval Triangle, the classification accuracy of each condition is lower under the same variations. One reason is that codes are not enough for representing the original faults while the other one is that variations of those values that locate in the threshold edge can be generate many unknown combination codes. It can lead to a misclassification of final result. For those cases in thermal fault  $< 700\text{ }^{\circ}\text{C}$ , typical combinations, such as '1 2 0', '0 1 2', '1 2 1' and '0 0 2' are classified into unknown cases. Cases with these code are the 4th case, the 8th case, the 10 case, the 13th case and the 16th case by Duval Triangle method, which represent the fault of thermal runaway in thick paper insulation, circulating currents in magnetic tank shunt during heat run tests, hot spot with carbon formation, overheating of conductor and thermal dielectric failure. Compared with IEC ratio method, the first three cases are correctly classified except the 16th case. It located in the zone of temperature  $> 700\text{ }^{\circ}\text{C}$ . However, the 5th case and the 16th case, which



indicate fault of blackened area within windings, interturn fault, open circuit parallel path and thermal dielectric failure, are misclassified into the zone of temperature  $> 700\text{ }^{\circ}\text{C}$  by both methods.

For cases in thermal fault  $> 700\text{ }^{\circ}\text{C}$ , three cases, the 6th case, the 14th case and the 15th case, are classified as unknown faults. All their codes are '1 2 2', while the code for the fault is '0 2 2' of IEC Ratio method. These three cases represent fault of contacts of selector switch burnt, hot spots in laminations and hot spot in laminations with molten steel. These three cases are correctly classified by using Duval methods, but the variations of last two values are located in the DT zone.

Four cases have unknown codes in partial discharge fault. These four unknown codes are corona in ASTM D2300, corona in gas bubbles, X-wax deposits and partial discharges, which are represented by codes of '2 0 0', '0 0 2', '1 0 0' and '1 0 0'. The original codes of partial discharge is '\* 1 0', where '\*' indicates that it can be any code. All these unknown cases are correctly classified by using Duval Triangle method.

For the 12 simulated cases of low energy discharge, four cases are unknown by using the IEC ratio method. The 2nd case, the 8th case, the 9th and the 11th case indicate the simulated fault of Pds in badly impregnated paper, arcing in oil, point-to-plane discharge in oil and rod-to-rod discharge. All these fault are classified right except the 2nd case, which is located in high energy discharge zone.

In the 26 fault identified as discharges of low energy by inspection of the equipment, three cases, the 8th case, the 15th case and the 19th case, are unknown. They are obtained from faults of sparking on tank walls to the bushing, tracking in paper and tracking in insulation. Their codes are '2 0 0', '1 1 2' and '1 1 2'. The original codes are '1-2 0 1-2'.

For the 48 fault cases identified as discharge of high energy by inspection of the equipment, six cases, the 2nd case, the 3rd case, the 6th case and the 7th case, the 12th case and the 13th case, are classified as unknown cases. Their codes are '2 0 0', '0 0 2', '2 2 2', '2 2 2', '1 0 0' and '1 0 0', but the code of high energy discharge is '1 0 2'. These six cases are obtained from faults of arc in selector switch, short circuit in distribution windings, arcing from windings to porcelain, tertiary windings

damaged by arcing, bushing swollen, tank opened and arcing to the magnetic circuit. All these cases except the 7th case are correctly classified by using Duval Triangle.

## 3.6 Summary

In this chapter, 134 fault cases, including lab simulated cases and fault cases identified by inspection of the equipment, are applied as testing dataset. The repeatability and average accuracy of twenty-five experienced laboratories from 15 different countries has been reviewed for determining the variation value. According to CIGRE default accuracy of medium-range concentrations and low-range gas concentrations,  $\pm 5\%$  variation values are calculated and all these values are added to the lab simulated gas cases. Meanwhile,  $\pm 10\%$  variation values are computed and all these values are added to those fault cases identified by inspection of the equipment.

Two important DGA methods, Duval triangle and IEC ratio method, are applied as classification methods. All the fault diagnostic results are obtained by using the variations. The corresponded final decisions are achieved by calculating the corrected classifications of gas records with variations. By carefully discussing the results, three zones are concluded in the original Duval triangle graphic for improving the reliability during application. The first one indicates a zone that a high possibility of misclassification of discharge faults. Bushing arcing faults and all tracking faults are highly tended to be classified as high energy discharge. Arcing in low voltage windings and flash-over fault appear in the zones as a low energy discharge. The second zone represents a zone that a high possible misclassification of overheating faults. In this zone, the gas records can be misclassified as a fault either greater than  $700\text{ }^{\circ}\text{C}$  or smaller than  $700\text{ }^{\circ}\text{C}$ . The threshold value of  $\text{C}_2\text{H}_4\%$  in the third zone decreases from 98% to 96%. All the 21 possible cases of IEC gas ratio have been calculated for a given gas record. The final result of IEC ratio method is obtained by calculating the correct classification numbers among these 21 cases. The classification result indicates that many unknown cases, which cannot be determined by using IEC ratio method, are generated when the variations are

considered in the fault detection. Error redundancy of IEC ratio method is lower than Duval Triangle due to the lack of codes.

## **Chapter 4**

# **Approaches to Incipient Fault Detection for Oil-Immersed Power Transformer using Support Vector Classifiers**

Incipient fault detection methods using a novel hybrid classifier are developed for dissolved gas analysis of oil-immersed power transformers. Four New fault features are derived by analyzing various industry standards of dissolved gas analysis. Two effective data pre-processing methods are employed for improving diagnosis accuracies. Bootstrap is first utilized to equalize sample numbers of different fault types, and then the logarithmic transformation is applied to generate additional classification features. In experiments, a least-square support vector machine, support vector machine, and support vector data description are developed as fault classifiers, and the optimal parameters of the three classifiers are obtained using particle swarm optimization. A comprehensive comparison is made regarding the performance of the three support vector machine based classifiers for the first time in the area of dissolved gas analysis. Moreover, classification boundaries are illustrated to provide an in-depth understanding upon the performance of each classifier with clear visualization figures. The results indicate that least-square support vector

machine can significantly improve the diagnosis accuracy of dissolved gas analysis along with the proposed pre-processing methods.

## 4.1 Introduction

Trend analysis of In this chapter, the research will focus on dealing with the nonlinear DGA data using the support vector classifiers. As knew in preceding chapter, oil-immersed power transformer is a vital apparatus in a power system and its reliability is very important to system operations. Although the aging failure probability of the transformer is reduced by adopting distributed electrical generation units, it could be still suffer from thermal stresses and chemical stresses as mentioned before. More specifically, thermal stresses significantly affect the properties of transformer oil by the formation of acidic products, which can lead to the degradation of insulation [48]. Despite their significant contributions in assuring transformer normal operations, there are still some drawbacks in the current practice, e.g. “lack code” [49], rigorous borderline and hidden relationships as mentioned in the preceding chapter.

As the development of computational aided techniques, support vector based classifiers are good tools to solve nonlinear classification, which can be applied to solve this problem. Support vector machine (SVM) and its variants have attracted great attention in the past decade. SVM consists of three main advantages, i.e. small training data samples, short training time and unique solution from convex quadratic programming. SVM has been used for fault classification in a two-terminal overhead transmission line using limited feature data extracted by wavelet [50]. In addition, other variants of SVM, e.g. support vector data description (SVDD) [51] and least-square support vector machine (LS-SVM), have emerged to tackle different classification problems. In our previous work, comparison between LS-SVM and ANN indicates that LS-SVM with a radial basis function (RBF) has excellent classification accuracy as well as lower computational cost [20]. The preliminary results motivated this research on support vector based classifiers for DGA in this chapter.

Two main factors should be concerned when a support vector based classifier is applied. The first one is the statistical characteristic of input data vectors. However, the number of data used for training and validation may be unequal regarding different fault types of dissolved gas data. In most cases, it is due to the lack of data related to different fault conditions. In addition, collected gas data possess essential diversity even related to the same condition faults because of a large variety of types of transformers investigated. These data often cause low diagnosis accuracy. The other significant factor is the preset values of parameters for the above classifiers. Mismatched combinations of them may lead to low classification accuracy. Particle swarm optimisation (PSO) was adopted in [52] for LS-SVM classifier.

In section 4.2, the logarithmic transformation of conventional gas ratios is introduced as additional features. More specifically, a 10 base logarithmic transformation is applied to select ratios of combustible gases against the total gas volume as well as the total gas volume itself. Meanwhile, lack of faculty class samples is overcome by bootstrap pre-processing [53]. Furthermore, SVM, LS-SVM and SVDD are discussed in section 4.3. PSO is used for searching the optimised combination of parameters for the RBF kernel function and penalty in the proposed classifiers. In section 4.5, classification accuracies as well as a confusion matrix, which are obtained from classifiers with optimized parameters, are illustrated. Comparisons between classification results of conventional gas ratios and results using the proposed additional feature ratios are illustrated. It is a clear indication that PSO-LSSVM has the highest classification accuracy using additional feature ratios. In order to submit an in-depth understanding of the classification principles, the corresponding decision boundaries of the three classifiers are drawn in 3D figures for clear presentation.

## 4.2 Pre-process DGA Data

### 4.2.1 Logarithmic Transform of DGA Concentrations

The majority of transformers present low dissolved gas concentrations of a few ppm, while faulty transformers may produce thousands or tens of thousands of ppm.

Therefore, dissolved gas records demonstrate typically in highly skewed distributions. Some values of a fat-tail distribution can cause numerical impreciseness, classification overflow and visualisation difficulty. This fat-tail distribution is, at the same time, difficult to visualize, and the extreme values can be a source of numerical imprecisions and overflows in a statistical learning algorithm [54]. Considering these facts, a natural way of DGA data preprocessing can be achieved by using the logarithmic transformation. Due to the lack of CO data, in this research, the new total gas volume (TGV) of inflammable carbon-hydron containing gases, which consists of  $[H_2 + CH_4 + C_2H_2 + C_2H_4 + C_2H_6]$ , is employed. In addition, inspired by Duval Triangle method, the three most sensitive gases percentage of  $C_2H_6$ ,  $C_2H_4$  and  $C_2H_2$  are chosen as additional features. Based on these two main points, the additional features are then obtained by taking a normal  $\log_{10}$  for the selected inflammable gas ratio against TGV and TGV itself. For example, an additional feature can be derived as  $\log_{10}^{(\frac{C_2H_4}{TGV})} = \log_{10}^{C_2H_4} - \log_{10}^{TGV}$ .

#### 4.2.2 Basic Theory of Bootstrap

Bootstrap is a resampling technique, which draws a large number of samples from initial data repeatedly [55]. The aim is to achieve reliable standard errors, confidence intervals as well as other measures of uncertainty in the case that the initial sample number is insufficient for accurate analysis when applying other statistical techniques [56]. Consider  $X = \{x_1, x_2, \dots, x_n\}$  to be a set of  $N$  samples with unspecified distribution  $F$ , where  $X$  are independent and identically distributed random variables. Suppose  $\vartheta$  is one of the possible characteristic of  $F$ , for instance mean or variance. In order to acquire  $k$  sets of samples  $X_m = \{x_{m1}, \dots, x_{mn}\}, (m = 1, \dots, k)$ , an estimator  $\vartheta'$  of  $\vartheta$  is calculated by bootstrap to resample the initial set  $X_m$ . Each generated samples  $x_{mn}$  has a probability  $\frac{1}{n}$  of being equally picked up for resampling. Consequently, for each generated set of samples  $X_m$  it is possible to calculate an estimator  $\vartheta_m^\wedge$  with the purpose to analyse its probability distribution function  $F(\vartheta^\wedge)$  and a confidence interval for the estimator [56]. In this chapter, collected DGA data is resampled by bootstrap to equalise the sample number for each fault type.

## 4.3 Support Vector Based Classification Methods

Three support vector based classifiers are discussed in this section. SVM represents a linear quadratic programming extension to nonlinear models, which is developed by Vapnik based on the statistical learning theory and Vapnik-Chervonenkis (VC) dimension theory [57]. LS-SVM [58] is proposed by Suyken as reformulations to standard SVM, which simplifies the model of standard SVM to a great extent by applying linear least squares criteria to the loss function. The simplicity and inherited advantages of SVM are its excellent generalization ability and a unique solution, which promote widespread applications of LS-SVM. Unlike SVM or LS-SVM, SVDD concerns the characterization of the target data set. The validation data is spherically shaped by a boundary to distinguish between the target data and outliers [59]. It is often applied to classification problems where the target class is sampled very well, while the outliers is severely undersampled. All the mentioned classifiers are applied with the RBF kernel function [58] in this chapter.

### 4.3.1 Support Vector Machine

In case of SVMs, a high dimensional hyperplane is generated by training vectors and it can separate validation data. An ideal linear classification with two input features in a high dimensional space is displayed in Figure 4.1. Two parallel hyperplanes are represented by dashed lines at the joint edges of both class data and no training data fall between them. These points which lie on the hyperplane are known as support vectors. A unique optimal separating hyperplane represented by the solid line is obtained through maximizing the distance between the two parallel hyperplanes. The general methodology is to start formulating a problem in the primal weight space as a constrained optimization problem, next formulate the Lagrangian, finally solve the problem under optimality conditions in the dual space of Lagrange multipliers. Considering a simple binary classification problem with a training set  $\{(x_k, y_k)\}_{k=1}^n$ , where  $y_k$  is the label of the input data class  $x_k$ . In the bi-classification case,  $y_k \in \{-1, 1\}$  and  $x_k \in R^d$ , where  $d$  is the dimension of



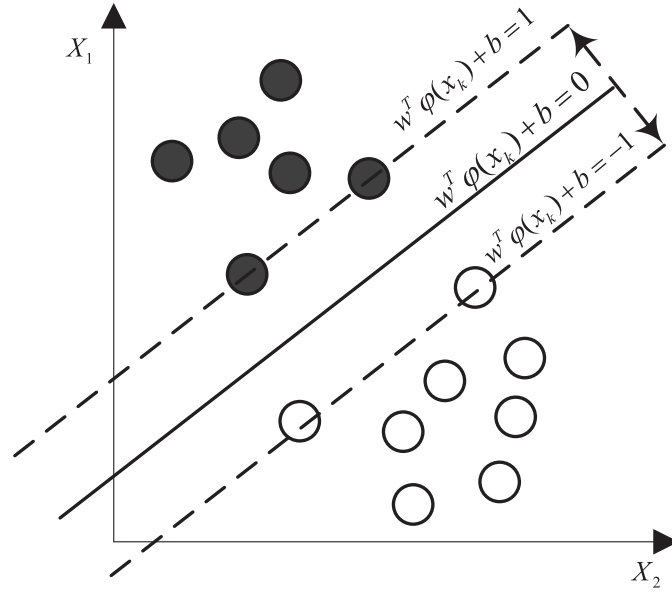


Figure 4.1: Maximum-margin hyperplane for an SVM with samples from two classes

input vectors. The SVM approach aims to search a classifier in the form of [60]:

$$y(x) = \text{sign} \left[ \sum_{k=1}^n \alpha_k y_k K(x_k, x) + b \right] \quad (4.3.1)$$

where  $\alpha_k$  is positive real constant of Lagrange multiplier, which is the solution of the dual problem for the following quadratic programming problem. Kernel function  $K(x_k, x) = \varphi(x_k)^T \varphi(x)$ , and  $\varphi(\cdot)$  represents the nonlinear mapping function from the original space to a high dimensional space.

The two parallel hyperplanes in Figure 4.1 can be described by the following two equations:

$$\begin{cases} w^T \varphi(x_k) + b \geq +1, & \text{if } y_k = +1 \\ w^T \varphi(x_k) + b \leq -1, & \text{if } y_k = -1 \end{cases} \quad (4.3.2)$$

where  $w$  is the normal vector and  $b$  is the constant of hyperplane. The margin distance equals  $\frac{2}{\|w\|}$ , which means the minima distance from the hyperplane to support vectors is  $\frac{1}{\|w\|}$ . In other words, maximizing the margin is archived by minimizing  $\|w\|$ , which can be represented by the following quadratic programming

(QP) problem:

$$\begin{aligned} \min_{w,b,\xi} J_P(w, \xi) &= \frac{1}{2}w^T w + C \sum_{k=1}^n \xi_k \\ \text{subject to : } &y_k [w^T \varphi(x_k) + b] \geq 1 - \xi_k, \quad \xi_k \geq 0, \\ &k = 1, \dots, n \end{aligned} \quad (4.3.3)$$

where  $C$  is called the penalty parameter of error term and  $\xi_k$  is the slack variable, which is used for “soft” classification. There are other typical Kernel functions for mapping, which are proposed as following: RBF :  $K(x_k, x) = \exp(-||x_k - x||^2/\varsigma^2)$ ; polynomial kernel:  $K(x_k, x) = (x_k^T x + l)^p$ . Here  $\varsigma$ ,  $l$ , and  $p$  are kernel parameters, which should be given before calculation. It is important to note that the Mercer condition holds for all  $\varsigma$  values in the RBF kernel case and positive  $r$  values in the polynomial case. For multi-class classification in this chapter, it is necessary to effectively extend the binary classification model. Currently, two types of approaches to multi-class SVM are used. One is by constructing and combining several binary classifiers while the other is by directly considering all data in one optimization formulation. The former one has been applied in this chapter, i.e. the directed acyclic graph support vector machines (DAGSVM) [61] method.

### 4.3.2 Least-Square Support Vector Machine

An advantage of SVM is that nonlinear classification and regression problems can be solved by means of convex quadratic programming. Meanwhile, sparseness problems may occur in a QP problem. Modification of SVM should achieve simplification of its formulation without losing its advantage. The standard SVM formulation is modified at two main points for this aim. Firstly, rather than inequality, LS-SVM takes equality constraints where the value 1 at the right hand side is preferred as a target value. Secondly, error slack variables are added since misclassification must be tolerated in the case of overlapping distributions. Furthermore, a squared loss function is adopted for this error variable, in which the problem is greatly simplified with these modifications [58].

$$\begin{aligned} \min_{w,b,e} J_P(w, e) &= \frac{1}{2}w^T w + C \frac{1}{2} \sum_{k=1}^n e_k^2 \\ \text{such that : } &y_k [w^T \varphi(x_k) + b] = 1 - e_k, \quad k = 1, \dots, n. \end{aligned} \quad (4.3.4)$$

where  $C$  is called the penalty parameter of error term and the Lagrangian for the above problem is

$$\mathcal{L}(w, b, e, \alpha) = J_P(w, e) - \sum_{k=1}^n \alpha_k \{y_k [w^T \varphi(x_k) + b] - 1 + e_k\}, \quad (4.3.5)$$

where Lagrange multiplier  $\alpha_k$  equals to  $Ce_k$ , which can be positive or negative according to equality constraints. Defining  $M^T = [\varphi(x_1)^T y_1; \dots; \varphi(x_n)^T y_n]$ ,  $y = [y_1; \dots; y_n]$ ,  $1_v = [1; \dots; 1]$ ,  $e = [e_1; \dots; e_n]$ ,  $\alpha = [\alpha_1; \dots; \alpha_n]$ , and eliminating  $w$  and  $e$ , the following linear Karush-Kuhn-Tucker (KKT) system is obtained [62].

$$\left[ \begin{array}{c|c} 0 & y^T \\ \hline y & S + I/C \end{array} \right] \begin{bmatrix} b \\ \alpha \end{bmatrix} = \begin{bmatrix} 0 \\ 1_v \end{bmatrix}, \quad (4.3.6)$$

where  $I$  is an identity matrix,  $S = M^T M$  and the kernel function can be applied within the  $S$  matrix

$$\begin{aligned} S_{kl} &= y_k y_l \varphi(x_k)^T \varphi(x_l) \\ &= y_k y_l K(x_k, x_l), \quad k, l = 1, \dots, n. \end{aligned} \quad (4.3.7)$$

The classifier in the dual space of Lagrange is:

$$y(x) = \text{sign} \left[ \sum_{k=1}^n \alpha_k y_k K(x_k, x) + b \right], \quad (4.3.8)$$

which is similar to a standard SVM case. However, the final solution can be well expressed as unknown error variables  $e_k$  by eliminating  $a_k$ . Meanwhile, LS-SVM has the following three properties. The choice of kernel function must be positive definite and the Mercer condition should be satisfied. The correspondent KKT system in a dual problem which has a unique solution if the matrix has a full rank.

### 4.3.3 Support Vector Domain Description

The basic idea of SVDD is to find a spherically shaped boundary around a training dataset, which can enclose as many target samples as possible during validation. This sphere is characterised by its center and radius. To fit the hypersphere to the data, minimization of its volume is achieved by minimising its square radius  $r^2$  [59].

More specifically, a data set  $\{x_1, \dots, x_n\}$  can be described by a hypersphere with center  $o$  and radius  $r$ . To allow the outliers in a data set, distance from  $x_k$  to centre  $o$  should not be strictly smaller than  $r$ , but larger distances should be penalized. Analogous to a support vector classifier, a slack variables  $\xi$  and an extra parameter  $C$  are used for the trade-off between the volume of hypersphere and errors.

$$\begin{aligned} \min_{r, \xi} J_P(r, \xi) &= r^2 + \frac{1}{nC} \sum_{k=1}^n \xi_k \\ \text{subject to : } &\left\|x_k - \frac{1}{nC}\right\|^2 \leq r^2 + \xi_k, \quad \xi_k \geq 0. \end{aligned} \quad (4.3.9)$$

When  $x_k$  is within a sphere or on the boundary, the corresponding  $\xi_k$  is equal to 0. On the other hand,  $x_k$  is out of sphere with  $\xi_k > 0$ . The dual problem in Lagrange multipliers is represented as: The distance from a test sample  $z$  to the center of the sphere has to be calculated first. If this distance is smaller than or equal to the radius, the test object is accepted. The inner product  $(x_k \cdot x_l)$  can be replaced by a kernel function  $K(x_k, x_l) = (\varphi(x_k) \cdot \varphi(x_l))$  for nonlinear classification.

## 4.4 Particle Swarm Optimisation

Undesirable combinations of predetermined parameters for the proposed classifiers may lead to low classification accuracy. A variety of methods can be used to search the best combination. GA is a typical evolutionary algorithm, which is widely applied for optimisation problems. However, GA cannot assure constant convergence times. Compared with conventional gradient methods, the GA average convergence time is larger. This weakness limits the GA in some real-time applications. Unlike GA, PSO optimises an object function without complicated evolutionary operation, which leads to short convergence time. PSO is originally attributed to Dr Kennedy and Dr Eberhart [63]. It was intended for simulating the migration and aggregation of bird flock when they seek for food [64]. Supposing a swarm of size  $S$ , each particle can be characterized by position  $P_k^d(t)$  and velocity  $V_k^d(t)$  ( $k = 1, \dots, S$ ) in  $d$ -dimensional search space,  $t$  represents the time step. By iteratively improving a solution space with regard to a given fitness function, each particle keeps track of its coordinates in the hyperspace which is associated with

Table 4.1: 90% Typical normal values (ppm) for power transformers without a communicating OLTC [9]

Year	Company	H <sub>2</sub>	CH <sub>4</sub>	C <sub>2</sub> H <sub>2</sub>	C <sub>2</sub> H <sub>4</sub>	C <sub>2</sub> H <sub>6</sub>	CO	CO <sub>2</sub>
76	LCIE	134	134	0	45	157	1008	10528
80	Alsthom	100	200	20	200	200	1000	10000
81	EDF	0	225	3	110	225	785	4500
82	Asinel	105	125	10	166	71	2000	18000
85	Chili	100	50	15	50	65	500	5000
88	Asinel	100	70	10	170	70	1000	10000
92	Vattenfall	200	50	3	200	50	1000	20000
93	Haefely	125	100	20	150	100	500	6000
93	Asinel	100	70	10	170	70	1000	10000
95	Enel	95	280	10	150	250	700	8000
96	Labelec	60	40	3	60	50	540	5100
96	Laborelec (tight OLTC)	84	79	56	166	52	673	8068
88	Asinel	50	10	5	10	10	1000	10000
93	Labelec	6	11	1	3	7	250	800
93	Milan Vidmar	150	120	1	40	130	1100	4000
96	ABB (CT, rubber seal)	20	30	2	4	25	330	900
96	ABB (CT, metal seal)	300	30	2	4	25	330	900

the best solution it has achieved so far. This value is called  $pbest^d(t)$ . Meanwhile, another best value called  $gbest^d(t)$  is also tracked, which is obtained thus far by any particle in the population. At each time step, PSO changes its velocity towards its final  $pbest$  and  $gbest$ . Acceleration is weighted by a random term with separate random numbers being generated. After finding these two best values at each time, a particle updates its velocity and positions according to the following equations for the next step.

$$\begin{aligned}
 V_k^d(t+1) &= V_k^d(t) + c_1 \cdot \text{rand} \cdot (pbest^d(t) - P_k^d(t)) \\
 &\quad + c_2 \cdot \text{rand} \cdot (gbest^d(t) - P_k^d(t)) \\
 P_k^d(t+1) &= P_k^d(t) + V_k^d(t+1)
 \end{aligned} \tag{4.4.1}$$

rand indicates a random number, which is generated between 0 and 1.  $c_1$  and  $c_2$  are learning factors.

Table 4.2: 90% Typical normal values (ppm) for power transformers with a communicating OLTC [9]

Year	Company	H <sub>2</sub>	CH <sub>4</sub>	C <sub>2</sub> H <sub>2</sub>	C <sub>2</sub> H <sub>4</sub>	C <sub>2</sub> H <sub>6</sub>	CO	CO <sub>2</sub>
76	LCIE	235	180	336	145	270	672	4256
88	Asinel	250	150	150	250	150	1000	10000
92	Vattenfall	200	50	30	200	50	1000	20000
93	Enel	200	100	50	100	100	500	10000
93	Asinel	250	190	180	250	180	1000	10000
96	Labelec	75	35	80	110	50	400	5300
96	Laborelec	151	131	266	250	73	848	11818
92	LCIE	134	224	154	224	550	672	3584
93	LCIE / EDF	0	150	150	200	550	800	5000

Table 4.3: Influence of various parameters on 90% typical (normal) values in power transformers [9]

Parameter	H <sub>2</sub>	C <sub>2</sub> H <sub>2</sub>	C <sub>2</sub> H <sub>4</sub>	C <sub>2</sub> H <sub>6</sub>
Transformer sub-type				
Sealed	100	35	50	
Breathing, transmission	150	10	280	
Breathing, generation	100	50	200	
Fault type				
Discharges	85	70	35	8
Thermal	175	3	375	100
Age, in years				
<2	60	5	5	2
2- 5	100	100	60	15
10 - 20	200	80	80	20
> 20	400	150	100	30

## 4.5 Results and Discussion

Table 4.1 and Table 4.2 illustrate 26 gas records of 90% typical normal values (ppm) for power transformers with and without a communicating OLTC. Details, including years and company, are also provided for fault detection. Other 69 overheating samples, low energy discharge (18 samples) and high energy discharge (54 samples) are obtained from IEC10 [4] [9]. In addition to the ages of the transformer, the sampling location and technique, type of dielectric coolant, test method, and data analysis method are important to keep in mind when considering an analysis. For example, the presence of even a trace amount of acetylene could be a problem for bolted cover designs, but it would not be cause for concern in welded cover transformer designs. It is also quite important to look at the trend of the dissolved gas content of samples taken from one transformer over a period time. This will make it more apparent which variables are affecting the DGA levels and help prevent a misdiagnosis. In this research, 167 sets of original gas data, which include  $H_2$ ,  $CH_4$ ,  $C_2H_6$ ,  $C_2H_4$  and  $C_2H_2$ , are taken directly from IEC 10 [9] [4]. The DGA data have been evaluated using various engineering diagnostic tools by industry experts and the corresponding diagnoses related to four fault classes have been provided, i.e., normal unit (26 samples), overheating (69 samples), low energy discharge (18 samples) and high energy discharge (54 samples). They were acquired during decades from a large number of power transformers. The five commonly used gas ratios  $X$ , which are listed in equation (4.5.1), are the same as they are used in [53]. The three most sensitive gases and total gas volume are chosen to derive additional features  $X_{add}$ , which are defined in equation (4.5.2).

$$X = \left[ \frac{C_2H_2}{C_2H_4}, \frac{CH_4}{H_2}, \frac{C_2H_4}{C_2H_6}, \frac{C_2H_2}{H_2}, \frac{C_2H_6}{C_2H_2} \right] \quad (4.5.1)$$

$$X_{add} = \left[ \log_{10}^{(\frac{C_2H_6}{TGV})}, \log_{10}^{(\frac{C_2H_4}{TGV})}, \log_{10}^{(\frac{C_2H_2}{TGV})}, \log_{10}^{(TGV)} \right] \quad (4.5.2)$$

The Duval Triangle method can be applied only if there is some suspicion of a fault, based on an increase in combustible gas or some other suspicious symptom. Because of the relative inaccuracy of gas-in-oil concentration measurements at low concentrations, DGA diagnostic methods, including the Duval Triangle, cannot be

applied unless the gas concentrations are well above the detection limit.

Figure 4.2 shows the classification results and the coded list of faults are: PD = partial discharges; D1 = discharges of low energy; D2 = discharges of high energy; T1 = thermal faults of temperature  $< 300^\circ\text{C}$ ; T2 = thermal faults of temperature  $300^\circ\text{C} < T < 700^\circ\text{C}$ ; T3 = thermal faults of temperature  $> 700^\circ\text{C}$ . Without considering the normal data, the final classification result of Duval Triangle is 80.14% (113/141).

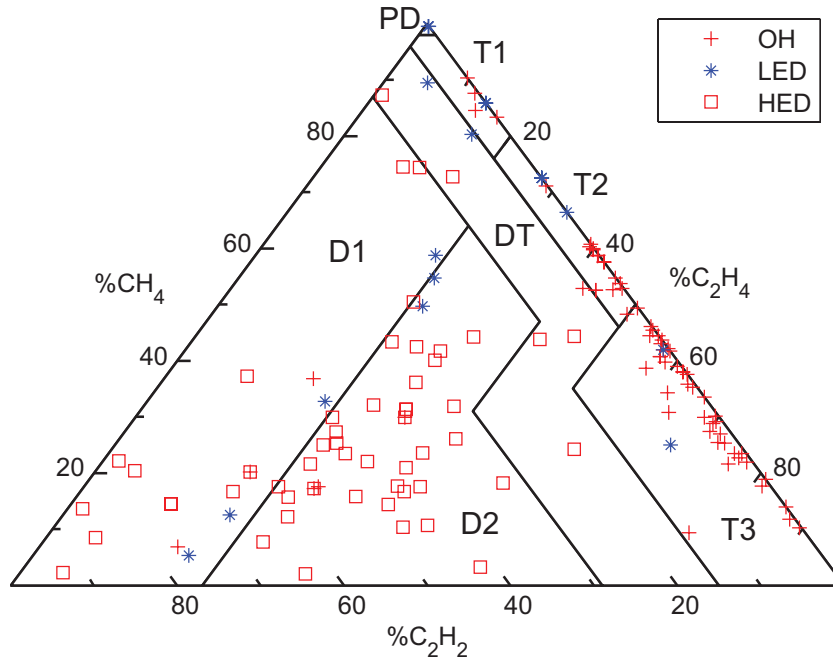


Figure 4.2: Classification result using Duval triangle

#### 4.5.1 Sample Number Equalisation for Different Fault Classes Using Bootstrap

In general, it is natural to obtain more accurate classification with DGA data using data set with equal number of samples regarding to different classes. In order to approximately equalise the samples number for each fault class, the bootstrapping has to be undertaken with the variable number of sets  $k$  for each class data depending on the initial number of the each class samples. Let  $n_i$  to be numbers of initial samples for corresponding  $i$ th fault classes in an initial dataset.  $i$  is from 1 to 4. Suppose  $N_{tr}$  and  $N_{ts}$  to be the desired equalised numbers of



Table 4.4: Length of 95% confidence intervals of gas ratio data

Class	C <sub>2</sub> H <sub>2</sub> /C <sub>2</sub> H <sub>4</sub>		CH <sub>4</sub> /H <sub>2</sub>		C <sub>2</sub> H <sub>4</sub> /C <sub>2</sub> H <sub>6</sub>		C <sub>2</sub> H <sub>2</sub> /H <sub>2</sub>		C <sub>2</sub> H <sub>6</sub> /C <sub>2</sub> H <sub>2</sub>	
	$\mu$	$\sigma$	$\mu$	$\sigma$	$\mu$	$\sigma$	$\mu$	$\sigma$	$\mu$	$\sigma$
NU <sup>a</sup>	0.32	0.38	35.12	7.22	2.71	2.51	0.5	0.67	26856	5640
OH <sup>b</sup>	0.28	0.89	13.37	60.417	7.65	8.54	0.95	3.47	83660	328000
LED <sup>c</sup>	0.70	1.04	0.72	0.86	2.87	5.63	0.48	1.28	13000	20500
HED <sup>d</sup>	5.40	10.48	0.53	0.96	14.98	37.28	2.85	14.85	0.25	0.53

<sup>a</sup> Normal Unit <sup>b</sup> Overheating <sup>c</sup> Low Energy Discharge <sup>d</sup> High Energy Discharge

samples for each class of newly generated training and testing datasets respectively. The sample number are firstly divided into two independently fractions  $cn_i$  and  $(1-c)n_i$  correspondingly, where  $c$  is a fraction parameter, which equals to 0.8 in this research. The bootstrapping is performed with the following function numbers of sets:  $k_{tr} \cong \frac{N_{tr}}{cn_i}$  and  $k_{ts} \cong \frac{N_{ts}}{(1-c)n_i}$ . The number of sets  $k$  has to be an integer value for data bootstrapping, only integer values closest to actual ratios in these two equations will be accepted. So, the actual numbers  $N_{tr}$  and  $N_{ts}$  will not be perfectly equal to the desired values but close to them respectively. A standard MATLAB “crossvalind” function is applied to randomly divide the each initial dataset into five data partitions. Four of them will be combined to constitute the initial training data and the remaining partition is used as initial testing partition. As a result, approximately 80 % of the initially available gas data have been used to create a training dataset. The remaining part will be 20% of the initially data. As mentioned above, the initial numbers of units are 26, 69, 18 and 54. In this research,  $N_{tr}$  is 199 and  $N_{ts}$  is 30. After calculation, numbers of training and testing for normal unit are 230 and 20 respectively. By using the bootstrapping for each dataset, the final training dataset for each case are 230, 240, 224, 220, which represent normal units, overheating, low energy discharge and high energy discharge. And, the correspondent dataset numbers of testing are 20, 36, 28 and 80.

A publicly available bootstrap toolbox is used in this chapter. In Table 4.4, the 95% confidence interval lengths of mean  $\mu$  and standard deviation  $\sigma$  values for each diagnosis class are presented after bootstrapping. It shows that there is a large distribution both in the mean and standard deviation values for all input vector elements within each fault type data. For example,  $\mu$  is from 0.28 to 83660 while  $\sigma$

Table 4.5: PSO-SVM without additional features  $\xi = 0.5171$  and  $C = 13.5626$ 

Class	NU	OH	LED	HED	Accuracy	Overall Accuracy
NU <sup>a</sup>	9	11	0	0	45.00%	71.95%
OH <sup>b</sup>	0	36	0	0	100.00%	
LED <sup>c</sup>	0	0	28	0	100.00%	
HED <sup>d</sup>	6	9	20	45	56.25%	

Table 4.6: PSO-LSSVM without additional feature  $\xi = 2.5728$  and  $C = 4.2486$ 

Class	NU	OH	LED	HED	Accuracy	Overall Accuracy
NU	20	0	0	0	100.00%	49.39%
OH	0	36	0	0	100.00%	
LED	28	0	0	0	0.00%	
HED	33	16	6	25	31.25%	

is from 0.38 to 328000. Even for the same gas ratio, the distribution of different fault type is large. For instance,  $\mu$  is from 0.25 to 26856 in  $C_2H_6/C_2H_2$ . Thus, it indicates the gas data are sufficiently complicate to carry out experiment using bootstrap.

## 4.5.2 Classification Results

$\xi$  and  $C$  among Table. 4.5 to 4.10 are obtained through PSO training. All swarm particles start at random positions for each dimension. The velocity of each particle is randomised to a small value to provide initial random impetus to the swarm particles. The swarm size is 30 particles as well as 50 maximum iterations. The values of  $c_1$  and  $c_2$  are both given as 2.0. The initialisation particle space for searching is located between 0 and 100. PSO is applied for searching the best combinations of  $\xi$  and  $C$  with different classifiers. The confusion matrix is a specific table layout that allows visualisation of the performance for different classification algorithms. All matrixes for the classifiers are also illustrated in Tables 4.5 to

Table 4.7: PSO-SVDD without additional feature  $\xi = 0.6139$  and  $C = 0.2839$ 

Class	NU	OH	LED	HED	Outlier	Accuracy	Overall Accuracy
NU	0	0	20	0	0	0.00%	56.71%
OH	14	15	1	6	0	41.67%	
LED	0	0	28	0	0	100%	
HED	30	0	0	50	0	62.50%	

Table 4.8: PSO-SVM with additional features  $\xi = 0.0452$  and  $C = 71.7022$ 

Class	NU	OH	LED	HED	Accuracy	Overall Accuracy
NU	9	11	0	0	45.00%	68.90%
OH	1	29	0	6	80.56%	
LED	28	0	0	0	0.00%	
HED	0	0	5	75	93.75%	

Table 4.9: PSO-LSSVM with additional features  $\xi = 2.3820$  and  $C = 7.7891$ 

Class	NU	OH	LED	HED	Accuracy	Overall Accuracy
NU	20	0	0	0	100%	90.85%
OH	0	29	1	6	80.56%	
LED	0	0	28	0	100%	
HED	0	4	4	72	90%	

4.10. Each column of the matrix represents the instances in a predicted class, while each row represents the instances in an actual class. The overall accuracy in each matrix is obtained by dividing the sum of the matrix diagonal values of overall data numbers, e.g. the overall accuracy is 71.95% (118/164) in Table 4.5. And the classification for each class is also given, for instance, the classification accuracy of NU is 100%(20/20) in Table 4.5. In the classification situation without additional features, PSO-SVM shows the highest accuracy of 71.95% while the PSO-LSSVM demonstrates the lowest accuracy is 49.39%. When the input vectors comprise the additional features, the accuracy of PSO-LSSVM rises to the highest accuracy 90.85% in Table 4.9 while it decreases to 53.05% in PSO-SVDD as shown in Table 4.10. Compared with the classification accuracy of 49.39% without using additional features, the PSO-LSSVM has the highest accuracy of 90.85%. Compared with the all results, the PSO-LSSVM classification accuracy 90.85%, which are obtained by using the five ratios features together with the logarithmic transformation additional features, is the highest value. A comparison between Table 4.5 and Table 4.8 shows that the penalty parameter  $C$  is increased after PSO learning. The reason of this change is that a “soft” margin SVM with a big  $C$  is comparable to a “hard” margin SVM with small  $C$  in high-dimensional data classification. Furthermore, the LED classification accuracy decreases to 0 as shown in Table 4.8 when the input vectors contain the additional features, which also reduce the overall accuracy. Compared

Table 4.10: PSO-SVDD with additional features  $\xi = 0.4562$  and  $C = 0.1918$ 

Class	NU	OH	LED	HED	Outlier	Accuracy	Overall Accuracy
NU	9	0	0	11	0	45.00%	53.05%
OH	15	0	21	0	0	0.00%	
LED	0	0	28	0	0	100%	
HED	0	0	30	50	0	62.50%	

with the results of Table 4.6 and Table 4.10, PSO-LSSVM has a great improvement in both HED and LED classification accuracies, which leads to a significant rise of the overall accuracy. Even though results in Table 4.7 and Table 4.10 present low alteration in overall accuracies, the classification confusion matrix of SVDD manifests significant variation even with the same optimized parameters during calculation. Meanwhile, it has an outlier feature in the confusion matrix under the multi-classification situation, which is due to the spherically shaped boundary. As SVDD is developed based on target classes well sampled and outlier undersampled, it is not appropriate for separating data after bootstrap. All these reasons lead to low overall accuracy for SVDD.

The four selected additional gas concentrations are quite sensitive to different types of faults. More specifically, low intensity discharges are always accompanied by small quantities of  $\text{CH}_4$  and acetylene  $\text{C}_2\text{H}_2$ . But the concentrations of  $\text{C}_2\text{H}_2$  and  $\text{C}_2\text{H}_4$  rise significantly as the intensity of the discharge increases. Moreover, when the intensity of electrical discharge reaches arcing, it produces overheating and the quantity of  $\text{C}_2\text{H}_2$  becomes the dominant gas. In other words, HED data have similar fault features with LED data and OH data. The main reason is that the HED data are sometimes diagnosed as LED and OH fault.

### 4.5.3 Classification Decision Boundary

The following figures are drawn for displaying the classification boundaries with reasonable approximation. SVM support vectors are obtained from both negative and positive classes after training. The bend curve is calculated by applying polynomial regression surface fitting with these selected support vectors. Although all the input data are support vectors for LS-SVM, those located at a range from

$e+0.5$  to  $e-0.5$ , which dominate the hyperplane, are used for polynomial regression surface curve fitting. The curve of SVDD is obtained by fitting the smallest ellipsoid function, which contains as many chosen support vectors as possible. Though this ellipsoid function is not from SVDD, the fitting surface is provided according to the same rules for visualisation. In order to present clear visualisation for these multi-classification problems, which consist of many bi-classifiers at different classification levels, different decision boundaries are obtained by these bi-classifiers. Certain decision boundaries are illustrated in this paper. More specifically, each classification method is given two decision boundaries. The first one is classification boundary between normal unit and faulty (FT) conditions, while the second one is classification boundary between normal unit and overheating (OH).

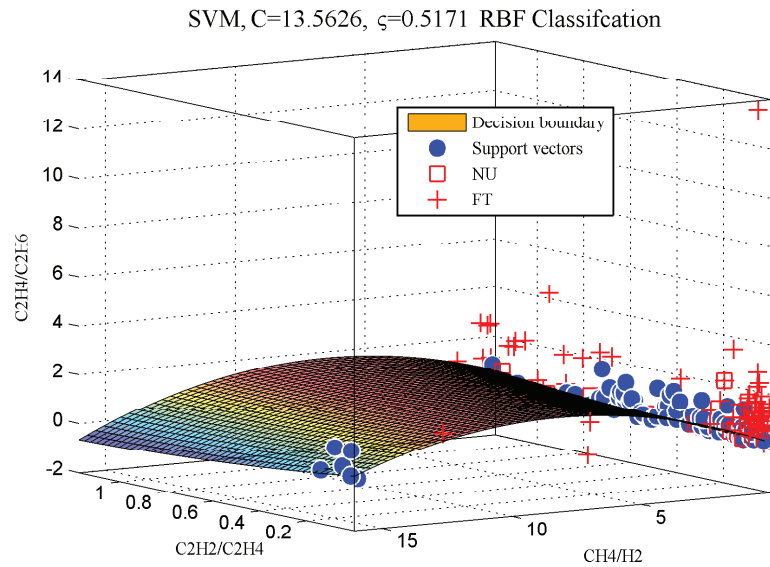


Figure 4.3: SVM classification using conventional features

As shown in Figure. 4.3 , the data are intensively distributed in the coordinate space and the approximate fitting curve surface cannot separate the data very effectively. Most of the data appear closely at the right-bottom corner, which also leads to a corresponding low classification accuracy 45.00%. For rescaled data classification, the corresponding decision boundaries are illustrated in Figure. 4.4 to Figure. 4.9. All the data are homogeneously dispersed in space after the logarithm

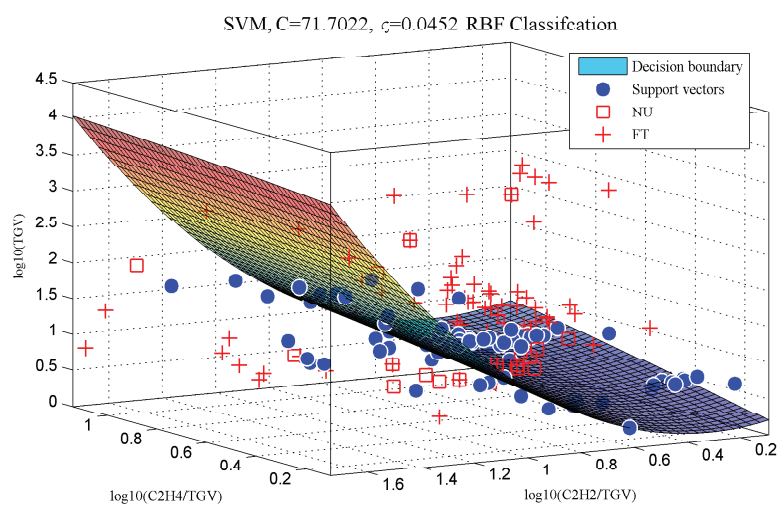


Figure 4.4: SVM classification using additional features

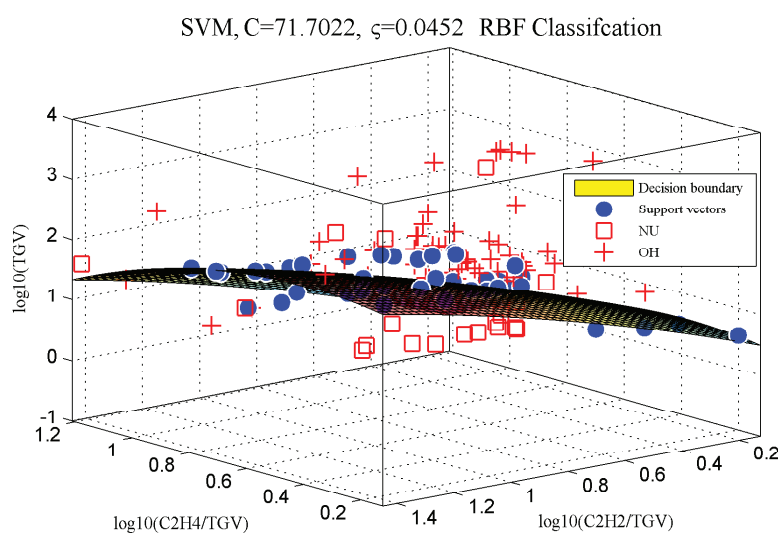


Figure 4.5: SVM classification using additional features

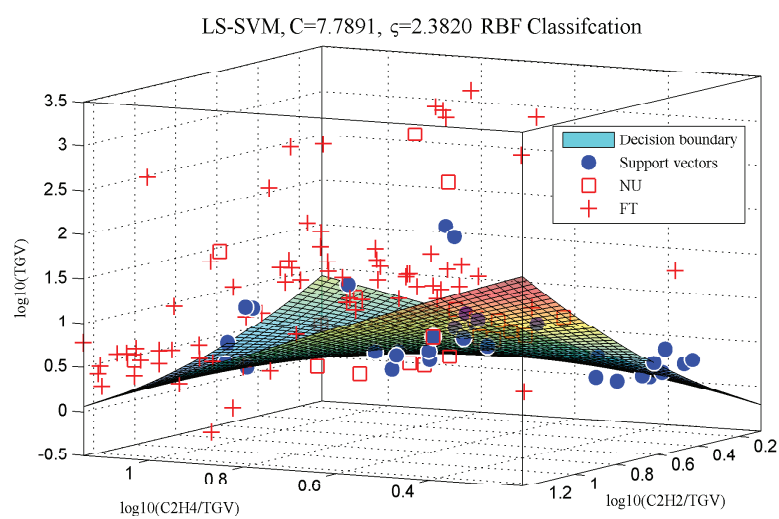


Figure 4.6: LS-SVM classification using additional features

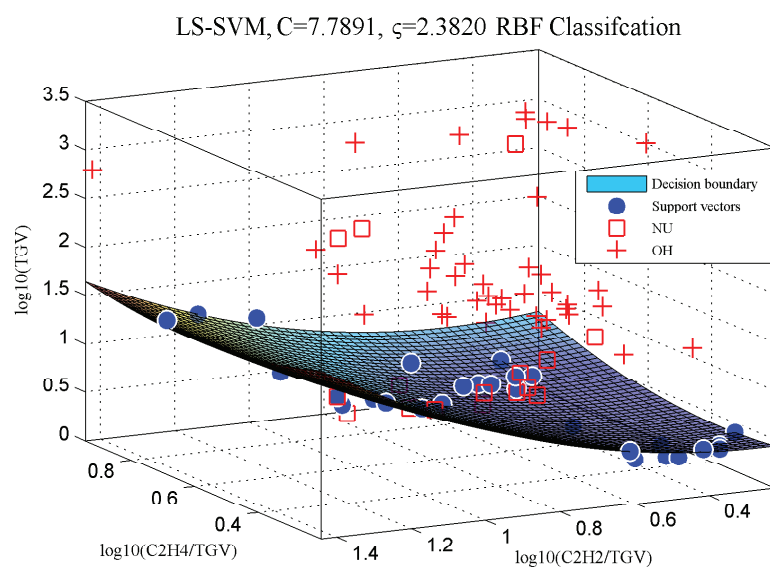


Figure 4.7: LS-SVM classification using additional features

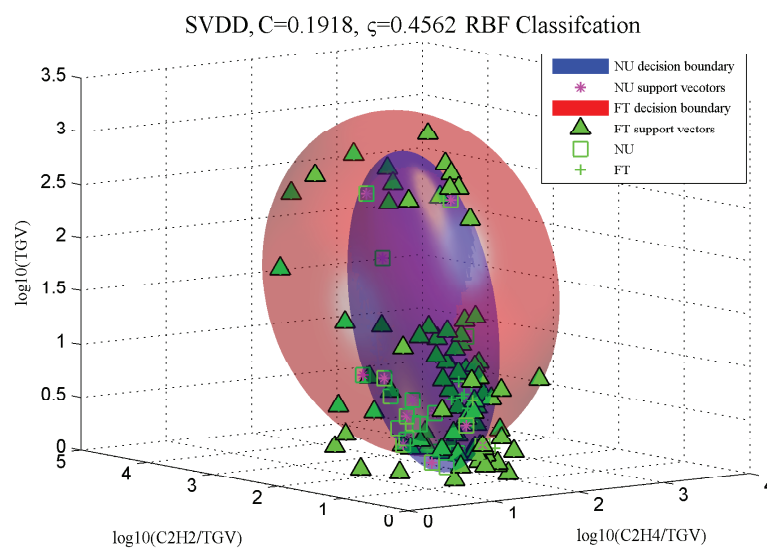


Figure 4.8: SVDD classification using additional features

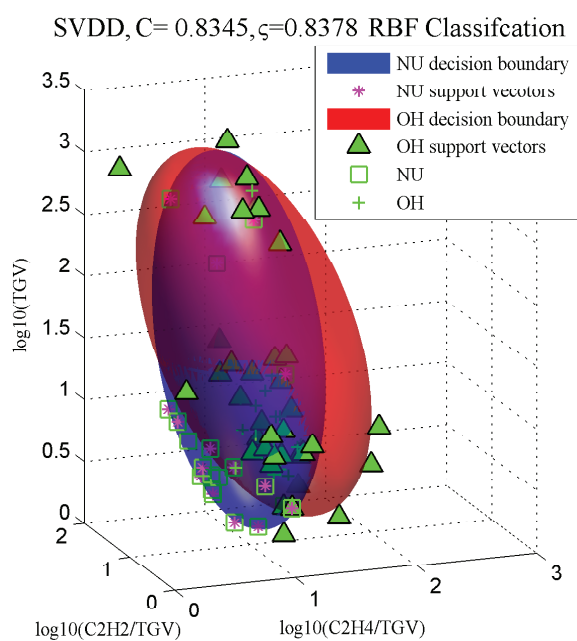


Figure 4.9: SVDD classification using additional features



transformation and the decision boundaries divide the data very well. The decision boundaries of LS-SVM in Figure. 4.6 and Figure. 4.7 present its strong capability in classification data, which leads to a high overall accuracy. However, Figure. 4.8 and Figure. 4.9 indicate that as the data become distributed the boundary curve of SVDD includes more outlier data, which illustrates SVDD is not suitable for highly distributed data classification.

## 4.6 Conclusions

In this chapter, three support vector based classifiers are developed to improve the classification accuracy. Two methods are applied for DGA data preprocessing. One is the resample tool bootstrap for overcoming the shortage of faulty data numbers while the other one is the logarithmic transformation of DGA concentrations, which rescale the gas ratio to generate additional features. PSO presents strong capability of searching the optimised combination of preset parameters for classifiers within a short convergence time. After final results of comparisons, PSO-LSSVM presents a significantly high classification accuracy among all the discussed methods, while fluctuation accuracy of PSO-SVDD indicates that it is not appropriate for multi-classification after the bootstrap processing. Comparisons of the decision boundaries with data in 3D figures indicate that additional features can enhance LS-SVM classification performance.

## **Chapter 5**

# **A Dissolved Gas Analysis Method Based on New Feature Prioritisation and Different Classifiers**

This chapter presents a novel approach to DGA feature prioritisation and classification, which considers not only the relations between a fault type and specific gas ratios but also their statistical characteristics based on data derived from onsite inspections. Firstly, new gas features are acquired based on the analysis of current international gas interpretation standards. Combined with conventional gas ratios, all features are then prioritised by using the Kolmogorov-Smirnov (K-S) test. The rankings are obtained by using their values of maximum statistical distance. The first three features in ranking are employed as input vectors to a multi-layer support vector machine (SVM), whose tuning parameters are acquired by particle swarm optimisation (PSO). In the experiment, a bootstrap technique is implemented to approximately equalise sample numbers of different fault cases. A common 10-fold cross validation technique is employed for performance assessment. Typical artificial intelligence classifiers with gas features extracted from genetic programming (GP) are evaluated for comparison purposes. The comparison of classification results indicates that the proposed method has superiority over other artificial intelligence classifiers with GP features.

## 5.1 Introduction

In general, feature extraction and preprocessing of DGA data are the two key procedures for achieving high fault diagnosis accuracy. In the precede chapter, three ratio additional features, which are  $\%C_2H_4$ ,  $\%C_2H_6$  and  $\%C_2H_2$ , are applied with support vector based classifiers in all situation. They are equal to  $C_2H_4/TGV$ ,  $C_2H_6/TGV$  and  $C_2H_2/TGV$ , where TGV is the sum of  $H_2$ ,  $CH_4$ ,  $C_2H_2$ ,  $C_2H_4$  and  $C_2H_6$ . However, some of them may be redundant and comparison of the results obtained from other artificial intelligence classifiers is also needed to be provided.

In previous research, a combined artificial neural network (ANN) and expert system tool is developed for transformer fault diagnosis using dissolved gas analysis [21]. A classification accuracy around 90% was achieved by using an essentially complex ANN structure. The diagnostic accuracy from 87% to 91% was obtained with regard to different ratio criteria. But it takes over 50000 iterations for reaching a preset mean error in ANN training [65]. Furthermore, different combined techniques were extensively applied to improve DGA classification accuracies. A hybrid multi-level decision model, which combined SVM with K-nearest neighbour (KNN), was proposed in [66]. With PSO optimised tuning parameters, SVM has also been applied to forecast the trend of dissolved gases [67]. A combination of fuzzy logic and ANN was presented in [68], and around 80% out of 212 gas samples were classified correctly. Recently, the presence of furanic derivatives was estimate by using artificial neural network (ANN) and ultra-violet-visible light absorbance property [69]. In addition, evolutionary programming has been applied to fault-section estimation in power systems [70]. Genetic programming (GP) were implemented to preprocess DGA data before applying different classifiers in [71].

Feature can be generated by analysing the characteristic of gas generation procedure. More specifically, new gas features need to be selected for particular classification situation, which can lead to a high overall classification accuracy. These features can be obtained based on the in-depth analysis of well-known DGA interpretation standards, which has been reveilles in chapter 1. Meanwhile, a fault feature prioritisation technique needs to be developed to verify selected new features. A statistical analysis of the corresponding data can be employed for this

purpose. The K-S test is a non-parametric method to measure the goodness of fit. In a two-sample K-S test, the basic procedure involves computing the empirical cumulative distribution function (ECDF) of given datasets, and comparing with each other. It has been applied to fast spectrum sensing [72] [73] and feature selection in emotional speech recognition [74]. In this chapter, it has been applied as a tool of new feature prioritisation.

In this chapter, new DGA features are first derived for discriminating different faults using the analysis of well-known fault interpretation standards. The maximum distance values of all the data in the feature set are calculated using the K-S test for feature prioritisation. The first three highly ranked features are applied as input vectors for fault classification. The bootstrap technique is also utilised to approximately overcome the lack of fault class samples as the precede chapter. Based on the analysis of the previous chapter, a basic multi-layer network SVM is applied as a classifier, whose tuning parameters are obtained by PSO. For comparison, KNN, ANN and SVM is applied with GP selection features. In the experiments, a 10-fold cross-validation procedure is applied in classification. Finally, a detailed comparison between the classification accuracy using the proposed method and that using KNN, ANN with GP selected features is presented.

## 5.2 New Feature Extraction and Data Preprocessing

As we discussed in the precede chapter 1, the two main reasons causing transformer faults are overheating and electrical stresses. For thermal faults, the relations between gas concentration abnormality and fault types are discussed in the Halstead's thermal equilibrium theory. The decomposition of mineral oil from 150 °C to 500 °C produces relatively large quantities of low molecular weight gases ( $H_2$  and  $CH_4$ ) and small trace quantities of higher molecular weight gases such as  $C_2H_4$ . The concentration of  $H_2$  exceeds that of  $CH_4$  when the temperature in oil increased. It also produces significant quantities of  $C_2H_4$  and  $C_4H_6$ . At the upper end of the thermal fault range, increasing quantities of  $H_2$  and  $C_2H_4$  and traces of  $C_2H_2$  may be produced. Compared with the thermal decomposition of oil, the decomposition

of cellulose releases large quantities of carbon monoxide (CO) and carbon dioxide (CO<sub>2</sub>).

In the situation under electrical stresses, low energy discharge faults, such as partial discharges and very low intermittent arcing, generate mainly H<sub>2</sub> and trace quantities of C<sub>2</sub>H<sub>2</sub>. The C<sub>2</sub>H<sub>2</sub> and C<sub>2</sub>H<sub>4</sub> concentrations rise significantly when the intensity of discharge increases. As the intensity of electrical discharge reaches arcing, the quantity of C<sub>2</sub>H<sub>2</sub> becomes predominant.

### 5.2.1 New Features Between Normal and Fault Cases

Regardless of variation of each gas during a fault, the total amount of combustible gases (TCG) increases under any fault conditions. Hence, an important feature, which can be used for separating the abnormal data from DGA data, is the total volume of combustible gases. In the Doernenburg method, if one of the four gas concentrations (H<sub>2</sub>, CH<sub>4</sub>, C<sub>2</sub>H<sub>2</sub> and C<sub>2</sub>H<sub>4</sub>) exceeds twice the value of its threshold and one of the other two gases (C<sub>2</sub>H<sub>6</sub> and CO) surpasses the preset limits, the unit is then considered as a faulty unit. Two values are adopted for identifying abnormal cases in this chapter. One is the total concentration of the four gases against its total threshold value 542 ppm (200 ppm + 240 ppm + 2 ppm + 100 ppm), which has been given in [1], for example, 200 ppm is the threshold of H<sub>2</sub>. The other one is the C<sub>2</sub>H<sub>6</sub> concentration over the threshold value 65 ppm.

Table 5.1: Rogers ratio for key gases

C <sub>2</sub> H <sub>2</sub> /C <sub>2</sub> H <sub>4</sub>	CH <sub>4</sub> /H <sub>2</sub>	C <sub>2</sub> H <sub>4</sub> /C <sub>2</sub> H <sub>6</sub>	Fault diagnosis
< 0.1	>0.1 to < 1.0	< 1.0	Unit normal
< 0.1	< 0.1	< 1.0	Low energy discharge
0.1 to 3.0	0.1 to 1.0	>3.0	High energy discharge
< 0.1	0.1 to 1.0	1.0 to 3.0	Low temperature thermal
< 0.1	>1.0	1.0 to 3.0	Thermal < 700 °C
< 0.1	>1.0	>3.0	Thermal > 700 °C

### 5.2.2 New Features Between Thermal and Discharge Cases

A new gas feature is obtained through the analysis of the Rogers ratio method, which can be applied for the classification between discharge and thermal faults. Referring to Table 5.1, the range values of  $C_2H_2/C_2H_4$  are the same in low energy partial discharge and thermal faults, which are both smaller than 0.1. In comparison, it falls into the range between 0.1 and 3 for high energy partial discharge faults. Although  $C_2H_2/C_2H_4$  has overlap range values between discharge faults and thermal faults, it denotes a relatively clear separation line between the two fault types, while there is no such distinct separation line for  $CH_4/H_2$  and  $C_2H_4/C_2H_6$ . The threshold for  $C_2H_2/C_2H_4$  is set to 0.1 in [75], which gain an accuracy of 96% in the classification between overheating faults and discharging faults. However, the overall accuracy of classification using  $C_2H_2/C_2H_4$  is relatively low, especially in classification between faulty cases and normal cases.  $CH_4/H_2$  falls into the 0.1-1 range in both low temperature thermal faults and high energy discharge faults, but it has a different value range in other faults. Compared with the previous two ratios,  $C_2H_4/C_2H_6$  overlaps in high energy discharge faults and thermal faults over 700° C, whose value for both cases are over 3.0. Hence,  $(C_2H_2/C_2H_4)/0.1$  is selected as a new feature in this study.

Additional features are obtained by analysis of the Duval Triangle. The Duval's triangle form for DGA is represented in Figure. 5.1 [4], and the area is separated by decision edges, which are mainly defined by  $\%C_2H_2$ ,  $\%CH_4$  and  $\%C_2H_4$ . The codes in the form are: PD = partial discharge, D1 = low energy discharge, D2 = high energy discharge, T1 = thermal faults of temperature  $< 150\text{ }^{\circ}\text{C}$ , T2 = thermal faults of temperature  $300\text{ }^{\circ}\text{C} < T < 700\text{ }^{\circ}\text{C}$ , T3 = thermal faults of temperature  $> 700\text{ }^{\circ}\text{C}$ . There is a Discharge-Thermal (DT) zone covering both thermal faults and discharge faults. The two threshold values of  $\%C_2H_2$  are 29% and 13%, which are used for separating the discharge fault area against the DT zone. In this study, a threshold value 21% of  $C_2H_2$ , which has an equal gap between 29% and 13%, is applied for the classification between overheating faults and discharge faults, which is calculated by  $(13\% + 29\%)/2$  as a trade-off value. The percentage value of  $C_2H_2$  above this value is viewed as thermal faults. On the contrary, values lower than this

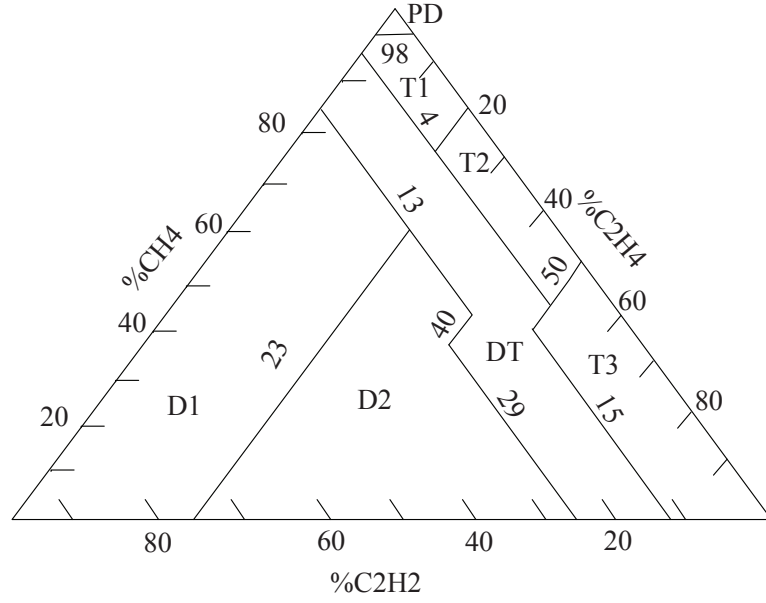


Figure 5.1: Triangle graphical form

percentage is regarded as discharge faults.

### 5.2.3 New Feature Between Low and High Energy Discharge Cases

Unlike the precede chapter, a base 2 logarithm transformation is applied due to a relative large curvature value. As shown in Figure.5.2, a clear and unique decision edge between low energy discharge and high energy discharge is defined by  $\%C_2H_4$  as 23% . As a result,  $(\%C_2H_4/0.23)$  is selected as a feature for the classification between low energy discharge faults and high energy discharge faults.

### 5.2.4 DGA Data Preprocessing

In this study, the logarithm transformations with base 2 are adopted for three newly derived features:  $(C_2H_2/C_2H_4) / 0.1$ ,  $\%C_2H_2/0.21$  and  $\%C_2H_4/0.23$ . Because the percentage values fall into a very narrow range between 0 and 1, a pre-process procedure is required to enlarge the distance of the centralised data. For instance,

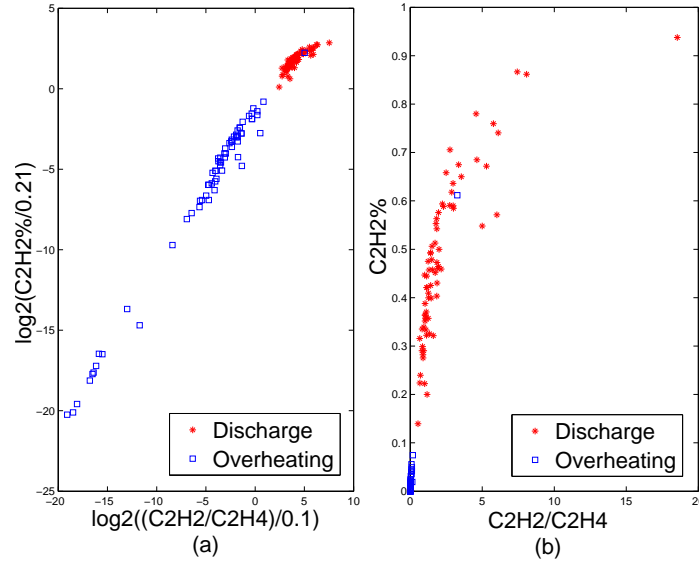


Figure 5.2: (a) Ratio values by using logarithm transformation. (b) Ratio values before logarithm transformation

the value of  $\%C_2H_2/0.21$  is between 0 and 1 if  $\%C_2H_2$  is lower than the threshold 0.21%, otherwise it is over 1. A logarithm function can map a data value to a negative value when its original value is between 0 and 1. But the value of logarithm transformation is a positive value if the original value is over 1. As a result, the logarithm transformation can be employed for enlarging the distance of the newly selected feature data. As shown in Figure. 5.2 (b), all the values of  $\%C_2H_2$  are originally located in between 0 and 1, but the distance between the values of the two fault categories is enlarged after logarithm transformation in Figure. 5.2 (a).

Bootstrap was a computer intensive resampling technique, which can draw a large number of resamples from initial data repeatedly [76]. This is designed to obtain reliable standard errors, confidence intervals, and other measures of uncertainty in cases when the initial sample number is not sufficient for accurate analysis by other statistical techniques. Because resampling is conducted in a random order, bootstrap assumes no particular distribution of processed data, which gives more applicability with respect to other classical statistical methods. This technique, which illustrates a well capability in improving the diagnostic accuracy of power transformer fault classification with highly versatile or noise corrupted DGA data [71], is applied for



equalise the sample numbers of different fault class.

In summary, the ratios of TCG/542 and  $C_2H_6/65$  are selected for the classification between normal and fault cases. In the classification between overheating and discharge faults,  $\log_2((\frac{C_2H_2}{C_2H_4})/0.1)$  and  $\log_2(\%C_2H_2/0.21)$  are proposed. The final selected feature for classification between high energy discharge and low energy discharge faults is  $\log_2(\%C_2H_4/0.23)$ .

## 5.3 Computational method for feature selection

### 5.3.1 Kolmogorov-Smirnov Test

The K-S test is a nonparametric test, which attempts to determine if two datasets differ significantly. Compared with other statistical methods, its main advantage is the independence from a particular statistical model, whose test performance is well only if the data adopts certain statistic distribution [77] [78]. For instance, the feature selection based on the Pearson correlation coefficient method is only effective when a linear relationship exists between two datasets. Otherwise, its accuracy drops. It is often difficult to obtain a correct statistical model of the given data especially based on DGA data. If the underlying statistical characterisation of the data is unknown, the K-S test can be used as a method for feature extraction. It has been used in different applications such as the differences in location, dispersion or changes, occurred between two samples from images [79]. There are two main types of K-S tests, i.e. one-sample K-S test and two-sample K-S test. In the one-sample K-S test, the probability distribution of a sample is compared with a reference probability distribution, while in two-sample K-S test the probability distributions of the two samples are compared with each other. Suppose that the first sample of  $X_1, \dots, X_m$  has a distribution with a cumulative distribution function (CDF)  $F(x)$  and the sample of  $Y_1, \dots, Y_n$  has a distribution with CDF  $G(x)$ . If  $F(x)$  and  $G(x)$  are the corresponding empirical CDF, the maximum difference between samples is defined by  $D_{mn}$  as follows:

$$D_{mn} = \sqrt{\frac{mn}{m+n}} \max |F_m(x) - G_n(x)|, -\infty < x < \infty, \quad (5.3.1)$$

where  $m$  and  $n$  are the numbers of two class samples. An example of CDF for the  $C_2H_2$  percentage in normal cases is given in Figure. 5.3 (a). The maximum distance  $d$  of  $C_2H_2$  percentage CDF between normal cases and overheating cases is shown in Figure. 5.3 (b). The maximum difference  $D_{mn}$  between them is equal to  $\sqrt{\frac{mn}{m+n}}d$ , where  $m$  and  $n$  are the number of samples of normal cases and overheating cases. In this research, the K-S statistical test is applied to all available features at different classification layers independently. For example, in the classification between normal cases and fault cases, all the maximum distances of selected features are calculated firstly. By ranking their maximum difference  $D$  values from big to small, the corresponding ranking orders of all features are obtained subsequently in this level. Then, the first three most important features are adopted for classification. Similar procedures are applied to the other two classification conditions.

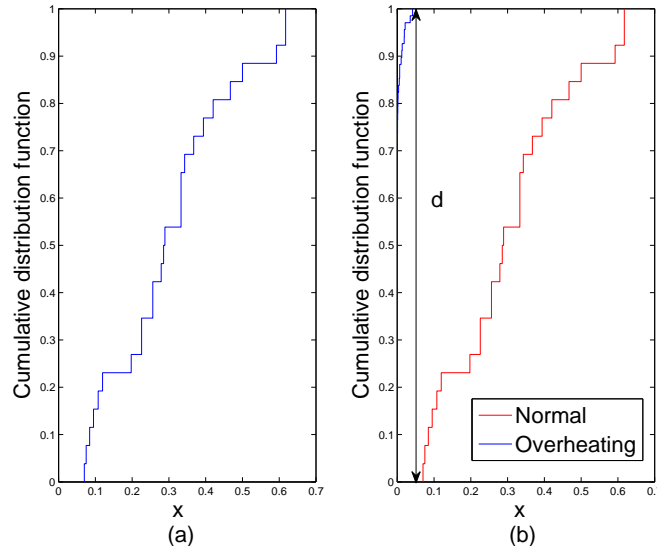


Figure 5.3: (a) CDF of  $\%C_2H_2$  in the normal case. (b) The K-S test of  $\%C_2H_2$  between normal and overheating.

### 5.3.2 $K$ -Nearest Neighbors Algorithm

$K$ -nearest neighbor (KNN) probably is one of those algorithms that are very simple to understand but works very well in practice [80] [81]. Also it is surprisingly

versatile and its applications range from vision to proteins to computational geometry to graphs and so on. The algorithm has been successfully applied in many different research areas. It also might surprise current researchers to know that KNN is one of the top data mining algorithms.

Generally, in KNN classification, the output is a class membership. An object is classified by a majority vote of its neighbors, with the object being assigned to the class most common among its  $K$  nearest neighbors [82]. KNN is an example of instance-based learning, in which the training data set is stored, so that a classification for a new unclassified record may be found simply by comparing it to the most similar records in the training set.

Therefore, two main issues involved in building a classifier using the k-nearest neighbor algorithm are: The definition of numbers of  $K$  neighbors should be applied. In other words, how to define  $K$ ?; The measurement of similarity between records and the trained ones. These two questions are answered in the following contents.

#### **Distance Measurement**

Data analysts define distance metrics to measure similarity. A distance metric or distance function is a real-valued function  $d$ , such that for any coordinates  $x$ ,  $y$ , and  $z$ :

1.  $d(x, y) \geq 0$ , and  $d(x, y) = 0$  only if  $x = y$ .
2.  $d(x, y) = d(y, x)$
3.  $d(x, z) \leq d(x, y) + d(y, z)$

Condition 1 assures us that distance is always nonnegative, and the only way for distance to be zero is for the coordinates to be the same. Condition 2 indicates commutativity, which means the distance from point  $x$  to point  $y$  is the same as the distance from point  $y$  to point  $x$ . Finally, Condition 3 represents the triangle inequality, which illustrates that introducing a third

point can never shorten the distance between two other points.

The most common distance function is Euclidean distance, which represents the usual manner in which humans think of distance in the real world:

$$d_{Euclidean}(x, y) = \sqrt{\sum_i (x_i - y_i)^2} \quad (5.3.2)$$

where  $x = [x_1, x_2, \dots, x_i]$ , and  $y = [y_1, y_2, \dots, y_i]$  represent  $i$  attribute values of the records.

When measuring distance, however, certain attributes that have large values, such as income, can overwhelm the influence of other attributes which are measured on a smaller scale, such as years of service. To avoid this, the data analyst should make sure to normalize the attribute values. For continuous variables, the min-max normalization or Z-score standardization can be applied:  $X^* = \frac{X - \min(X)}{\text{range}(X)} = \frac{X - \min(X)}{\text{Max}(X) - \text{Min}(X)}$  and  $X^* = \frac{X - \min(X)}{SD(X)}$ .

#### Determination of $K$ for KNN

A small value of  $k$  means that noise will have a higher influence on the result, which a large  $K$  value make it computationally expensive, which may calculate all the point in feature space. Typical a range of  $K$  is manually selected by the user. Normally, the value of  $K$  is from 10 to 50.

## 5.4 Experimental Results

In this research, 174 DGA samples and their matching diagnosis are taken IEC10 DGA database. The DGA data contain seven types of key gases and the corresponding diagnosis results from on-site inspections. The DGA samples are composed of four types, which are normal units (33 samples), overheating (68 samples), low energy discharge (25 samples) and high energy discharge (48 samples). The data are first preprocessed by using bootstrap to equalise the amount of data in each fault case. Subsequently, newly selected features and the conventional features are ranked by applying the K-S test. Then, the first three highly ranked features are applied as input vectors for a multi-layer SVM classifier, whose tuning parameters are obtained by using PSO. Eventually, the performance of this classifier with

the selected features is evaluated. Meanwhile, classifiers analysing various GP-extracted features are also provided for comparison purposes.

#### 5.4.1 Feature Prioritisation using K-S Test

A publicly available bootstrap toolbox is used in this research for solving the shortage of numbers of gas samples. Gas samples of certain fault, such as, high energy discharge fault, are hard to collect during transformer operation. Meanwhile, the gas sample acquisition process from insulation oil may exist measurement errors. By using bootstrap preprocessing, the noise corruption is overcome and the amount of data of each fault type are almost equalised, where the final value of  $N_{tr}$  and  $N_{ts}$  are set to 100 and 10 respectively. Finally, the amount of newly obtained training and testing samples with regard to different classes are enlarged as follows: normal (99 training samples — 13 testing samples), overheating (136 training samples — 15 testing samples), low energy discharge (85 training samples — 10 testing samples), high energy discharge (96 training samples — 11 testing samples).

Based on an in-depth analysis of current DGA standards, the five specifically selected features are:  $F_{S1} = \text{TCG}/542$ ,  $F_{S2} = \text{C}_2\text{H}_6/65$ ,  $F_{S3} = \log_2((\frac{\text{C}_2\text{H}_2}{\text{C}_2\text{H}_4})/0.1)$ ,  $F_{S4} = \log_2(\%\text{C}_2\text{H}_2/0.21)$ ,  $F_{S5} = \log_2(\%\text{C}_2\text{H}_4/0.23)$ . In the above features, TCG is the volume summation of  $\text{H}_2$ ,  $\text{CH}_4$ ,  $\text{C}_2\text{H}_2$  and  $\text{C}_2\text{H}_4$ . The relative proportions of gases are  $\%\text{C}_2\text{H}_2$ ,  $\%\text{C}_2\text{H}_4$ , which can be calculated as follows:  $\%\text{C}_2\text{H}_2 = 100x/(x+y+z)$ ,  $\%\text{C}_2\text{H}_4 = 100y/(x+y+z)$ , where  $x = \text{C}_2\text{H}_2$ ,  $y = \text{C}_2\text{H}_4$ ,  $z = \text{CH}_4$ . Apart from the above selected features, five conventional gas ratios employed in the feature prioritisation are:  $F_{C1} = \text{CH}_4/\text{H}_2$ ,  $F_{C2} = \text{C}_2\text{H}_2/\text{C}_2\text{H}_4$ ,  $F_{C3} = \text{C}_2\text{H}_2/\text{CH}_4$ ,  $F_{C4} = \text{C}_2\text{H}_6/\text{C}_2\text{H}_2$  and  $F_{C5} = \text{C}_2\text{H}_4/\text{C}_2\text{H}_6$ . The ranking orders are obtained from the analysis of maximum distance values by using the K-S test.

Table 5.2: Maximum D values for features without bootstrapping

Level	$F_{S1}$	$F_{S2}$	$F_{S3}$	$F_{S4}$	$F_{S5}$	$F_{C1}$	$F_{C2}$	$F_{C3}$	$F_{C4}$	$F_{C5}$
1	3.33	1.87	1.78	1.27	1.65	1.53	1.78	1.41	1.97	3.34
2	1.10	2.69	5.85	5.84	4.99	5.25	5.77	5.76	5.75	2.77
3	0.75	1.09	2.67	2.17	3.48	2.18	2.67	1.27	1.26	1.25

Table 5.3: Feature ranking using K-S test results without bootstrapping

Level	F <sub>S1</sub>	F <sub>S2</sub>	F <sub>S3</sub>	F <sub>S4</sub>	F <sub>S5</sub>	F <sub>C1</sub>	F <sub>C2</sub>	F <sub>C3</sub>	F <sub>C4</sub>	F <sub>C5</sub>
1	2	4	5	10	7	8	6	9	3	1
2	10	9	1	2	7	6	3	4	5	8
3	10	9	3	4	1	5	2	8	6	7

Table 5.2 lists the maximum  $D$  values of all different features using the K-S test at each classification level without applying bootstrap. Level one indicates the separation of abnormal cases from normal cases. Level two represents the classification between thermal fault cases and electrical discharge fault cases. Level three denotes the separation between high energy discharge cases and low energy discharge cases. As an input vector for SVM in the corresponding level, a feature with a larger  $D$  value is more suitable than the feature with small ones. Table 5.3 shows the corresponding ranking orders based on their maximum  $D$  values in Table 5.2. The ranking scales are from one to ten. One indicates that the feature is the most significant feature while ten indicates that the feature is the least significant feature.

Table 5.4 and Table 5.5 provide the maximum  $D$  values for features using bootstrap. The corresponding feature ranking orders are given in Table 5.5. Compared with feature values in Table 5.2, all the values in Table 5.4 are larger due to increased sample numbers after bootstrap. However, there is no noticeable variation in the orders of the first five features as shown in Table 5.5 and Table 5.3.

Table 5.4: Maximum  $D$  values for features with bootstrapping

Level	F <sub>S1</sub>	F <sub>S2</sub>	F <sub>S3</sub>	F <sub>S4</sub>	F <sub>S5</sub>	F <sub>C1</sub>	F <sub>C2</sub>	F <sub>C3</sub>	F <sub>C4</sub>	F <sub>C5</sub>
1	5.77	3.75	3.36	3.07	2.83	2.18	3.36	1.83	4.23	5.84
2	1.91	4.28	8.45	8.44	7.45	7.91	8.44	8.44	8.44	4.61
3	2.14	2.74	4.78	3.56	5.82	3.17	4.78	2.03	2.07	2.34

Among the ranking values in Table. 5.5,  $F_{C5}$ ,  $F_{S1}$  and  $F_{C4}$  are the first three features in level one for separating between normal and fault cases. The two manually selected features  $F_{S1}$ ,  $F_{S2}$  are ranked at the second position and the fourth position.

Table 5.5: Features ranking using K-S test results with bootstrapping

Level	F <sub>S1</sub>	F <sub>S2</sub>	F <sub>S3</sub>	F <sub>S4</sub>	F <sub>S5</sub>	F <sub>C1</sub>	F <sub>C2</sub>	F <sub>C3</sub>	F <sub>C4</sub>	F <sub>C5</sub>
1	2	4	5	7	8	9	6	10	3	1
2	10	9	1	2	7	6	3	4	5	8
3	8	6	3	4	1	5	2	10	9	7

It also indicates that the total amount of combustible gases increases under any fault conditions. It is noticed the maximum  $D$  values of  $F_{S1}$  and  $F_{C5}$  are almost equal. Among the ranking orders of level two for discriminating between thermal and discharge fault,  $F_{S3}$ ,  $F_{S4}$  and  $F_{C2}$  are the three most important features. Their maximum  $D$  values are almost equal with each other. Based on the results, it shows that  $C_2H_2/C_2H_4$  and  $C_2H_2\%$  are very important for the classification between overheating and discharge faults. Among the ranking orders of level three for the classification between low and high discharge faults,  $F_{S5}$ ,  $F_{C2}$  and  $F_{S3}$  are the three highly ranked features. In Duval's triangle, a clear boundary using  $C_2H_4\%$  is provided for classification of these two faults. The ranking results also shows that the selected features are all related to  $C_2H_4$ . In summary, the results illustrate that the newly selected features have a clear physical meaning.

### 5.4.2 Configuration of Intelligent classifiers

In this part, a briefly describes the configuration of The three AI data classification techniques, SVM, ANN and KNN classifiers. The first method has method has been introduce in the precede chapter while the last two is presented earlier in this chapter.

#### Artificial Neural Networks

As it has been discussed before, the most common structure of ANN for classification is multilayer perception (MLP) with a exappropriation learning algorithm. Therefore, in this research, a simple three-layer MLP structure with input, hidden and output layers is employed, where each neuron model of the hidden layer has a hyperbolic tangent activation function and a logistic

activation function is implemented for generation outputs.

### Support Vector Machine

The procedure of transformer fault diagnosis based on a multi-layer SVM classifier is illustrated in Fig. 5.4. Three layer SVMs are applied to identify the four classes: normal, overheating, low energy discharge and high energy discharge. It contains three procedures at each level, which are SVM training, SVM validation and SVM testing. The data used for the each level are corresponding to the selected features. The optimised parameters of SVM are obtained by PSO. The output label of SVM-1 is set to +1 if it belongs to the normal case; otherwise -1. All fault cases are classified into thermal faults and discharge faults by the second layer SVM-2. The output label of SVM-2 is set to +1 if it belongs to the thermal fault case; otherwise -1. SVM-3 is applied for the classification between low energy discharge data and high energy discharge data. The output label of SVM-3 is set to +1 if it is the low energy discharge case; otherwise -1.

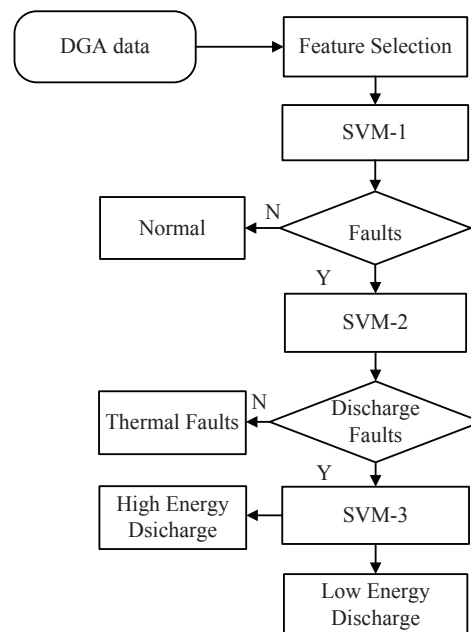


Figure 5.4: Diagnostic model using multi-layer SVM classifier



### K Nearest Neighbor

The value of  $K$  in KNN classifier is selected not to be a too small in order to minimise the noise effect in training data. On the other hand, a large value of  $K$  will increase the computing time as mentioned before. In this research, the value is selected between 10 to 60.

#### 5.4.3 Classification Results using the K-S Features

In this research, the ten-fold cross-validation has been employed to randomly separate DGA samples. Eight folds data are applied for the training purpose. One fold data is used for validation in PSO-SVM while the other data is applied for testing. By applying the division of the total accuracy by ten, which is repeating iterations, the classification accuracy is obtained. The two tuning parameters  $\xi$  and  $C$  of SVM are acquired through PSO training and validation. The swarm particle size is set as 30. The maximum iterations are 50. The values of  $c_1$  and  $c_2$  are both given as 2.0. The initialisation particle space for searching is between 0 and 100. Table 5.6 shows the average classification accuracy of each layer and the total average classification accuracy using the multi-layer PSO-SVM with different features. Five commonly used ratios as well as the Rogers ratios are also included for comparison purposes. As it can be seen from Table 5.6, the newly selected features achieve the highest overall classification accuracy 96.50%. Compared with the new features, the performances of multi-layer PSO-SVM are not satisfactory in both five common ratio features and the Rogers ratio features (86.71% and 87.09%). For separating abnormal cases from normal cases, the selected features  $F_{C5}$ ,  $F_{S1}$  and  $F_{C4}$  gain a very high classification accuracy 97.42%, which leads to an overall high total accuracy 96.50%. Comparatively, the first level classification accuracies using conventional features are lower values 90.82% and 89.32% respectively. This is the main reason that their total average accuracies are low. In the other two classification levels, the classification accuracies using conventional features are also lower than the accuracy applying selected features.

Table 5.6: Classification accuracy (%) using multi-layer PSO-SVM with different features

Features	Layer	$\xi$	$C$	Accuracy	Total average accuracy
$F_{C5} F_{S1} F_{C4}$	SVM-1	0.65	8.13	97.42	<b>96.50</b>
$F_{S3} F_{C2} F_{S4}$	SVM-2	0.04	27.40	99.37	
$F_{S5} F_{C2} F_{S3}$	SVM-3	0.83	14.60	98.50	
$F_{C1} F_{C2} F_{C3} F_{C4} F_{C5}$	SVM-1	0.92	9.70	90.82	86.71
$F_{C1} F_{C2} F_{C3} F_{C4} F_{C5}$	SVM-2	0.68	5.65	92.27	
$F_{C1} F_{C2} F_{C3} F_{C4} F_{C5}$	SVM-3	0.85	15.06	91.88	
$F_{C1} F_{C2} F_{C5}$	SVM-1	0.17	20.69	89.32	87.09
$F_{C1} F_{C2} F_{C5}$	SVM-2	0.66	2.32	94.32	
$F_{C1} F_{C2} F_{C5}$	SVM-3	0.39	10.09	92.70	

#### 5.4.4 Classification Results using GP Features

Table 5.7: Test classification accuracy(%) of GP-ANN with different neuron numbers

ANN	4 GP Features			6 GP Features			8 GP Features		
	mean	st.dev	best	mean	st.dev	best	mean	st.dev	best
3 neurons	71.78	1.42	74.60	76.75	7.67	<b>85.96</b>	75.09	1.89	77.63
4 neurons	72.13	2.89	75.44	71.94	2.45	75.44	74.47	6.80	<b>80.26</b>
5 neurons	71.88	2.71	74.75	75.09	2.60	78.51	69.56	2.30	71.50
6 neurons	69.21	5.22	<b>76.32</b>	73.34	5.65	<b>81.15</b>	71.48	4.08	78.07
10 neurons	63.25	5.22	68.42	66.41	3.18	70.18	60.89	3.43	63.56

For comparison purposes, ANN, KNN and SVM are applied to analyse the features extracted by genetic programming (GP). Table 5.7 shows the fault classification accuracy of the multilayered perceptron (MLP) with a backpropagation learning algorithm using different numbers (varying from 3 to 10) of neurons in the hidden layer. A 76.32% accuracy is obtained with four GP-extracted features, whereas

Table 5.8: Test classification accuracy (%) of PSO-SVM using GP features

SVM	4 GP Features				6 GP Features				8 GP Features			
	$\xi$	$C$	A1	A2	$\xi$	$C$	A1	A2	$\xi$	$C$	A1	A2
SVM-1	0.029	1.58	84.85	81.85	0.23	7.44	92.42	<b>88.16</b>	0.12	1.24	88.71	83.77
SVM-2	0.79	2.48	87.51		0.014	10.25	90.36		0.021	5.31	86.65	
SVM-3	0.39	8.41	90.13		1.21	1.37	89.01		0.003	4.17	87.12	

Table 5.9: Test classification accuracy (%) of GP-KNN with different neighbor number

KNN	4 GP Features	6 GP Features	8 GP Features
10	70.81	71.96	74.56
20	68.43	85.84	81.15
40	73.76	89.90	92.11
45	73.67	<b>92.12</b>	<b>92.12</b>
50	73.68	<b>92.12</b>	<b>92.12</b>
60	73.65	92.12	92.12

an application of the six GP-extracted features indicates an improved accuracy of 85.96%. In Table 5.8 , A1 indicates the classification accuracy of each level while A2 represents the overall accuracy, the maximum SVM classification performance at 88.16% is obtained with the six GP-extracted features. Its accuracy is higher than accuracy of conventional gas (86.71% and 87.09%). However, it is much lower than the classification accuracy using the proposed feature 96.50% in Table 5.6. It can be seen from Table 5.9, the KNN classification results are listed with respect to the neighbour number and the number of GP-extracted features. Six and eight GP-extracted features allows KNN to achieve the maximum value 92.12%, whereas the neighbour numbers equal to 45 and 50. The final results using GP feature

Table 5.10: Best test classification accuracy(%) of different classifiers

GP features	ANN	SVM	KNN
4 GP features	76.32	81.85	73.68
6 GP features	85.96	88.16	92.12
8 GP features	80.26	83.77	92.12

extraction method are illustrated in Table 5.10. The maximum SVM classification performance at 88.16% is obtained with six GP-extracted features. The highest ANN accuracy of 85.96% is reached using six GP-extracted features. However, one of ANN drawbacks is that overfitting makes the network tend to adopt particular details of specific training dataset, which may lead to a high training accuracy but a low test accuracy. The unitisation of the six and eight GP-extracted features allows KNN to achieve the maximum classification accuracy of 92.11%. Compared with application of GP features, the proposed features increase the classification accuracy of PSO-SVM from 88.16% to 96.50%. Moreover, it also has a higher value than the maximum classification accuracy 92.11% with KNN. The feature selection using GP only focuses on the mathematical characteristics of datasets. Unlike GP, the proposed feature extraction method not only considers the physical meaning of gases but also takes into account their statistical characteristics. The comparison of classification accuracy indicates that the proposed method can be applied for the

improvement of DGA accuracy.

## 5.5 Conclusion

In this chapter, both the physical meaning of fault gases and their statistical characteristics are considered for feature extraction. Firstly, five novel gas features are manually selected based on the in-depth analysis of well-known DGA international standards. Combined with conventional gas features, prioritisation of all features are obtained by using the K-S test. The features in the first three rankings are applied as input vectors for a multi-layer SVM classifier, whose tuning parameters are optimised by utilising PSO. Among all classification accuracies using different features, the proposed new features gain the highest accuracy. Moreover, a comparison of results illustrates that the proposed method has superiority over other artificial intelligence classifiers dealing with features extracted from GP.

# Chapter 6

## Conclusion and Future work

Literatures of DGA techniques have been successfully reviewed in Chapter 2, including the theory of fault gas evolution and a variety of conventional gas interpretation schemes. The advantages of DGA are : identifying the improper use of units; advanced warning of developing faults; convenient scheduling of repairs; status checks on new and repaired units and monitoring of units under overload. Based on different interpretation methods of DGA, the correlations among gas types, gas concentrations and fault types are summarised. Then, conventional DGA evaluation procedures are presented and a combined DGA criterion is introduced involving the Key gas method, the Rogers ratio method, the gassing rate method and the Duval triangle method.

In Chapter 3, DGA dataset cases, including lab simulated cases and fault cases identified by inspection of the equipments, are applied as testing dataset. A  $\pm 5\%$  variation is calculated and all these values are added to the original faulty gas value. The  $\pm 10\%$  variation is computed and all these values are added to those fault cases identified by the inspection of the equipment. Two important DGA methods, Duval triangle and IEC ratio method, are applied as classification methods. All the fault diagnosis results are obtained by using the variations. The corresponded final decisions are achieved by calculating the number of correct fault diagnosis result of each variation. Based on the analysis of the results, three zones are concluded in the original Duval triangle graphic for improving the performance of its application. The first one indicates a zone has a high possibility of misclassification of discharge

faults. The bushing related arcing faults and all tracking related faults have high tendency to be classified as high energy discharge. Arcing in low voltage windings and flash-over fault appear in the zone as a low energy discharge. The second zone represents a zone has a possible misclassification of overheating faults. In this zone, the case can be misclassified as a fault either greater than 700 °C or smaller than 700 °C. The third zone decreases the threshold value of %C<sub>2</sub>H<sub>4</sub> from 98% to 96% by carefully considering the partial discharge cases and their variations. All these cases are then classified by the IEC ratio method for comparison. Each diagnosis value obtained from the IEC ratio method is lower than the Duval triangle method and unknown cases are generated due to the lack of codes.

In chapter 4, three support vector based classifiers are developed to improve the classification accuracy. Two methods are applied for DGA data preprocessing. One is the resample tool bootstrap for overcoming the shortage of faulty data while the other one is the logarithmic transformation of DGA concentrations, which rescale the gas ratio to generate additional features. PSO presents a strong capability of searching the optimised combination of preset parameters for classifiers within a short convergence time. After the comparisons of final results, PSO-LSSVM presents a significantly high classification accuracy among all the discussed methods, while accuracy fluctuation of PSO-SVDD indicates that it is not appropriate for multi-classification after the bootstrap processing. Comparisons of the decision boundaries with data in 3D figures indicate that additional features can enhance LS-SVM classification performance.

In Chapter 5, both the physical meaning and the statistical characteristics of fault gases are considered for feature extraction. Firstly, five novel gas features are manually selected based on the in-depth analysis of well-known DGA international standards. Prioritisation of all features is obtained by using the K-S test. The features in the first three rankings are applied as input vectors for a multi-layer SVM classifier, whose tuning parameters are optimised by utilising PSO. Among all classification accuracies using different features, the proposed new features gain the highest accuracy. Moreover, a comparison of results illustrates that the proposed method has superiority over other artificial intelligence classifiers dealing

with features extracted from GP.

The fixed 5% and 10% variations are applied as sampling error rates in this research, which are based on the analysis of CIGRE accuracy surveys. Recent research shows the deviation between laboratory results and online monitoring DGA results is within 30%. So, other percentage values can be used to represent sampling error rates with regard to different gas concentration levels. On the other hand, a polygonal uncertainty region can be obtained around the gas data point in Duval Triangle graphic, if the estimate sampling error rate is considered. By treating the uncertainty region as a zone containing equal distribution data, a probability value can be generated to every diagnostic outcome.



# References

- [1] IEEE guide for the interpretation of gases generated in oil-immersed transformers. *IEEE Std C57.104-2008 (Revision of IEEE Std C57.104-1991)*, pages 1–36, Feb 2009.
- [2] S.J. Blanksby and G.B. Ellison. Bond dissociation energies of organic molecules. *Accounts of Chemical Research*, 36(4):255–263, Jan 2003.
- [3] S. Singh and M.N. Bandyopadhyay. Dissolved gas analysis technique for incipient fault diagnosis in power transformers: A bibliographic survey. *IEEE Electrical Insulation Magazine*, 26(6):41–46, Nov 2010.
- [4] M. Duval. A review of faults detectable by gas-in-oil analysis in transformers. *IEEE Electrical Insulation Magazine*, 18(3):8–17, May 2002.
- [5] M. Duval. The duval triangle for load tap changers, non-mineral oils and low temperature faults in transformers. *IEEE Electrical Insulation Magazine*, 24(6):22–29, Nov 2008.
- [6] Mineral oil-impregnated electrical equipment in service-guide to the interpretation of dissolved and free gases analysis. *IEC Publication 60599*, 1999.
- [7] N.A. Muhamad, B.T. Phung, T.R. Blackburn, and K.X. Lai. Comparative study and analysis of dga methods for transformer mineral oil. In *Proceedings of power technology meeting*, pages 45–50, July 2007.
- [8] M. Duval and J. Dukarm. Improving the reliability of transformer gas-in-oil diagnosis. *IEEE Electrical Insulation Magazine*, 21(4):21–27, Jul 2005.

- 
- [9] M. Duval and A. Depabla. Interpretation of gas-in-oil analysis using new IEC publication 60599 and IEC TC 10 databases. *IEEE Electrical Insulation Magazine*, 17(2):31–41, Mar 2001.
- [10] S. Birlasekaran and G. Ledwich. *Asset management of power apparatus*. Springer London, 2 edition, 2006.
- [11] J.H. Harlow. *Electric power transformer engineering*. CRC Press, 3 edition, 2012.
- [12] Guide for the dissolved gas analysis and analysis. Technical report, Chinese standards boards, China, 1987.
- [13] Loading guide for oil-immersed power transformers. Technical report, International Electrotechnical Commission, 1991.
- [14] Loading guide for dry-type power transformers. Technical report, International Electrotechnical Commission, 2007.
- [15] High voltage test techniques - partial discharge measurements. Technical report, International Electrotechnical Commission, 2000.
- [16] Z.D. Wang, X. Yi, S.T. Li, J. V. Hinshaw, and J. Noakes. Comparison between online and laboratory measurements of fault gases for mineral oil and natural ester. *International Journal on Electrical Engineering and Informatics*, 5(2):173–180, Jun 2013.
- [17] Q. Su, C. Mi, L.L. Lai, and P. Austin. A fuzzy dissolved gas analysis method for the diagnosis of multiple incipient faults in a transformer. *IEEE Transactions on Power Systems*, 15(2):593–598, May 2000.
- [18] P.S. Georgilakis, J.A. Katsigiannis, K.P. Valavanis, and A.T. Souflaris. A systematic stochastic petri net based methodology for transformer fault diagnosis and repair actions. *Journal of Intelligent and Robotic Systems*, 45(2):181–201, Feb 2006.
-

- 
- [19] R.J. Liao, J.P. Bian, L.J. Yang, S. Grzybowski, Y.Y. Wang, and J. Li. Forecasting dissolved gases content in power transformer oil based on weakening buffer operator and least square support vector machine-markov. *IET Generation, Transmission and Distribution*, 6(2):142–151, Feb 2012.
- [20] W.H. Tang, S. Almas, and Q.H. Wu. Transformer dissolved gas analysis using least square support vector machine and bootstrap. In *Proceedings of the 26th Chinese Control Conference*, pages 482–486, Jul 2007.
- [21] Z.Y. Wang, Y.L. Liu, and P.J. Griffin. A combined ANN and expert system tool for transformer fault diagnosis. In *IEEE Power Engineering Society Winter Meeting*, pages 339–347, 1999.
- [22] R.R. Rogers. IEEE and IEC codes to interpret incipient faults in transformers, using gas in oil analysis. *IEEE Transactions on Electrical Insulation*, 13(5):349–354, Oct 1978.
- [23] E. Dornenburg and W. Strittmatter. Monitoring oil-cooled transformers by gas analysis. *Brown Boveri Review*, 61(5):238–247, 1974.
- [24] R. Batruni, R.C. Degeneff, and M.A. Lebow. Determining the effect of thermal loading on the remaining useful life of a power transformer from its impedance versus frequency characteristic. *IEEE Transactions on Power Delivery*, 11(3):1385–1390, Jul 1996.
- [25] C.R.T. Castro, S.R. Barbosa, H.L. Ferreira, L.E. Samico, I.J.S. Lopes, and S.R. Silva. Power transformer loading studies considering overexcitation. In *Transmission and Distribution Conference and Exposition*, pages 651–656, Nov 2004.
- [26] K.T. Muthanna, A. Sarkar, K. Das, and K. Waldner. Transformer insulation life assessment. *IEEE Transactions on Power Delivery*, 21(1):150–156, Jan 2006.
- [27] H. Martin. *The J and P Transformer Book*. Newnes, 2011.
-

- 
- [28] A. Shahsiah, R.C. Degeneff, and J.K. Nelson. A study of the temperature-based dynamic nature of characteristic gases in oil-cellulose insulation systems. *IEEE Transactions on Dielectrics and Electrical Insulation*, 14(2):471–479, Apr 2007.
- [29] A. Akbari, S. Dehpahlevan, and H. Borsi. Analyzing dynamic of moisture equilibrium in oil-paper insulation in power transformers for efficient drying. In *IEEE Conference on Electrical Insulation and Dielectric Phenomena*, pages 545–548, Oct 2006.
- [30] R.J. Musil, E. Schopper, and H. Foschum. Behavior of transformer insulation under short-time overvoltage. *IEEE Transactions on Power Apparatus and Systems*, 96(2):614–618, Mar 1977.
- [31] E.L. Morrison. Evaluation of the thermal stability of electrical insulating paper. *IEEE Transactions on Electrical Insulation*, EI-3(3):76–82, Aug 1968.
- [32] Facilities instructions, standards and techniques in transformer diagnostics, 2003. Technical report, Bureau of Reclamation Hydroelectric Research and Technical Services Group, Denver, 2003.
- [33] P.J. Griffin, R.L. Lewand, R.C. Peck, and N.A. Letendre. Load tap changer diagnostics using oil tests - A key to condition-based maintenance. In *Conference on Minutes of Doble Engineering*, 2005.
- [34] M. Duval et al. Final report of CIGRE TF D1-01-15. In *Conference on Electrical Insulation and Dielectric Phenomena, Annual Report*, 1990.
- [35] C.P. Mcshane, J. Corkran, K. Rapp, and J. Luksich. Natural ester dielectric fluid development update. In *IEEE Power Energy Society General Meeting*, pages 1–6, Jul 2009.
- [36] C.P. McShane, J. Luksich, and K.J. Rapp. Retrofilling aging transformers with natural ester based dielectric coolant for safety and life extension. In *Cement Industry Technical Conference*, pages 141–147, May 2003.
-

- 
- [37] C. Perrier and A. Beroual. Experimental investigations on insulating liquids for power transformers: Mineral, ester, and silicone oils. *IEEE Electrical Insulation Magazine*, 25(6):6–13, Nov 2009.
- [38] Copper power system, Envirmtemp FR3 Fluid - Dissolved Gas Guide. Technical report, R900-20-19, 2006.
- [39] P.J. Griffin. Analysis for combustible gases in transformer silicone fluids. In *Minutes of the 52th Annual International Conference of Doble Clients*, 1987.
- [40] S. Tenbohlen, M. Schafer, Z.D. Wang, and I.H. Atanasova. Investigation on sampling, measurement and interpretation of gas-in-oil analysis for power transformers. In *CIGRE, Paris, A2-102*, 2008.
- [41] Guide for the analysis and diagnosis of gases dissolved in transformer oil. Technical report, National Technical Committee 44 on Transformer of Standardization Administration of China., Bureau of Standards for the P.R.China GB7252-87, 2003.
- [42] Z.D. Wang, A. Darwin, and R. Martin. New insulation fluids: use of environmentally friendly fluids in power transformers,. In *CIGRE Colloquium, Bruges, Belgium*, pages PS1–4, 2007.
- [43] M. Tozzi, A. Cavallini, G.C. Montanari, and G.L.G. Burbui. PD detection in extruded power cables: an approximate propagation model. *IEEE Transactions on Dielectrics and Electrical Insulation*, 15(3):832–840, Jun 2008.
- [44] N. Oussalah, Y. Zebboudj, and S.A. Boggs. Partial discharge pulse propagation in shielded power cable and implications for detection sensitivity. *IEEE Electrical Insulation Magazine*, 23(6):5–10, Nov 2007.
- [45] G. Berg and L.E. Lundgaard. PD signatures of wedge type discharges in transformer insulation. In *IEEE 14th International Conference on Dielectric Liquids*, pages 211–214, 2002.
-

- 
- [46] R. H. Lee. The other electrical hazard: electric arc blast burns. *IEEE Transactions on Industry Applications*, IA-18(3):246–251, May 1982.
- [47] T.M. Crnko. Flash hazard and design considerations for its reduction. In *Industry Applications Conference Fourtieth IAS Annual Meeting*, volume 3, pages 1928–1937, Oct 2005.
- [48] S. Abdi, A. Boubakeur, A. Haddad, and N. Harid. Influence of artificial thermal aging on transformer oil properties. *Electric Power Components and Systems*, 39(15):1701–1711, Oct 2011.
- [49] H.Z. Ding, R. Heywood, J. Lapworth, and S. Ryder. Learning from success and failure in transformer fault gas analysis and interpretation. In *IET Conference on Reliability of Transmission and Distribution Networks*, pages 1–6, Nov 2011.
- [50] B. Bhalja and R.P. Maheshwari. Wavelet-based fault classification scheme for a transmission line using a support vector machine. *Electric Power Components and Systems*, 36(10):1017–1030, Sep 2008.
- [51] D.M.J. Tax and R.P.W. Duin. Support vector data description. *Machine Learning*, 54(1):45–66, Jan 2004.
- [52] H.B. Zheng, R.J. Liao, S. Grzybowski, and L.J. Yang. Fault diagnosis of power transformers using multi-class least square support vector machines classifiers with particle swarm optimisation. *IET Electric Power Applications*, 5(9):691–696, Nov 2011.
- [53] A. Shintemirov, W.H. Tang, and Q.H. Wu. Power transformer fault classification based on dissolved gas analysis by implementing bootstrap and genetic programming. *IEEE Transactions on Systems, Man, and Cybernetics, Part C: Applications and Reviews*, 39(1):69–79, Jan 2009.
- [54] P. Mirowski and Y. Lecun. Statistical machine learning and dissolved gas analysis: A review. *IEEE Transactions on Power Delivery*, 27(4):1791–1799, Oct 2012.
-

- 
- [55] B. Efron. The bootstrap and modern statistics. *Journal of the American Statistical Association*, 95(452):1293–1296, Dec 2000.
- [56] A.M. Zoubir and I.D. Robert. Bootstrap methods and applications. *IEEE Signal Processing Magazine*, 24(4):10–19, Jul 2007.
- [57] V.N. Vapnik. An overview of tatistical learning theory. *IEEE Transactions on Neural Networks*, 10(5):988–999, Sep 1999.
- [58] J.A.K. Suykens, T.V. Gestel, J.D. Brabanter, B.D. Moor, and J. Vandewalle. *Least Squares Support Vector Machines*. World Scientific, Nov 2002.
- [59] D.M.J. Tax and R.P.W. Duin. Support vector domain description. *Pattern Recognition Letters*, 20:1191–1199, Sep 1999.
- [60] C. Cortes and V. Vapnik. Support-vector networks. *Machine Learning*, 20(3):273–297, Sep 1995.
- [61] J.C. Platt, N. Cristianini, and T.J. Shawe. Large margin DAGs for multiclass classification. In *Advances in Neural Information Processing Systems*, pages 547–553. MIT Press, 2000.
- [62] R. Fletcher. *Practical methods of optimization*. Wiley-Blackwell, Chichester; New York, 2 edition, 2000.
- [63] Y.H. Shi and R. Eberhart. A modified particle swarm optimizer. In *Evolutionary Computation Proceedings, IEEE International Conference on Computational Intelligence.*, pages 69–73, May 1998.
- [64] M.R. Alrashidi and M.E. Elhawary. A survey of particle swarm optimization applications in electric power systems. *IEEE Transactions on Evolutionary Computation*, 13(4):913–918, Aug 2009.
- [65] J.L. Guardado, J.L. Naredo, P. Moreno, and C.R. Fuerte. A comparative study of neural network efficiency in power transformers diagnosis using dissolved gas analysis. *IEEE Transactions on Power Delivery*, 16(4):643–647, Oct 2001.
-

- 
- [66] M. Dong, D.K. Xu, M.H. Li, and Z. Yan. Fault diagnosis model for power transformer based on statistical learning theory and dissolved gas analysis. In *IEEE International Symposium on Electrical Insulation*, pages 85–88, Sep 2004.
- [67] R.J. Liao, H.B. Zheng, S. Grzybowski, L.J. Yang, C. Tang, and Y.Y. Zhang. Fuzzy information granulated particle swarm optimisation-support vector machine regression for the trend forecasting of dissolved gases in oil-filled transformers. *IET Electric Power Applications*, 5(2):230–237, Feb 2011.
- [68] D.R. Morais and J.G. Rolim. A hybrid tool for detection of incipient faults in transformers based on the dissolved gas analysis of insulating oil. *IEEE Transactions on Power Delivery*, 21(2):673–680, Apr 2006.
- [69] R. Karthik, T. Sree Renga Raja, and M.W. Iruthayarajan. Investigations of furanic derivatives in transformer oil using ultra-violet light absorption property. *IET Electric Power Applications*, 7(2):123–130, Feb 2013.
- [70] L.L. Lai, A.G. Sichanie, and J. Gwyn. Comparison between evolutionary programming and a genetic algorithm for fault-section estimation. *IEE Proceedings Generation, Transmission and Distribution*, 145(5):616–620, Sep 1998.
- [71] A. Shintemirov, W. Tang, and Q.H. Wu. Power transformer fault classification based on dissolved gas analysis by implementing bootstrap and genetic programming. *IEEE Transactions on Systems, Man, and Cybernetics, Part C: Applications and Reviews*, 39(1):69–79, Jan 2009.
- [72] G.W. Zhang, X.D. Wang, Y.C. Liang, and J. Liu. Fast and robust spectrum sensing via kolmogorov-smirnov test. *IEEE Transactions on Communications*, 58(12):3410–3416, Dec 2010.
- [73] K. Arshad and K. Moessner. Robust spectrum sensing based on statistical tests. *IET Communications*, 7(9):808–817, Jun 2013.
-



- 
- [74] A. Ivanov and G. Riccardi. Kolmogorov-Smirnov test for feature selection in emotion recognition from speech. In *IEEE International Conference on Acoustics, Speech and Signal Processing*, pages 5125–5128, Mar 2012.
- [75] H. Han, H.J. Wang, and X.C. Dong. Transformer fault dignosis based on feature selection and parameter optimization. *Energy Procedia*, 12(1):662 – 668, 2011.
- [76] B. Efron and R.J. Tibshirani. *An introduction to the Bootstrap*. CRC Press, 1994.
- [77] G. Marsaglia, W.W. Tsang, and J.B. Wang. Evaluating kolmogorov’s distribution. *Journal of Statistical Software*, 8(18):1–4, May 2003.
- [78] R. Simard and L.E. Pierre. Computing the two-sided kolmogorov-smirnov distribution. *Journal of Statistical Software*, 39(11):1–14, Mar 2011.
- [79] H.J. Eghbali. K-S test for detecting changes from landsat imagery data. *IEEE Transactions on Systems, Man and Cybernetics*, 9(1):17–23, Jan 1979.
- [80] Y. Cui, H. Ma, and T. Saha. Improvement of power transformer insulation diagnosis using oil characteristics data preprocessed by smoteboost technique. *IEEE Transactions on Dielectrics and Electrical Insulation*, 21(5):2363–2373, Oct 2014.
- [81] Z.S. Li, G.F Ding, R. Li, and S.F Qin. A new extracting algorithm of k nearest neighbors searching for point clouds. *Pattern Recognition Letters*, 49(1):162–170, Nov 2014.
- [82] F. Angiulli and G. Folino. Distributed nearest neighbor-based condensation of very large data sets. *IEEE Transactions on Knowledge and Data Engineering*, 19(12):1593–1606, Dec 2007.
-

## Appendix A

An approach for the detection of broken bars in an induction motor is introduced. The stator and rotor can be represented by a number of coupled electrical circuits using a multiple coupled circuit model. All self-inductance and mutual inductance are calculated based on winding function theory. By applying genetic algorithm (GA), optimized parameters are obtained by minimizing the errors between experimental results and simulation results. The experimental results are obtained from a published paper. The comparison result of speed and current illustrates a good agreement between the model and the induction motor in a healthy condition. Based on the optimized model, the simulation results of the machine with one broken bar and two adjacent broken bars are provided for fault diagnosis. By analyzing the power spectrum density of the stator current, the broken bars are detected by the clear and strong side frequency components. For the purpose of maintenance cost reduction of induction motor, researchers attempt to find efficient and reliable methods for the detection of faults. Broken rotor bar fault is one of typical rotor faults in an induction motor. It can bend out of the rotor slots by the effect of electromagnetic forces and rub the inner face of the stator, which may cause a mixed stator and rotor fault. In the past few decades, various techniques have been developed to detect rotor faults. One of the well-known methods for the detection of broken bar is the motor current signature analysis (MCSA), which is based on the monitoring of the stator phase current to detect sidebands around the supply frequency [1] [2]. More specifically, broken rotor bars result in current components being induced in the stator winding at the frequencies of  $2(1 \pm ks)f_s$ , where  $f_s$  is the supply frequency,  $s$  is the slip rate and  $k$  is an integer ( $k = 1, 2, 3, \dots$ ).

Calculation of the slip rate depends mainly on the mathematical model of the induction motor and its parameters during simulation. The classical  $d$ - $q$  model assumes that both stator and rotor windings are symmetric and the magnetomotive force (MMF) is sinusoidally distributed [3]. However, it cannot provide any information about rotor bars and end rings currents. And, it also requires a modification in the model structure for each fault case. Other methods are employed in the simulation based on the model of individual conductors in the rotor cage

using  $R$ - $L$  series circuits. The current loops are defined by two adjacent rotor bars connected by portions of the end ring. For a squirrel cage machine with  $n$  bars, the model leads to a transient model with a total of  $n + 3$  coupled simultaneous differential equations [4]. However, there are always errors between simulation results of model and experimental results of motor. These errors are due to the assumptions, e.g., saturation is neglected and air gap is uniform. On the other hand, the task of acquiring machine design data is very difficult and the values of parameters may vary because of temperature variations and the nonlinearities caused by the skin effect and saturation.

Parameter determination of induction motor with the deep bar effect was discussed in [5]. An approach to identifying the parameters of an induction machine from standstill time-domain test data was proposed in [6]. A standstill frequency test was utilized in [7] for motor parameter estimation. Another method [8] employed single-phase test results as a base test for calculating the equivalent circuit parameters. However, the conventional techniques applied to electrical machines require the measurement of full state variables and probing signals to excite dynamic modes of the machine for the identification purpose. Recently, evolutionary computation techniques provide more powerful means to resolve the problem. Effective identification of induction motor based on GA was proposed in [9] and [10]. But the research is based on the per-unit system with only limited parameters.

This study is to provide a solution based on a GA algorithm to acquire the best possible set of parameter values for the multiple circuit model, by means of minimizing the errors between the model's simulated results and the measured ones. The inductances of the proposed model are calculated by the winding function method. The parameters of this model, e.g., rotor bar resistance, end ring segment resistance are optimized using GA. Based on the accurate model, the simulations of machine with one broken bar and two broken bars are provided. The broken bar is detected by analyzing spectrum side components of the stator current in the frequency domain. The adverse effect of broken bars on the performance of motor are also discussed.

In this part, multiple coupled circuit modeling is presented at first. Then, winding function theory is discussed for the calculation of applied inductance. Finally, a brief introduction is given to genetic algorithms. The parameters of this model, for instance rotor bar resistance, end ring segment resistance are optimized by using the proposed GA. The motor current signature analysis (MCSA) is applied and the broken bar is determined by analyzing spectrum side frequency components of the stator current in the simulation.

### Appendix A.1 Multiple Coupled Circuit Modeling

The rotor and the stator can be represented by multiple inductive circuits using the coupled magnetic-circuit theory [11]. The current of each circuit is considered as an independent variable. Current and voltage relationships between stator and rotor can be described in a vector-matrix form as following equations:

$$V_s = R_s I_s + \frac{d\psi_s}{dt} \quad (\text{Appendix A.1})$$

$$V_r = R_r I_r + \frac{d\psi_r}{dt} \quad (\text{Appendix A.2})$$

$$\psi_s = L_{ss} I_s + L_{sr} I_r \quad (\text{Appendix A.3})$$

$$\psi_r = L_{rs} I_s + L_{rr} I_r \quad (\text{Appendix A.4})$$

where  $V_s$ ,  $V_r$ ,  $I_s$  and  $I_r$  are the stator voltage vector, rotor loop voltage vector, stator current vector and rotor loop current vector, which are given by equation (Appendix A.5), equation (Appendix A.6), equation (Appendix A.7) and equation (Appendix A.8) respectively. In equation (Appendix A.3) and equation (Appendix A.4),  $\psi_s$ ,  $\psi_r$  are the stator flux linkage vector and rotor flux linkage vector, which are given by equation (Appendix A.10) and equation (Appendix A.11). Because  $n$  identical and equally spaced bars are combined together by an end ring, the rotor flux linkage vector contains  $n$  flux linkage vectors and an end ring flux linkage vector. The current distribution of each rotor loop is illustrated by Figure. A.1, where  $L_b$ ,  $L_e$ ,  $R_b$  and  $R_e$  are the rotor bar leakage inductance, end-ring leakage inductance, rotor bar resistance and end-ring leakage resistance respectively. Each loop shares two rotor bars with two adjacent loops, where  $i_n^r$  is the  $n$ th rotor-loop

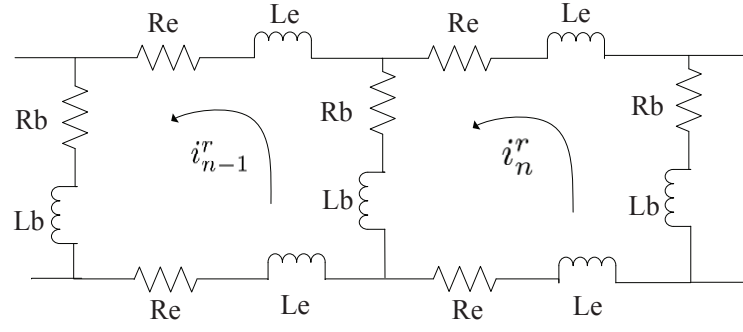


Figure A.1: Multiple coupled circuit rotor model

current. Among the following equations,  $v_e$  is the end-ring loop voltage,  $i_e$  is the end ring circulating current,  $R_s$  is stator resistance matrix and T indicates the transpose operation of a vector respectively.

$$V_s = [v_a^s \ v_b^s \ v_c^s]^T \quad (\text{Appendix A.5})$$

$$V_r = \begin{bmatrix} v_1^r & v_2^r & \cdots & v_n^r & v_e \end{bmatrix}^T \quad (\text{Appendix A.6})$$

$$I_s = \begin{bmatrix} i_a^s & i_b^s & i_c^s \end{bmatrix}^T \quad (\text{Appendix A.7})$$

$$I_r = \begin{bmatrix} i_1^r & i_2^r & \cdots & i_n^r & i_e \end{bmatrix}^T \quad (\text{Appendix A.8})$$

$$R_s = \begin{bmatrix} R_{aa} & 0 & 0 \\ 0 & R_{bb} & 0 \\ 0 & 0 & R_{cc} \end{bmatrix} \quad (\text{Appendix A.9})$$

$$\psi_s = [\psi_a^s \ \psi_b^s \ \psi_c^s] \quad (\text{Appendix A.10})$$

$$\psi_r = [\psi_1^r \ \psi_2^r \ \psi_3^r \ \cdots \ \psi_n^r \ \psi_e] \quad (\text{Appendix A.11})$$

Ideally, the resistances of the stator are equal with respect to each other. By comparing with the stator resistance matrix  $R_s$ , the complex rotor matrix  $R_r$  is a

matrix, whose size is equal to the numbers of bars.

$$R_r = \begin{bmatrix} R_m & \cdots & -R_b & R_e \\ -R_b & \cdots & 0 & R_e \\ \vdots & \vdots & \vdots & \vdots \\ 0 & R_m & -R_b & R_e \\ -R_b & -R_b & R_m & R_e \\ R_e & \cdots & \cdots & nR_e \end{bmatrix} \quad (\text{Appendix A.12})$$

$R_b$  is the rotor bar resistance,  $R_e$  is the end-ring-segment resistance and  $R_m$  is equal to  $2(R_b + R_e)$ . In equation (Appendix A.3) and equation (Appendix A.4),  $L_{ss}$ ,  $L_{rr}$  and  $L_{sr}$  are the inductance matrix of stator, rotor loop mutual inductance matrix and mutual inductance matrix between the stator and the rotor loop respectively. The matrix  $L_{rs}$ , which is the mutual inductance between the rotor loop and the stator, is equal to the transpose value of  $L_{sr}$  as shown in equation (Appendix A.14).  $L_{an}^{sr}$  is the mutual inductance between phase A and the  $n$ th rotor loop, while  $L_{ae}^{sr}$  is the mutual inductance between phase A and an end ring. The mutual inductances between phase B and rotor loops are also defined in the same way.

$$L_{ss} = \begin{bmatrix} L_m^s & L_{ab}^s & L_{ac}^s \\ L_{ba}^s & L_m^s & L_{bc}^s \\ L_{ca}^s & L_{cb}^s & L_m^s \end{bmatrix} \quad (\text{Appendix A.13})$$

$$L_{sr} = \begin{bmatrix} L_{a1}^{sr} & L_{a2}^{sr} & \cdots & L_{an}^{sr} & L_{ae}^{sr} \\ L_{b1}^{sr} & L_{b2}^{sr} & \cdots & L_{bn}^{sr} & L_{be}^{sr} \\ L_{c1}^{sr} & L_{c2}^{sr} & \cdots & L_{cn}^{sr} & L_{ce}^{sr} \end{bmatrix} \quad (\text{Appendix A.14})$$

$$L_{rr} = \begin{bmatrix} L_{mlp}^r & \cdots & L_{r_1 r_n}^r & L_e \\ L_{r_2 r_1}^r & \cdots & L_{r_1 r_n}^r & L_e \\ \vdots & \vdots & \vdots & \vdots \\ L_{r_{n-1} r_1}^r & \cdots & L_{r_{n-1} r_n}^r & L_e \\ L_{r_n r_1}^r & \cdots & L_{mlp}^r & L_e \\ L_e & \cdots & \cdots & nL_e \end{bmatrix} \quad (\text{Appendix A.15})$$

The rotor loop mutual inductance matrix  $L_{rr}$  is very complex, where  $L_{r_{n-1} r_n}^r$  indicates the mutual inductance between the  $(n - 1)$ th rotor loop and the  $n$ th rotor

loop. It equals to the result of  $M_{rr} - L_b$ .  $M_{rr}$  is the magnetizing inductance between two rotor loops and  $L_b$  is the bar linkage inductance.  $L_{mlp}^r$  is the total inductance of each loop. It equals to the result of  $L_{rm} + 2(L_b + L_e)$ .  $L_{rm}$  is the magnetizing inductance of each rotor loop.  $M_{rr}$  and  $L_{rm}$  are calculated by the winding function method. The mechanical-motion equation depends on the characteristics of load conditions. The torque, which opposes that produced by the machine, consists of an inertial torque, an internal-friction torque and an external load torque.

$$T_e = \frac{d\omega}{d\theta} \quad (\text{Appendix A.16})$$

$$T_e - T_L = J \frac{d\omega}{dt} \quad (\text{Appendix A.17})$$

$$\omega = \frac{d\theta}{dt} \quad (\text{Appendix A.18})$$

$$W_c = \frac{1}{2} I^T \frac{dL}{d\theta} I \quad (\text{Appendix A.19})$$

$T_e$  is the electromagnetic torque of machine,  $\theta$  is the mechanical angle,  $T_L$  is the load torque,  $J$  is inertia of the rotor and  $\omega$  is the mechanical angle speed respectively.  $W_c$  is magnetic co-energy.  $I$  is a combination vector, which includes  $I_r$  and  $I_s$ .  $L$  is composed by  $L_{sr}$ ,  $L_{rs}$ ,  $L_{rr}$  and  $L_{ss}$  matrixes.

## Appendix A.2 Winding Function Method

The inductances in equation (Appendix A.13), equation (Appendix A.14) and equation (Appendix A.15) can be calculated by the winding function method. The mutual inductance of two circuits describes the voltage induced in one electrical circuit by the rate of change of current in the other circuit. The general expression for mutual inductance between any two circuits is given by the following equation [12]:

$$L_{mn}(\theta) = \mu_0 l \int_0^{2\pi} \frac{r(\phi, \theta) N_m(\phi, \theta) N_n(\phi, \theta)}{g(\phi, \theta)} d\phi \quad (\text{Appendix A.20})$$

$\theta$  is the angular position of rotor with respect to some stator reference,  $\phi$  is a particular angular position along the stator inner surface,  $l$  is the length of the stack,  $r(\phi, \theta)$  is the average radius of air-gap,  $g(\phi, \theta)$  is the air gap function and  $\mu_0$  is the

permeability constant. The stator winding distribution of phase A can be denoted by a cosine function. Taking as a reference the magnetic axis of the first phase, the normalized stator winding function for this phase is:

$$N_{sa} = N_s/2 \cos(\phi) \quad (\text{Appendix A.21})$$

where  $N_s$  is the effective number of turns. The other two phases are also in the similar formula only with a phase shift.

$$N_b(\phi) = \left(\frac{N_s}{2}\right) \cos\left(\phi - \frac{2\pi}{3}\right) \quad (\text{Appendix A.22})$$

$$N_c(\phi) = \left(\frac{N_s}{2}\right) \cos\left(\phi + \frac{2\pi}{3}\right) \quad (\text{Appendix A.23})$$

Substituting equation (Appendix A.21) into equation (Appendix A.20), the magnetizing inductance for each stator coil is:

$$L_{sm} = \mu_0 l r N_s^2 \pi / 4g \quad (\text{Appendix A.24})$$

The total inductance of stator coil is the sum of magnetizing inductance  $L_{sm}$  and leakage inductance  $L_l$ .

$$L_m^s = L_{sm} + L_l \quad (\text{Appendix A.25})$$

The mutual inductances between different phases are:

$$L_{ba}^s = L_{ab}^s = L_{ac}^s = L_{ca}^s = L_{bc}^s = L_{cb}^s = -1/2 L_{sm} \quad (\text{Appendix A.26})$$

The winding function for the rotor loop is shown in Figure. A.2. The following piecewise function indicates the winding function value in a given rotor angle.

$$N_{rk}(\theta_r, \phi) = \begin{cases} -(a_r/2\pi), 0 < \phi < \theta_i \\ 1 - (a_r/2\pi), \theta_i < \phi < \theta_{i+1} \\ -(a_r/2\pi), \theta_{i+1} < \phi < 2\pi \end{cases} \quad (\text{Appendix A.27})$$



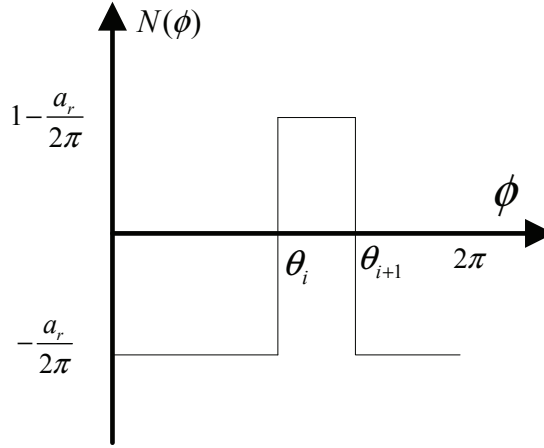


Figure A.2: Winding distribution of a rotor loop

$N_{rk}$  is the  $k$ th loop winding function and  $a_r$  is the radius of each rotor loop. It is equal to  $2\pi/N$ , where  $N$  is the total number of bars in a rotor. By substituting equation (Appendix A.27) into equation (Appendix A.20), the magnetizing inductance of each rotor loop  $L_{rm}$  and the mutual inductance  $M_{rr}$  between them are obtained respectively.

$$L_{rm} = \frac{\mu_0 l r a_r}{g} \left(1 - \frac{a_r}{2\pi}\right) \quad (\text{Appendix A.28})$$

The mutual inductance between different loops is:

$$M_{rr} = \frac{\mu_0 l r}{g} \left(-\frac{a_r^2}{2\pi}\right) \quad (\text{Appendix A.29})$$

The mutual inductance between the  $m$ th stator coil and the  $n$ th loop are denoted as:

$$M_{snrm} = \frac{\mu_0 l r}{g} N_s \cos\left(\theta_r + \frac{(2n-1)a_r}{2} - (m-1)\frac{2\pi}{3}\right) \sin\left(\frac{a_r}{2}\right) \quad (\text{Appendix A.30})$$

The inductances in equation (Appendix A.14) are:

$$M_{s1rn} = L_{an}^{sr}; M_{s2rn} = L_{bn}^{sr}; M_{s3rn} = L_{cn}^{sr} \quad (\text{Appendix A.31})$$

The calculation of inductance under broken bar faults can be also achieved by using this method. Consider a motor with  $N_b$  adjacent rotor bars, the gap between  $\theta_i$  and

$\theta_{i+1}$  in Figure. A.2 is enlarged. For this loop, the self-inductance can be calculated by the following expression:

$$L_{rb} = \frac{\mu_0 l r a_r}{g} ((N_b + 1) - (2N_b + 1) \frac{a_r}{2\pi}) \quad (\text{Appendix A.32})$$

The mutual inductance between this broken bar loop and all other healthy loops can be calculated by:

$$M_{rb} = \frac{\mu_0 l r}{g} (-\frac{a_r^2}{2\pi})(N_b + 1) \quad (\text{Appendix A.33})$$

The mutual inductance between the  $m$ th stator coil and the broken rotor loop are defined as:

$$M_{smrb} = \frac{\mu_0 l r}{g} N_s \cos(\theta_r + \frac{(2n+N_b-1)a_r}{2} - (m-1)\frac{2\pi}{3}) \sin((N_b + 1) \frac{a_r}{2\pi}) \quad (\text{Appendix A.34})$$

### Appendix A.3 Genetic Algorithms

GA is an optimization method inspired by natural genetics and biological evolution, which has been applied for dynamic model identification in multi-machine power systems [13]. For searching optimized solutions, it evaluates the objective function at problem solution domain iteratively. The strength of solution points is measured using fitness values, which depends only on the value of the objective function. The better points are retained in the population and recombined with other good performance to produce offspring. Gradually the points in the population approach the global extremum. Genetic algorithms can be applied when no information is available about the gradient of the objective function at selected points. The optimized function does not need to be continuous or differentiable. It can still achieve good results even in the cases that the function has several local minima values. Compared to the pure local optimization methods, e.g., gradient descent method, GA has the advantage that it does not remain trapped in a sub-optimal local maximum or minimum values. Because the optimization information of many different regions are applied, it can move away from a local maximum or minimum value if the population finds better function values in other areas of

the definition domain. The typical procedure of GA includes initial population, evaluation of candidate solutions, reproduction, crossover operation and mutation operation. After mutation is completed, the children population is created and the previous population is replaced by the new generation. Children are evaluated and the fitness function for each individual is calculated. The procedure is repeated until the termination criterion are reached. In this research, the fitness value is the difference between the simulation results and experimental results, which ideally tends to be zero. The optimized objects in this study are the parameters of an induction motor.

#### Appendix A.4 Simulation Results

A 4 KW induction motor, whose parameters are given in Table A.1 [3] , is investigated in this research. The connection type of stator windings is Y-connection. Simulation results are obtained by applying a balanced three phases, 220 V and 50 Hz power source. The GA is applied for searching the optimized parameters. A typical flow chart of GA is provided by Figure A.3. Genetic algorithm generates solutions to optimization problems by selection, crossover and mutation. The GA toolbox of MATLAB is applied for optimisation. The fitness function is given by the following equation, which indicates the difference between the steady-state experimental results and the steady-state simulation results. More specifically, the values of  $f(x)$  are composed of 40% difference value of the current and 60% difference value of the speed.

$$f(x) = \frac{1}{N} \sum_{i=1}^N (0.4 \times (I_{\text{exp}} - I(x))^2 + 0.6 \times (S_{\text{exp}} - S(x))^2) \quad (\text{Appendix A.35})$$

where  $x$  is the vector of optimized parameters,  $N$  is the sample numbers,  $I_{\text{exp}}$  is the steady-state experimental current,  $S_{\text{exp}}$  indicates the steady-state experimental speed [3].  $I(x)$  and  $S(x)$  denote the simulation values of phase A steady-state current and steady-state speed using selected parameters respectively.  $x$  vector includes the stator winding resistance  $R_s$ , stator windings leakage inductance  $L_s$ , rotor bar resistance  $R_b$ , end ring segment resistance  $R_e$ , rotor bar self-inductance

Table A.1: Induction motor parameters [3]

Input supply parameters	
Input supply voltage	220 V
Input supply frequency	50 Hz
Stator parameters	
Effective number of stator turns: $N_s$	156
Stator windings resistance: $R_s$	1.5 $\Omega$
Stator windings leakage inductance: $L_s$	7 mH
Number of pole pairs	1
Rotor parameters	
Number of rotor bars: $n$	28
Rotor bar resistance: $R_b$	96.940036 $\mu\Omega$
End ring segment resistance: $R_e$	5 $\mu\Omega$
Rotor bar self inductance: $L_b$	0.28 $\mu\text{H}$
End ring segment self inductance: $L_e$	0.036 $\mu\text{H}$
Air gap parameters	
Air gap average radius: $r$	70 mm
Air gap length: $g$	0.28 mm
Rotor effective length: $L$	120 mm
Mechanical parameters	
Inertia: $J$	0.002 $\text{N}\cdot\text{sec}^2$
Friction coefficient: $F$	0.001 $\text{N}\cdot\text{sec}^2$

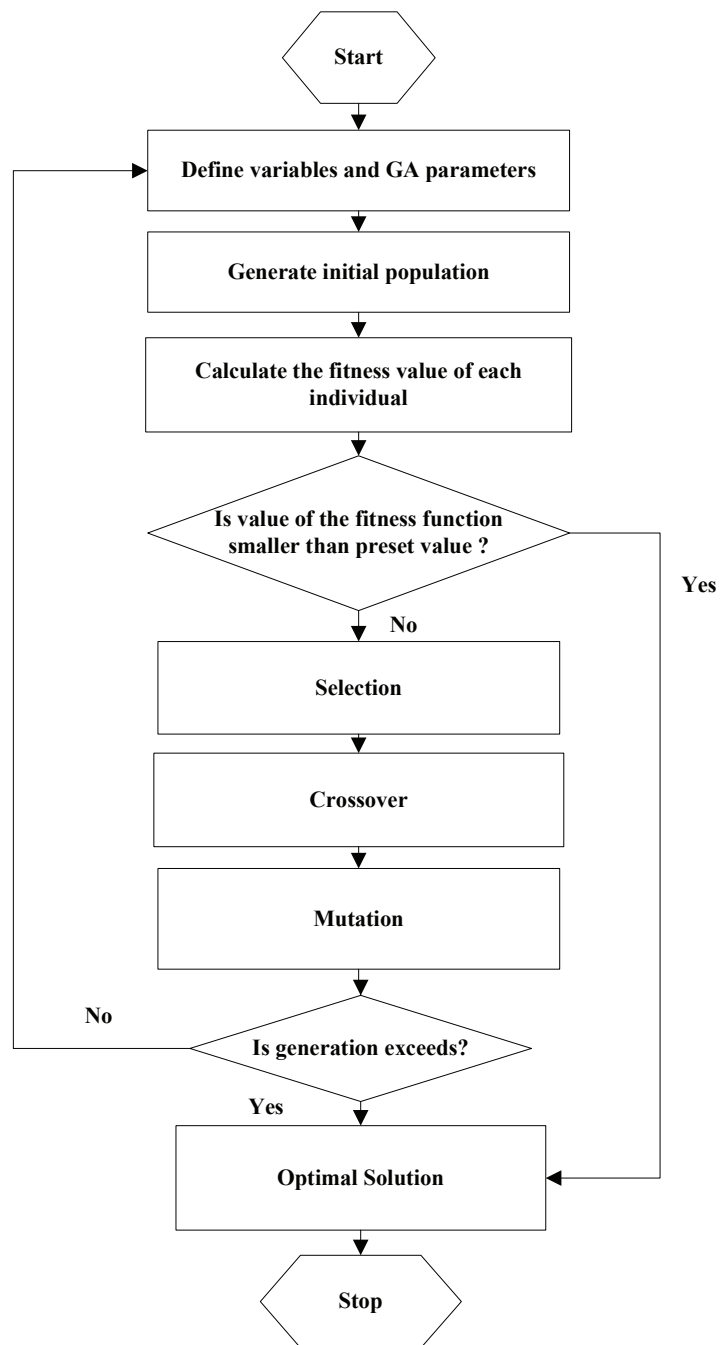


Figure A.3: GA flow chart

$L_b$  and end ring segment self-inductance  $L_e$  respectively. The sample numbers  $N$  is 3000. The searching The low bound of each parameter is set to the fifty percent value of its original value, while the high bound of each parameter is the result of adding the given value to its fifty percent of each value. The optimization stop conditions are either the object function equals to zero or the generation surpasses 50. The population size is 50 for each objective parameter. The selection process is achieved by using Roulette method, the mutation procedure applies Gaussian function and the crossover function is heuristic function with default settings. Table A.4 shows the results of GA and change rate of parameters. The value of objective function decreases from 18.36 to 8.49, which achieves a 53.7% decline. Among the change of all the parameters, the load value increases from 15.00 N·m to 17.33 N·m, which has the highest change rate 14.73%. The stator windings leakage inductance  $L_s$  has the smallest variation rate 2.33%. It decreases to 6.80e-3H. Other parameters are increased by less than 10% from its original value except the stator winding resistance  $R_s$ , which decreases to 1.36  $\Omega$ . Figure. A.4 shows a comparison of phase

Table A.2: Parameter results using GA

	$L_s(\text{H})$	$L_b(\text{H})$	$L_e(\text{H})$	$R_s(\Omega)$	$R_b(\Omega)$	$R_e(\Omega)$	Load	f(x)
Pr <sup>a</sup>	7.00e-3	2.80e-7	3.60e-8	1.50	9.69e-5	5.00e-6	15.00	18.36
Pr <sup>b</sup>	6.80e-3	2.86e-7	3.95e-8	1.36	1.04e-4	5.46e-6	17.33	8.49
Cr <sup>c</sup>	2.33%	2.34%	9.83%	8.81%	8.04%	9.20%	14.73%	53.7%

<sup>a</sup> Original parameters    <sup>b</sup> Parameters obtained by GA

<sup>c</sup> Change rate

A currents using different parameter sets. Compared with the simulation current using the original parameters in Table. A.1, the red dash line, which indicates the simulation current using GA parameters, is closer to the experimental steady-state current between 0.1s and 0.3s. Figure. A.5 illustrates the comparison of speed values. Compared with the black solid line obtained by original parameters, the red dash line, which represents the simulation speed using GA parameters, has a smaller peak value before it reaches steady state. Moreover, the red dash line has a small fluctuation compared with the black solid line in steady-state condition. These results can prove that GA parameters can improve performance of the proposed

model in steady-state condition, whose outcomes are much closer to the measured results. Furthermore, the model based on GA parameters is accurate for further fault diagnosis. In order to implement fault detection of broken bars in induction

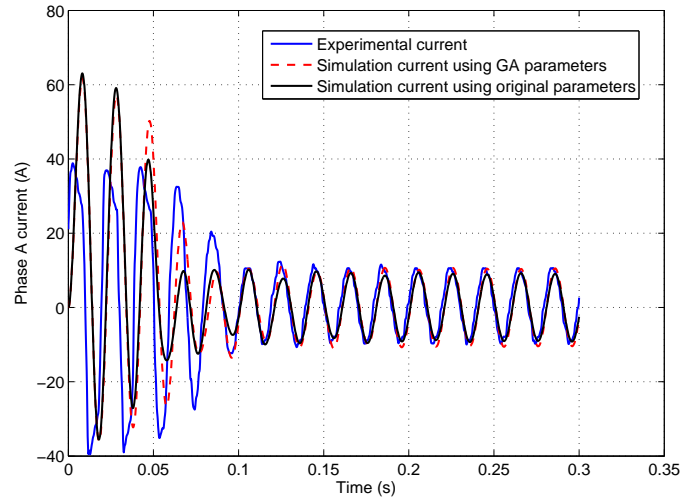


Figure A.4: Comparison of measured current [3], simulation current using original parameters and simulation current using GA parameters

Table A.3: Frequency Points

	One Broken Bar				Two Broken Bars			
Fp <sup>a</sup> (Hz)	42.61	46.19	53.90	57.42	42.19	46.09	53.91	57.81
Fp <sup>b</sup> (Hz)	44.00	47.00	53.00	56.00	41.80	45.90	54.10	58.20

<sup>a</sup> Simulated frequency points <sup>b</sup> Calculated frequency points

motor with a load of 12 N·m, the power spectral density is applied to extract the side frequency components at  $(1 \pm 2ks)f_s$  frequency points. Figure. A.6 shows the stator current power spectral density values of a healthy machine, a machine with one broken bar and a machine with two broken bars. When broken bar faults exist in an induction motor, the harmonic components appear at the right and left sideband of fundamental frequency. The frequency points of all side bands are given in Table A.3. At one broken bar condition, the slip rate is 0.030. It changes to 0.041 when the rotor has two broken bars. The corresponding side frequency points are calculated by  $(1 \pm 2ks)f_s$ , which are also illustrated in Table A.3. There are

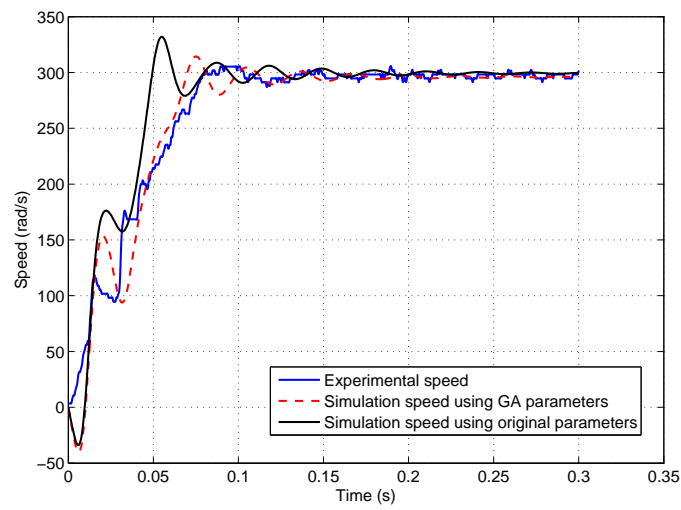


Figure A.5: Comparison of measured speed [3], simulation speed using original parameters and simulation speed using GA parameters

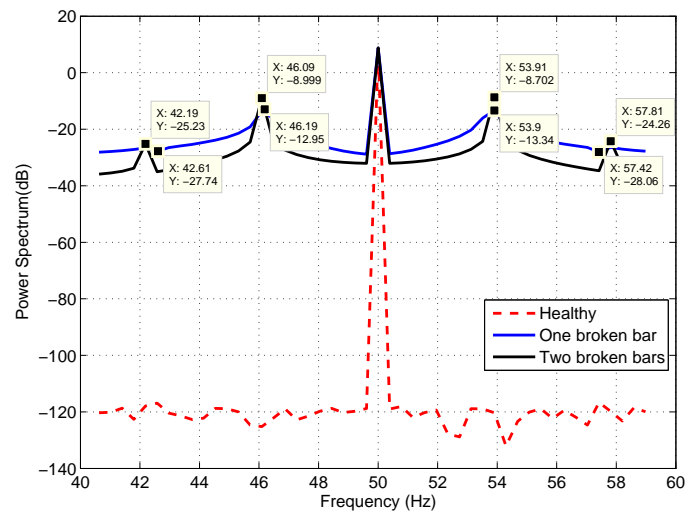


Figure A.6: Comparison of health power spectrum, one broken bar power spectrum and two broken bars power spectrum



Table A.4: Speed and Torque

Fault type	No load		12(N·m)	
	Speed (rad/s)	Torque (N·m)	Speed (rad/s)	Torque (N·m)
Healthy	313.88	0.312	302.56	12.3
One broken bar	313.90±0.01	0.29±0.01	302.53±0.01	12.3±0.1
Two broken bars	313.87±0.01	0.30±0.01	302.23±0.01	12.3±0.1

small difference between simulation values and calculation values in one broken bar condition. However, the gap between these two values in two broken bars condition is smaller. Meanwhile, the fault-related spectral components grow with the extent of the numbers of adjacent broken bars in Figure. A.6. The second order frequency component can be used to recognize the number of broken bars due to clear difference between their amplitudes. As shown in Table A.4, both the speed and the torque are not greatly affected by broken bar faults at no load condition, because only small amount current exists in stator and the asymmetries can be neglected. When the load increases to 12 N·m, the ripples of speed and load tend to increase as the growth of rotor asymmetry current.

## Appendix A.5 Summary

An induction motor model based on multi-coupled circuits has been developed. The inductances are calculated based on the winding function theory. In addition, the best possible set of parameters is obtained by GA, which can reduce the errors between measured values and simulation values. The comparison result of current and speed illustrates a good agreement between the model using optimised parameters and the actual parameters of a motor. It proves that the model can be used to simulate transient-state and steady-state response of a healthy induction motor. Based on the accurate model optimised by GA, simulations for a machine with one broken bar and a machine with two broken bars are undertaken. The power spectral density has been performed to extract fault features. The amplitudes of fault-related spectral components increase with the growth of the numbers of adjacent broken bars. But, speed and torque ripple levels are not greatly affected by rotor broken bars

faults in the light load condition. Because the first order amplitude of one broken bar and two broken bars are very close to each other, the second order frequency components can be used to recognize the number of broken bars. An advanced signal processing technique is required for the detection of second order frequency components in our future study.

# References

- [1] W. T. Thomosn and M. Fenger, Current signature analysis to detect induction motor faults, *IEEE Transaction on Industry Applications Magazine*, 7(4):26–34, Jul 2001.
- [2] G. B. Kliman, J. Stein, R.D. Endicott, and R.A. Koegl, Noninvasive detection of broken rotor bars in operating induction motor, *IEEE Transaction on Energy Conversion*, 3(4):873–879, Dec 1998.
- [3] S. Hamdani, O. Touhami, and R. Ibtiouen, A generalized two axes model of a squirrel-cage induction motor for rotor fault diagnosis, *Serbian Journal of Electrical Engineering*, 5(1):155–170, May 2008.
- [4] H. Toliyat and T. Lipo, Transient analysis of cage induction machines under stator, rotor bar and end ring faults, *IEEE Transaction on Energy Conversion*, 10(2):241–247, Jun 1995.
- [5] Z. Zhang, G. E. Dawson, and T. Eastham, Evaluation of dynamic parameters and performance of deep-bar induction machines, in *Industry Applications Society Annual Meeting*, pages 62-63, 1994.
- [6] S. I. Moon and A. Keyhani, Estimation of induction machine parameters from standstill time domain data, in *Industry Applications Society Annual Meeting*, pages 336–342, 1993.
- [7] M. Bertoluzzo, G. Buja, and R. Menis, Inverter voltage drop-free recursive least-squares parameter identification of a pwm inverter-fed induction motor

- at standstill, in *Proceedings of the IEEE International Symposium on Industrial Electronics*, pages 649–654, 1997.
- [8] A. Gastli, Identification of induction motor equivalent circuit parameters using the single-phase test, *IEEE Transaction Energy Conversion*, 14(1):51–56, Mar 1999.
- [9] F. Alonge, F. Dippolito, G. Ferrante, and F. M. Raimondi, Parameter identification of induction motor model using genetic algorithms, *IEE Proceedings on Control Theory and Applications*, 145(6):587–593, Nov 1998.
- [10] K. S. Huang and Q. H. Wu, Effective identification of induction motor parameters based on fewer measurements, *IEEE Transaction on Energy Conversion*, 17(1):55–60, Jun 2000.
- [11] X. G. Luo, Y. F. Liao, H. A. Toliyat, A. Elantably, and T. A. Lipo, Multiple coupled-circuit modeling of induction machines, *IEEE Transaction Industry Application*, 31(2):311–318, Mar 1995.
- [12] G. M. Joksimovic, M. D. Durovic, J. Penman, and N. Arthur, Dynamic simulation of dynamic eccentricity in induction machines - winding function approach, *IEEE Transaction on Energy Conversion*, 15(2):143–148, Jun 2000.
- [13] G. Stefopoulos, P. Georgilakis, N. Hatziargyriou, and A. Meliopoulos, A genetic algorithm solution to the governor-turbine dynamic model identification in multi-machine power systems, in *Proc. 44th IEEE Conf. Decision and Control*, Page. 1288-1294, 2005.